INVESTIGATING THE MULTI-FREQUENCY PERFORMANCE OF ELECTRO – THERMAL IMAGING: AN EXPERIMENTAL STUDY

A THESIS SUBMITTED TO
THE GRADUATE SCHOOL OF NATURAL AND APPLIED SCIENCES
OF
MIDDLE EAST TECHNICAL UNIVERSITY

BY

GALİP ÖZDEMİR

IN PARTIAL FULFILLMENT OF THE REQUIREMENTS
FOR
THE DEGREE OF MASTER OF SCIENCE
IN
BIOMEDICAL ENGINEERING

SEPTEMBER 2013

Approval of the Thesis:

INVESTIGATING THE MULTI-FREQUENCY PERFORMANCE OF ELECTRO – THERMAL IMAGING: AN EXPERIMENTAL STUDY

submitted by **GALİP ÖZDEMİR** in partial fulfillment of the requirements for the degree of **Master of Science in Biomedical Engineering, Middle East Technical University** by,

Prof. Dr. Canan Özgen
Dean, Graduate School of **Natural and Applied Sciences** _____

Prof. Dr. Vasıf Hasırcı
Head of Department, **Biomedical Engineering** _____

Prof. Dr. Nevzat G. Gençer
Supervisor,**Electrical&Electronics Engineering Dept,METU** _____

Assoc. Prof. Dr. Süha Yağcıoğlu
Co-Advisor, **Biophysics Department, Hacettepe University** _____

Examining Committee Members:

Prof. Dr. Tayfun Akın
Electrical and Electronics Engineering Department, METU _____

Prof. Dr. Nevzat Güneri Gençer
Electrical and Electronics Engineering Department, METU _____

Prof. Dr. Cengiz Beşikçi
Electrical and Electronics Engineering Department, METU _____

Assoc. Prof. Dr. Haluk Külah
Electrical and Electronics Engineering Department, METU _____

Assoc. Prof. Dr. Süha Yağcıoğlu
Biophysics Department, Hacettepe University _____

Date: _____

I hereby declare that all information in this document has been obtained and presented in accordance with academic rules and ethical conduct. I also declare that, as required by these rules and conduct, I have fully cited and referenced all material and results that are not original to this work.

Name, Last name:

Signature :

ABSTRACT

INVESTIGATING THE MULTI-FREQUENCY PERFORMANCE OF ELECTRO – THERMAL IMAGING: AN EXPERIMENTAL STUDY

Özdemir, Galip
M.Sc., Department of Biomedical Engineering
Supervisor: Prof. Dr. Nevzat G. Gençer
Co-Advisor: Assoc. Prof. Dr. Süha Yağcıoğlu

September 2013, 114 pages

Biological tissues have different thermal properties. Medical thermal imaging (thermography) is used to determine local abnormalities in the thermal properties of the body tissues. It is a pain-free examination but it fails determining abnormal tissues in deeper regions. At this point, external sources play a vital role by increasing the image contrast. Due to varying electrical properties of tissues, it is possible to obtain different thermal images by applying electrical currents from the body surface. The contrast in the thermal images can be changed by adjusting the strength and frequency of the current source. In this thesis study, experimental aspects of this hybrid imaging modality is investigated. For that purpose, a current source is designed and realized to apply sinusoidal currents (within the safety limits, maximum 10 mA_{p-p}) in the 10 kHz-1 MHz frequency range for loads up to 2 kΩ. In that frequency range, the current source operates with an error of 2.6% (due to a decreased output impedance of 190 kΩ). To explore the performance of this imaging modality, experiments are conducted using body phantoms and a sensitive thermal camera (320x240 resolution, 50 mK of noise equivalent temperature difference). In

these experiments, none of the biological tissue models (banana, carrot, potato) can be distinguished for a current injection at 10 kHz. On the other hand, at an operation frequency of 500 kHz all of these regions are distinguished. When the current injection frequency is increased to 1 MHz the image contrast is improved by 80 %.

Keywords: *active thermography, electro-thermal imaging, current source, breast cancer*

ÖZ

ELEKTRO - TERMAL GÖRÜNTÜLEMENİN ÇOKLU FREKANS PERFORMANSININ İNCELENMESİ: DENEYSEL ÇALIŞMALAR

Özdemir, Galip
Yüksek Lisans, Biyomedikal Mühendisliği Bölümü
Tez Yöneticisi: Prof. Dr. Nevzat G. Gençer
Ortak Tez Yöneticisi: Doç. Dr. Süha Yağcıoğlu

Eylül 2013, 114 sayfa

Biyolojik dokular farklı termal özelliklere sahiptir. Medikal termal görüntüleme yöntemi, göğüs dokusundaki termal özellikler yardımıyla, anormallikleri tespit etmede kullanılır. Hastaya acı vermeyen bu yöntem, derin kısımlardaki anormal dokuları tespit etmekte başarısız olmaktadır. Bu noktada dış kaynaklar doku kontrastını artırmakta önemli bir rol oynar. Dokuların değişik elektriksel özellikleri, vücut yüzeyine elektrik akımı uygulayarak farklı termal görüntüler elde etmeyi mümkün kılmaktadır. Bu termal görüntülerin kontrastı da akımın büyüklüğü ve frekansı ayarlanarak değiştirilebilmektedir. Bu tez çalışmasında, bu hibrit görüntüleme yönteminin deneysel özellikleri incelenmiştir. Bu amaçla, sinuzoidal akımlar (tıbbi güvenlik sınırları içerisinde, en fazla 10 mA_{p-p}) uygulayabilmek amacıyla 10 kHz – 1 MHz frekans aralığında 2kΩ'a kadar olan yükleri sürebilen bir akım kaynağı tasarlanıp, üretildi. Akım kaynağı, bu frekans aralığında %2.6'lık bir hata payına sahiptir (çıkış empedansının 190kΩ'a düşmesi nedeniyle). Bu görüntüleme yönteminin performansını incelemek amacıyla, doku modelleri ve

duyarlı bir termal kamera (320x240 çözünürlük, gürültüye eşdeğer sıcaklık farkı 50 mK) ile deneyler yapılmıştır. Bu deneylerde kullanılan biyolojik doku modelleri (muz, patates, havuç) 10 kHz frekansında akım uygulandığında fark edilemezken, frekans 500 kHz'e çıkartıldığında ayırt edilebilmiştir. Akım uygulama frekansı 1 MHz'e yükseltildiğinde ise görüntü kontrastında % 80'lik bir iyileşme sağlanmıştır.

Anahtar kelimeler: *aktif termografi, elektro-termal görüntüleme, akım kaynağı, göğüs kanseri*

To my family

ACKNOWLEDGMENTS

Not overestimating their influence, I owe my deepest gratitude to my supervisor Prof. Dr. Nevzat G. Gençer and co-advisor Assoc. Prof. Dr. Süha Yağcıoğlu for their invaluable guidance and support in this study. It was great honor and privilege for me working with Prof. Gençer and Prof. Yağcıoğlu.

Exclusively, I really appreciate the opportunities provided by Assoc. Prof. Dr. Teyfik Demir (TOBB University of Economy and Technology) in the experimental procedure of this thesis study. Prof. Demir has always a positive approach and a great contribution by providing me devices to construct the experimental setup.

Here, I also would like to express my appreciation to my friends, both in Middle East Technical University and TOBB University of Economics and Technology, Balkar Erdoğan, Cihan Göksu, İlkay Günel, Nazım Babacan, Semih Çetindağ, Umut Aradağ, Burak Mert, Güneş Otlu and especially Hamza Feza Carlak, İsmail Ozan Sert and Gökhan Yıldırım for their assistance and invaluable contributions.

I would like to thank my family for their support throughout this thesis. They encouraged me to apply a Master of Science degree and gave the best effort a parent can do. I always felt their love and support in my heart, no matter what happens.

Recording my sincere to thank Nehir Güneş, not only for the help of drawings in this thesis but also her endless support during the writing and organizing my thesis, she was completely supportive and motivating through all the time. I am not sure if I could complete study if it was not for her.

TABLE OF CONTENTS

LIST OF TABLES

TABLES

LIST OF FIGURES

FIGURES

CHAPTER 1

INTRODUCTION

Researchers investigate new imaging modalities to examine human body for diagnostic purposes. Medical imaging is a widespread research area, but mostly focused on cancer research. Due to the high mortality rate [1], many imaging modalities are developed for breast cancer. Mammography is the preferred imaging technique for breast cancer detection, however, medical thermal imaging is also used to detect breast abnormalities after recent developments in thermal detector technology. Lawson was the first investigator who proposed to use thermography in medical area [2]. Following Lawson's study, many researchers detected breast abnormalities using thermography, however results were not satisfactory compared to mammography [3]. These studies have inspired researchers in this area concluding that thermography can be used as cancer risk indicator. In recent years, the sensitivity of thermography has been increased by the use of external sources, leading to a new title for the imaging modality, namely, ¨active thermography¨. Many heat sources are used to manipulate the body temperature distribution: cold air stress, light, electromagnetic waves, etc. [4,5]

An alternative active thermography technique, namely Electro-thermal imaging, was recently proposed by the researchers in the Middle East Technical University (METU)[6]. In this technique, electrical currents are applied using electrodes attached on the body surface. Consequently, apart from metabolic heat sources and tissue thermal properties, the electrical conductivity distribution becomes a parameter in the determination of temperature distribution. Two-dimensional (2D) simulation and experimental studies of Carlak *et al*. suggest that this pain-free exam can improve the conventional thermography image quality. This technique

differentiates from others by the possibility of obtaining multiple images by altering the frequency of the stimulation. These multiple images are beneficial for detecting the abnormality in the healthy breast tissue.

In 2D simulations, current sources created additional temperature difference between cancerous and healthy tissue. It was concluded that the proposed method results in 70% increase in breast cancer detection performance [7]. Carlak and colleagues have also tested the performance of electro-thermal imaging using three-dimensional (3D) simulations [8]. Results show that a 40 mm^3 tumor located at 1.5 cm depth can be detected by applying currents lower than the safety limits.

In this chapter motivation, scope and a short outline of the thesis study will be presented. Following sections will cover the studies of various methodologies used in breast imaging. Also, a brief history of thermal imaging and electrical impedance tomography will be discussed.

1.1 Motivation of the Thesis

There is 12.15% probability (1 of every 8) among women to have breast cancer throughout their lives. Detecting breast cancer has a significant importance since the chance of full recovery gradually decreases when the cancer diagnosed at later stages [1]. Figure 1.1 shows the clinical and preclinical phase of tumor [9]. Note that tumors become detectable in 8-10 years, and the treatment becomes more difficult for tumors of larger size. Mammography seems to be the best imaging modality for detection, however, it does not have sufficient performance for dense breast tissues [10] and it cannot distinguish tumors smaller than 1.66 cm in diameter [10].

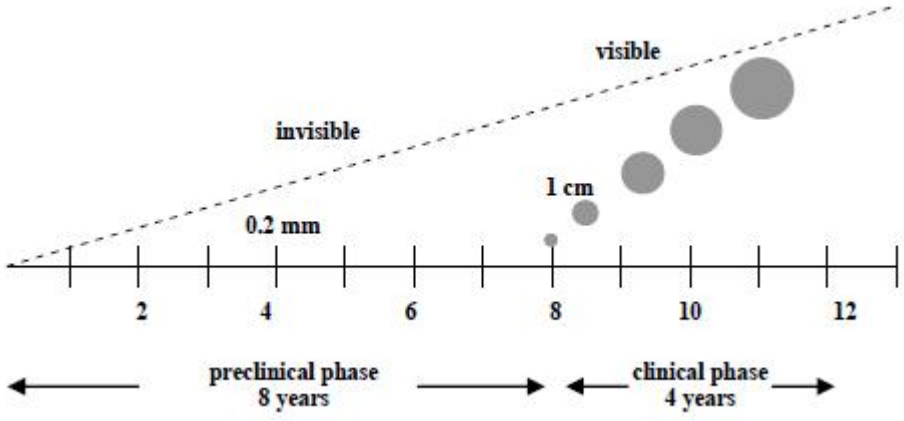

Figure 1.1 Clinical and preclinical phase of tumor [9]

Infrared imaging and electrical conductivity (impedance) imaging are two alternative imaging modalities that can also be used to detect breast cancer. Both modalities are non-invasive and radiation free with a short application time.

Breast thermography can be used as a risk indicator for cancer (with a high sensitivity and specificity rate). A consistent abnormal thermogram may eventually yields cancer in forthcoming years. But thermography alone does not have satisfactory results for the tumors located in deeper regions of the biological tissue. Temperature distributions on the skin surface are mainly caused by blood perfusion and metabolic heat generation. If the tumor is small, even modern state-of-the-art infrared cameras, having a noise equivalent temperature difference (NETD) of 20 – 30^{o}mK, may fail and cannot detect the abnormality.

Electrical impedance tomography (EIT) studies indicate that electrical properties of the biological tissues can be used for medical purposes. Organs and tissues can be differentiated according to their electrical properties. Tumor tissues with a high metabolic rate and in need of angiogenesis (formation of new blood vessels), show greater conductivity values compared to the surrounding tissues. Thus, EIT has the potential to distinguish malignant and health tissues. Additionally, these electrical parameters also vary with frequency. By adjusting the frequency of current drive, it

is possible find an optimum frequency range where the bio-impedance values of the tumor and surrounding tissues provide a maximum contrast on the image. Note that, tumor tissue has 3 to 5 times higher conductivity than normal breast tissues [11].

Electro-thermal imaging is a combined modality of infrared and electrical impedance tomography. Studies prove that additional heat sources improve the image contrast in thermography. This heat source may be in different forms of energy. Applying a time varying electrical current is a commonly used method in electrical conductivity imaging. Injecting current creates voltage distributions in biological tissue, condensing in highly conducting tumor tissues. Thus, tumor heats up more than its surrounding tissue. Electr0-thermal imaging takes advantage of medical infrared imaging and electrical impedance tomography, yielding higher contrast in thermal images [6].

As an additional advantage, if the frequency of applied current changes, the image contrast may be affected. With the additional knowledge obtained by a multi-frequency study, an optimal frequency band can be detected for this modality to detect tumor tissues.

1.2 Scope of the Thesis

There are two major objectives of this study:

- To design and build a voltage controlled current source (VCCS) to be used as an external source for electro-thermal imaging

- To develop body phantoms and conduct 2D experiments at varying frequencies using an infrared camera.

1.3 Outline of the Thesis

In this chapter, first information about breast cancer will be presented. The status of breast cancer points out that it is a highly probable and fatal cancer type. Next sections will discuss imaging modalities used to detect breast cancer. Since electro–thermal imaging is a combination of electrical conductivity and thermal infrared imaging, studies about these techniques will be explained in detail.

In the following chapters:

- Chapter 2 explains the theory of Electro-Thermal Imaging. In the first sub-section, a review on active thermography studies is available. Starting with the Pennes' Bio-Heat equation, a detailed explanation and derivations of the modality is discussed. The thermal equilibrium equations corresponding to ¨passive¨ and ¨active¨ modes will be obtained.

- Chapter 3 discusses the design procedure of the voltage controlled current source. First, a short review of current sources is presented, followed by the design aspects of the source. Thereafter, simulation and implementation (hardware) performances (output impedance characteristics) are introduced

- Chapter 4 contains information about experimental studies. Explanation of the experimental setup, phantom preparation and properties are given in detail. In the following sections, experimental results and analysis of these results are discussed.

1.4 Introduction

Human body is made up of millions of cells. The normal life cycle of a cell consists of growing, dividing to form new cells and dying. At the early ages of a person's life, normal and healthy cells divide faster to make that person's growth possible. When

the person reaches to the adult stage of his/her life, most of the cells divide only to replace the dying cells or to repair present injuries.

Cancer is the definition of the cells that start to grow out of control. There are many kinds of cancer that are similar of having abnormal cells with out-of-control growth. Cancer cells have different cell cycle than the healthy ones. While a normal cell completes its life with dying, cancer cells continue to grow forming abnormal cells that sometimes may invade other tissues. This is caused by damage to the cell DNA. A healthy cell with a damaged DNA, tries to repair the damage and if not, the cell dies (necrosis). However, cancer cells continue to divide and form new cells despite the DNA damage. Most types of cancer cells form a mass called ¨tumor¨, and are named after where the tumor is located in the body.

In breast cancer, cancer arises in the breast tissue, either in glands responsible for milk production (lobules), or in ducts that connect these lobules to the nipples. Majority of breast cancers are invasive. These invasive cancers arise in the lobules or in the ducts of the breast, break the duct or glandular walls and spreads to surrounding tissues.

1.4.1 Types of Breast Cancer

Breast cancer is commonly divided into 4 types as follows:

- Ductal carcinoma in situ,
- Lobular carcinoma in situ,
- Invasive (infiltrating) ductal carcinoma,
- Invasive (infiltrating) lobular carcinoma.

Ductal carcinoma in situ (DCIS) is the most common non-invasive breast cancer. Lobular carcinoma in situ (LCIS) is considered as pre-cancer. These non-invasive cancer cells have not spread into the surrounding tissues. Invasive ductal carcinoma (IDC) origins in milk duct of breast, but spreads and grows into the fatty tissue of

breast. 80% of invasive breast cancers are these types with the possibility to metastasize to other parts of the body through lymphatic system and bloodstream. Invasive lobular carcinoma (ILC), origins in lobules and similar to IDC, can also metastasize. ILC is more difficult to detect by mammography compared to invasive ductal carcinoma.

1.4.2 Breast Cancer Statistics

Breast cancer is the second leading cancer cause following lung cancer [1]. According to the most recent and updated estimates of American Cancer Society, in United States, there are;

- ~63300 new diagnosis of non-invasive carcinoma
- ~226000 new diagnosis of invasive carcinoma
- ~39500 deaths from breast cancer

in 2012[1].

Another surveillance analyzes the incidence rates of breast cancer among females in United States, by race and tumor size [1] between 1988 and 2008. Results indicate that the tumors smaller than 2.0 cm are significantly more frequently diagnosed than mid-sized tumors (>5.0 cm). Although the incidence rate varies by race, the study suggests that almost 65% of the detected tumors are smaller than 2.0 cm.

Another research investigates the relation of tumor size and survival rate. Females, each are diagnosed with breast cancer, are surveyed for 5-year period. The results show:

- 95% survival rate for tumors < 2.0 cm
- 82% survival rate for tumors between 2.1 & 5.0 cm
- 63% survival rate for tumors > 5.0 cm

Considering this knowledge, detection of small tumors (sensitivity of the imagers, discussed in further sections) becomes more important.

In addition to the survival rates, depending on tumor size, early diagnosis (stage of the cancer) is also crucial. Table 1.1 shows the probability of a woman developing invasive breast cancer with her age.

Table 1.1

The probability of developing breast cancer against age [1]

If current age is..	The probability of developing breast cancer in the next 10 years	or 1 in
20	0.06%	1681
30	0.43%	232
40	1.45%	69
50	2.38%	42
60	3.45%	29
70	3.74%	27
Lifetime Risk	12.15%	8

It can be seen that 1 out of every 8 women, either has or will develop invasive breast cancer in her life. Given the fact that early diagnosis increases the possibility of full recovery, regular examinations and developing more sensitive imaging modalities are lifesavers.

1.5 Imaging Modalities Used for Breast Cancer

Mammography is the most effective and widely accepted imaging technique for breast cancer detection. Despite being commonly used, current performance of mammography is still questionable. For this purpose, additional imaging modalities are used other than x-ray mammography: positron emission tomography (PET), magnetic resonance imaging (MRI), breast thermography, including breast ultrasound (sonography), ductogram, etc.

Early diagnosis is important for the breast cancer treatment. Since a single imaging modality is not sufficient in diagnosis, different imaging modalities are developed to improve diagnosis accuracy. Table 1.2 shows the results of a study that compares the performance of mammography, ultrasound, MRI, clinical examination and their combined systems.

Table 1.2 Comparison of different modalities [12]

Modality	Sensitivity	Specificity	Positive Predictive Value	Accuracy
Mammography	67.8%	75%	85.7%	70.2%
Mammography and clinical examination	77.4%	72%	58.6%	75.6%
Clinical examination	50.3%	92%	94%	63.6%
Ultrasound	83%	34%	73.5%	67.8%
Mammography and ultrasound	91.5%	23%	72.3%	70.2%
Mammography, clinical examination and ultrasound	93.2%	22%	72.4%	70.9%
MRI	94.4%	26%	73.6%	72.9%
Mammography, clinical examination and MRI	99.4%	7%	70.1%	70.5%

1.5.1 Mammography

Mammography has been used in the past decades and it still is the best imaging technique for breast cancer diagnosis. Food and Drug Administration (FDA)

strongly suggests annual mammography screening for woman over 40 years old. Features are:

- low cost compared to other modalities
- sufficient sensitivity and specificity [13]
- low interpretation time for examination

Despite being the best screening tool, mammography has many drawbacks and limitations:

- Mammography is unsuccessful in younger women, because their breasts are dense (more glandular, less fatty tissue), so can hide the tumor.
- Mammography is likely to miss tumors smaller than 1.66 cm [10].
- High false-positive rate causes unnecessary biopsies.
- Screening is uncomfortable for patients because of squeezing the breast to obtain high-resolution images.
- Patients are exposed to radiation. Because of this reason, pregnant women cannot be screened by mammography. There are studies indicating that even regular mammography check itself can cause cancer.

1.5.2 Ultrasound

Breast ultrasound (sonography) is a non-invasive method that uses sound waves and their echoes bouncing off of the internal organ boundaries, fluids and tissues. Ultrasound is less expensive compared to the other imaging modalities, provides sufficient images for women under 30 years, however, cannot show micro-calcifications which may be precursors for early cancer. Ultrasound has high sensitivity for small invasive tumors [14].

1.5.3 Positron Emission Tomography

Positron emission tomography (PET) scan is useful to identify metastatic lesions but overall sensitivity and spatial resolution cannot compete with mammography. For small breast tumors less than 1 cm, PET can only identify 25% of the breast cancer [15].

1.5.4 Magnetic Resonance Imaging

For women at high risk for breast cancer, magnetic resonance imaging (MRI) screening is advised additionally to mammography. MRI, which is free off radiation, is more sensitive than mammography. Even though MRI has super spatial resolution [16] (even in dense tissue), it may still miss some cancers and may likely to find something that is not cancer (high false-positive rate). MRI is also more expensive than any other imaging techniques. Because of having long and uncomfortable (lying in a tight area) data acquisition process, MRI examination is not the first choice of many patients. MRI also is not as widely available as mammography.

1.5.5 Thermography

It has been known that using temperature in the detection of a disease or illness relies on very past. The ancient Egyptians used their hands across the body surface to observe the changes in the temperature. In 400 B.C. the Greek Physician Hippocrates wrote, ¨In whatever part of the body excess of heat or cold is felt; the disease is there to be discovered.¨ As the old people knew heat is a property of the human body, they did not have enough information to create a certain standard reference.

Galileo was the first to design a temperature sensing device, still without a scale. Fahrenheit fixed the freezing point of water at 0 and boiling temperature at 212 degrees. In 1742, Celsius modified Fahrenheit's scale using 0 as boiling and 100 as

the freezing temperature. Swedish botanist Linnaeus reversed Celsius' work resulting today's commonly used temperature scale (100 degrees for boiling temperature).

In 1800 an astronomer, Sir William Herschel discovered infrared radiation while trying to measure the heat of the colors on the rainbow spectrum. He observed that highest temperature to fall beyond the red color end, however; it was his son Sir John Herschel managed to record heat rays on the far red color end (infra-red), by creating an image, using carbon suspension in alcohol, he called ¨thermogram¨. With additional studies after that time, the complete electromagnetic spectrum appears as follows:

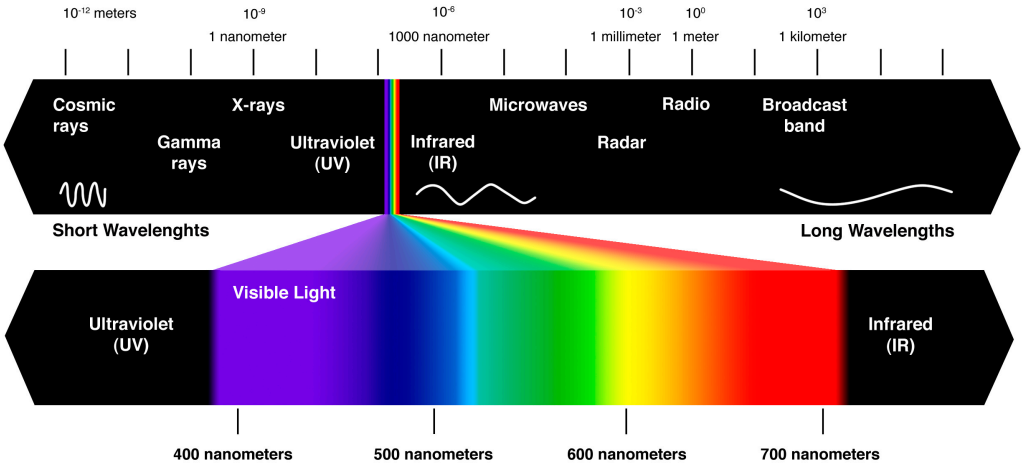

Figure 1.2 Electromagnetic Spectrum [17]

It can be seen in figure 1.2, visible light covers a very narrow band in the whole spectrum that Herschel tried to investigate. The band contains radiations that have slightly longer wavelengths than the visible spectrum is called infrared region. It is divided into 5 bands (fig 1.3):

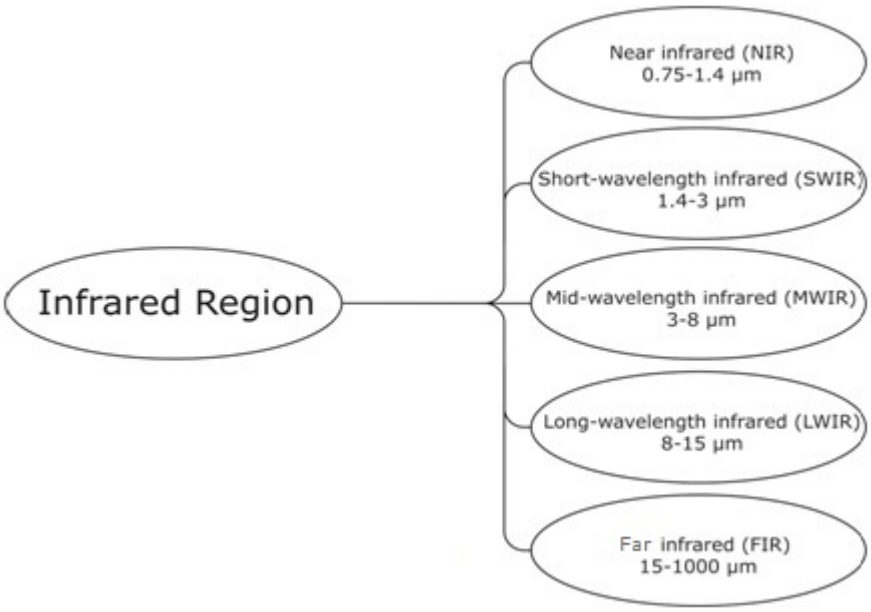

Figure 1.3 Sub – regions of infrared spectrum

1.5.5.1 History of Infrared Theory

Gustav Kirchoff was the first one, to come up with the blackbody concept. He claimed that, the energy absorbed should be equal to the energy emitted at each wavelength (λ), when an opaque material is at thermal equilibrium:

$$\alpha(\lambda) = \varepsilon(\lambda) \tag{1.1}$$

where α is the reflection coefficient and ε is the emittance. Emittance is almost unity at all wavelengths for a blackbody. Consequently, good absorbers are poor reflectors. Therefore, good blackbody sources appear black.

All objects with temperature above absolute zero (-273^{o}C) emit radiation from their surfaces. The Stefan-Boltzmann Law (in 1879) defines the relation between this emitted energy and absolute temperature. The total emitted radiation power is

proportional with the area, emissivity and the fourth power of the temperature of the object.

$$P = A\varepsilon\sigma T^4 \tag{1.2}$$

where, P is the total emitted radiation power (watt), A is the object surface area (m^2), ε is the emissivity, σ is the Stefan-Boltzmann constant (J/sm^2K^4) and T is the absolute temperature (K). Resulting that, the emitted radiation per unit area only depends on the emissivity and absolute temperature.

$$W \sim \varepsilon T^4 \tag{1.3}$$

where, W is the total emitted radiation per unit area ($watt/m^2$), ε is the emissivity and T is the absolute temperature (K).

In 1880s and 1890s, Wilhelm Wien continued Kirchoff's study about radiation. His blackbody radiation law, which was corrected by Planck later, was valid at high frequencies. However, he also formulated the peak value of the wavelength emitted by an object in relation with its temperature.

$$\lambda_{\max} * T = 2.8977 \ nm \cdot K \tag{1.4}$$

He concludes that if the absolute temperature of the object elevates to higher values, the body can emit shorter wavelengths.

Shortly after Wien's study, Max Planck proposed the function of spectral radiance of the surface of a blackbody for a specific wavelength. Planck's Law (1901), written as:

$$B_\lambda(T) = \frac{2hc^2}{\lambda^5} \frac{1}{e^{\frac{hc}{\lambda k_B T}} - 1} \tag{1.5}$$

where, B_λ is the spectral radiance ($W \cdot sr^{-1}m^{-3}$), h is the Planck constant ($J \cdot s$), c is the speed of light(m/s), λ is the corresponding wavelength (m), k_B is the Boltzmann constant ($J \cdot K^{-1}$) and T is the absolute temperature (K). The Boltzmann constant should not be confused with the Stefan-Boltzmann constant described previously, which has a formula of:

$$\sigma = \frac{2\pi^5 k_B^4}{15h^3c^2} = 5.6703 \cdot 10^{-8} Jm^{-2}s^{-1}K^{-4} \tag{1.6}$$

where k_B is the Boltzmann constant ($J \cdot K^{-1}$), h is the Planck constant ($J \cdot s$) and c is the speed of light in vacuum (m/s).

1.5.5.2 Development of Thermal Detectors

Detectors use specific wavelength bands to obtain higher transmittance (almost unity) and minimize losses.

Richard D. Hudson created a list of applications for thermal imaging systems in 1969, into four major categories: military, industrial, medical and scientific. Detectors are designed and developed corresponding to the need and application area. Today, thermal imagers are widely used for military purposes.

Lead sulfide (PbS), invented in 1930s, is sensitive to radiation for wavelengths 1 – 2.5 μm. When cooled (i.e. using liquid nitrogen), the sensitivity range of PbS changes to 2 – 4 μm. Thus, detectors that operate in the near infrared band can be developed with PbS. In 1952, Heinrich Walker discovers indium antimonite (InSb) that later makes thermal imaging possible in the mid band infrared region. Lawson's discovery of infrared detection properties of mercury cadmium tellurium (HgTeCd) had opened a wide window, that still today majority of the infrared systems use HgTeCd detectors to image in the far region (8-14 μm).

Thermal systems applications are conducted first, for military purposes and then for clinical purposes in 1970s. There were two basic technologies: liquid crystal contact thermography and noncontact blackbody infrared imaging. Performance of the cameras on those days, was limited due to the used material properties. Liquid crystal contact thermography has low thermal resolution (± 0.5^{o}C), low spatial resolution (± 5mm), long response time (>60 sec). Significant thermometric information can be obtained in the far infrared region (8 – 12 μm). Even though skin has >0.98 emissivity value in that region with a blackbody radiation reached its peak value between 30 and 34^{o}C, state of the art infrared thermal imagers in 1970s, were not better than liquid-crystal thermography because of the technology limitations:

- Early digital infrared cameras had a 128x128 pixel resolution. With a field of view of 32x32 cm, yields to 2.5x2.5 mm pixel size.
- Thermal resolution was also law (almost ± 0.1^{o}C)
- Single detector cameras needed 4 seconds to take a single image. During this data acquisition time, blurs caused by involuntary patient movement, skin temperature drifts with ~0.05^{o}C/sec generate a physiological noise in the order of ± 0.2^{o}C.
- Until mid-1980s, clinical infrared cameras did not have blackbodies for calibrating, resulting an error of 1^{o}C for the same patient, imaged on different days [18].

Studies using thermal infrared cameras increased with the development of the 2nd and 3rd generation of detectors. At the beginning of the 1990s, focal plane array (FPA) cameras having 256x256 pixels per frame and >100 frames/sec speed were designed. This high resolution, fast scanning cameras then even were improved to 1024x1024 pixel size, which made sensing 0.02-0.03^{o}C temperature difference possible.

There are some thermal detectors that operate at room temperature. Since they do not need any cooling mechanism, they are called ¨uncooled detectors¨. Uncooled

detectors are lightweight, small and easy to use but not sensitive as cooled detectors. Cooled detectors have to be cooled below 77-100^{o}K to get reliable performance. Generally liquid nitrogen is used for the cooling procedure.

Quantum Well Infrared Photodetector (QWIP) is based on gallium arsenide (GaAs) technology. It has high sensitivity for the wavelengths 3 to 19 μm, and high resolution that can detect 0.01 ^{o}C changes in the temperature.

1.5.5.3 Detector Output

As mentioned previously, objects with higher temperature than absolute zero emit radiance. Infrared imaging systems are used to determine the amount of this emitted radiance.

The output of the infrared camera is due to the emittance and reflectance of all the sources in the field of view. That is,

Detected Energy = Emitted Energy + Reflected Energy

Emitted energy = Emitted from object + Emitted from Background

To obtain the emitted energy of the source (object), emitted energy of the background should be subtracted from the total emitted energy detected by the imaging system:

Emitted from object = Emitted energy – Emitted from Background

Output signal (voltage) of the thermal detector is dependent of ε (the emissivity of the object), T (the absolute temperature of the object), internal properties of the imaging system (the transfer function of the system - independent of the object), τ_{ATM} (the transmittance of the atmosphere).

1.5.5.4 Thermography in Medical Area

Breast cancer is the most common cancer in women, and second deadly cancer type after lung cancer. In the previous parts, it was shown that early diagnosis increases the rate of survival. For the purpose of improving the performance of diagnostic tools, designing more sensitive screening systems plays a key role. Thermal imaging may be a helpful methodology to decrease the mortality rates. It can provide complementary information to other imaging techniques, and detect abnormalities that mammography cannot.

Medical thermography is a pictorial recording of the body temperature taken by a heat sensing device due to the natural infrared emission. Thermography cannot be used to decide whether a tissue is cancerous or not, it just discovers a local temperature abnormality.

Lawson was the first to use thermography to diagnose breast cancer [2]. In 1956, he investigated 26 patients who all were diagnosed with breast cancer. He resulted that an average of 2.27^{o}F temperature rise detected around the tumor tissue.
United States was introduced infrared imaging by a radiologist, Gershon - Cohen, in 1965. In his publication in 1968, he reported 94% sensitivity and 6% false positive rate for thermography on 4000 cases [19].

January 29, 1982 was a milestone in medical thermography history. At this date, Food and Drug Administration (FDA) approved thermography and classified it as an adjunctive screening technique for breast cancer detection.

There are very long-term studies in the literature about breast thermography. One of these researches, published in 1980 by Michel Gautherie and Charles M. Gros, exploring whether thermography could be used for cancer risk prediction [20]. They examined approximately 58000 patients in 12 years (between August 1965 and June 1977) and classified patients with stages from 1 to 5. Stage 3 thermograms represent

a suspicious abnormality but not certain diagnosis. These 1527 women are re-screened in 5 years. 44% of the patients develop malignancy during this period, who were diagnosed as normal at the initial physical and x-ray examinations including ultrasonic studies. Study concluded that, an abnormal thermogram was a high risk marker for the development of the breast cancer in future.

Another long-term study was operated by Isard *et al.* (1972). They combined thermography and mammography to detect local abnormalities on 10055 patients in 4 years [21]. Patients are asked to remove all of clothing over their waist in a cool room, 20-21^{o}C. They stated that, in this examination conditions, waiting to obtain a thermal equilibrium is not meaningful, as they had experienced there was no distinguishable difference in the image quality or contrast of breast thermogram for periods 3 – 15 minutes. The patients are divided into two sections titled, symptomatic and asymptomatic. Asymptomatic patients who did not have any complaints or pain claiming, they just screened for routine examination. Thermogram detected abnormalities in 1028 of those 4393 asymptomatic patients. Authors concluded that, thermography not only improves the diagnostic accuracy for the symptomatic patients in collaboration with mammography, but also determines the women in high risk state for breast cancer in the asymptomatic group. Combining two modalities will result a 10% increase in the sensitivity rate of detection.

In 1986, Nyirjesy and his colleagues published their results over 16778 participants, of whom 4716 with confirmed carcinoma, 3305 with histologically diagnosed benign breast disease [22]. This paper compared clinical examination, mammography and thermography. While clinical examination has 75% sensitivity in detecting all tumors and 50% in small tumors (<2 cm size), mammography showed 80% sensitivity with 73% specificity. On the other hand, results demonstrated 88% general, 85% for tumors smaller than 1 cm sensitivity, and also a specificity rate of 85%.

Spitalier and his associates screened 61000 women with thermography. At the end of the 10-years-long study, they came up with 89% sensitivity and specificity (11% false-negative and false-positive rate) and also 91% rate of non-palpable cancer detection [3]. Results also indicated that screening patients with thermography could provide additional cancer development risk information. In 60% of the cancer patients, thermography pointed out first alarm. Thus, even if patients did not have clinical malignancy suspicion, abnormal thermogram represents highest risk factor for breast cancer development.

In the 1980s, there were many studies on patients to determine the effect of the thermography on breast cancer detection. In one of these studies, 39802 patients screened in 3 years, resulting 85% sensitivity and 70% specificity [23]. 30% of the cancers, could not be detected with classical imaging modalities, emphasizing the value of thermography. However, Haberman noted that more than 10 years observation time needed to obtain more reliable false positive rates.

Another study showing high sensitivity rate for thermography was done in 2003. By examining 875 biopsies from 769 women (some of the patients had more than once), Parisky and associates reached 187 malignant and 688 benign tumors. Index of suspicion respresented 97% sensitivity in breast cancer detection [24].

In the year 1984, Thomassin *et al.* observed 4000 confirmed breast cancers [25]. 130 of 4000 cancers, were subclinical carcinoma with a tumor size of 3 to 5 mm. Both mammography and thermography are used in this study. Each technique screened patients one by one prior to their combined model imaging. 10% of the 130 carcinomas were detected only by mammography whereas thermography alone detected 50% of the tumors. Remaining 40% of the patients required application of combination of thermography and mammography. Thus, authors resulted while thermography detecting half of the carcinomas, it also gave thermal alarm to the 90% of the patients who were examined.

Former studies investigated the performance of breast thermography without knowing the effect of the tumor size, depth, stage etc. Therefore, it was not possible to improve the performance of the thermography. For this purpose, mathematical models of the breast tissue are developed to figure out the anatomical and physiological aspects. These models have been used for simulation studies to analyze the limitations of thermal imaging. For the comparison of different applications of thermography (in combination with other imaging techniques), *in vivo* and *in vitro* experiments were done in addition to simulation studies. Some researchers, who did not have opportunity to examine human patients, used phantom models or animals either.

Gonzalez published a simulation study in 2007. He solved the bio-heat equation for a simplified female breast model, which was approximated to match the average patient in Gautherie's study [26]. Finite element method simulations resulted that a 3 cm-sized tumor could be detected up to 7 cm depth, and if located close to the surface of the skin, small tumors (~0.5 cm), could be captured using state-of-the-art infrared imagers (having a 20mK sensitivity) [27].

There are studies exploring new algorithms or creating multi-modal techniques to improve the image quality. However, the development of the performance of the breast thermography basically depends on the design of higher resolution, more sensitive infrared cameras. With the 3rd generation detectors, thermography has begun to provide more accurate results in recent studies. For this purpose, Joro and Laaperi compared the performance of the infrared cameras using in the procedure of breast cancer diagnosis. A long-wave quantum well infrared photovoltaic (QWIP), and two mid-wave detectors were used on 10 cases with a breast cancer size of 6 – 45 mm [28]. The results indicated that InSb mid-wave detector showed the best performance, and microbolometer technology was not sufficient to detect the tumors. GaAs QWIP detector had adequate results in between the other cameras.

1.5.6 Electrical Conductivity Imaging

The tissues and organs of the human body have different anatomical and physiological characteristics. Additionally, the tissues also show different electrical properties. Thus, it is possible to identify each one of these tissues and organs by measuring the electrical conductivity distribution.

Electrical conductivity imaging (ECI) or electrical impedance tomography (EIT) has been used for many years. Different methodologies are being used and many new modalities are still being proposed. Introducing power to the body is necessary as for all other imaging modalities. Either voltage is introduced to the body and current patterns are measured from the body surface or, more commonly, current is introduced and voltage measurements are recorded.

A similar technique, electrical resistivity imaging (ERI), is used to image the structures of the earth. It differs from EIT, in the sense of current application. Since large areas need to be examined, very low frequency current is used. This is called ¨Telluric current¨, which travels underground or through the sea. The beginning of the utilization of this method withstands to 19^{th} century.

Electrical properties of the tissues may change with temperature, condition and frequency of the applied energy. Thus, voltage sources are not considered reliable power supplies. The alterations in the dielectric and conductivity properties of tissues inspired researchers to use current sources. By this method, applied current will remain constant while tissue characteristics vary. This methodology makes it possible that introduced energy can be adjusted in safety limits to avoid harm to the body. Current is either injected to the body or can be induced.

EIT applications diverge each other in many directions: the way of introducing energy, using a fixed frequency or multi-frequency studies, invasiveness, electrode configurations, simulation / experimental studies etc.

1.5.6.1 First Applications of EIT

It is almost a century that electrical properties of tissues are investigated. To characterize biological tissues, many different methods are used. Fricke and Morse (1926) have a well-known study. They cut the tissues into small, taken from 58 cases, cylindrical shapes and put them in a conductivity cell to make sure of electric current passed through the tissue [29]. It was observed that, biological tissues acted as a resistor in parallel with a capacitor.

Conrad, Haggard and Teare implemented a study, supporting Fricke and Morse's observations. Equivalent circuits for the frog and human tissues are investigated[30]. A rectangular current pattern is applied with changing intensity for any desired duration. Frog tissue showed purely resistive response, while human tissue was represented by a resistance with relatively high shunt capacitance.

As early as 1941, Kenneth S. Cole and Robert H. Cole [31] described a model, which explains the impedance behavior of the tissues.

$$\varepsilon^*(\omega) - \varepsilon_\infty = \frac{\varepsilon_s - \varepsilon_\infty}{1 + (i\omega\tau)^{1-\alpha}} \tag{1.7}$$

where ε^* is complex, ε_s and ε_∞ are the static and infinite dielectric constants respectively, ω is the angular frequency (rad/s), τ is the relaxation time (s) and α is a parameter between 0 and 1, giving the result of Deby for polar dielectrics. In the light of this model, it is observed that:

- At frequencies below 5 kHz, electrical current cannot penetrate into the cells, only flows in the extracellular fluid. Thus, tissue demonstrates resistive characteristics (Fig 1.4).

- As frequency increases, electrical currents begin to pass through the cells, yielding an increase in the capacitor behavior. This capacitance reaches to its peak value around 50 kHz as shown in Fig 1.5.
- At higher frequencies (>100 kHz), electrical current passes through the cells without any deflection, causing a decrease in the capacitive behavior.

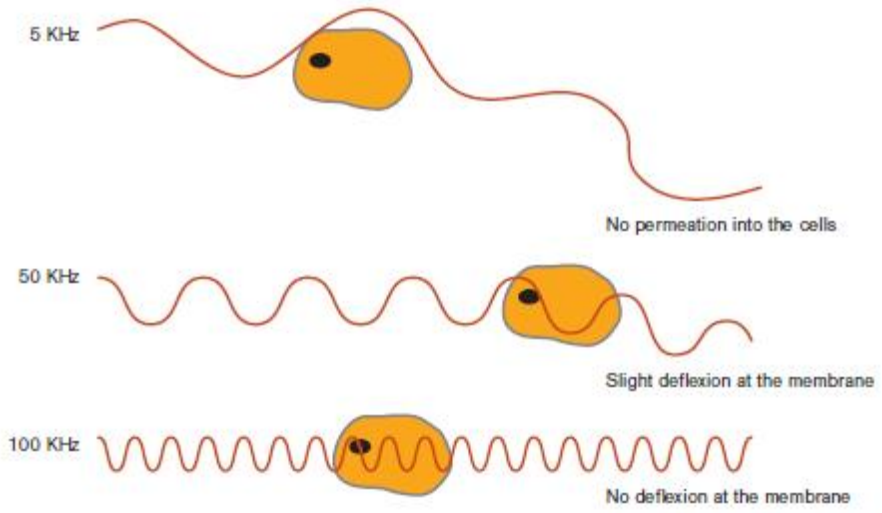

Figure 1.4 Electric pathways at different frequencies [32]

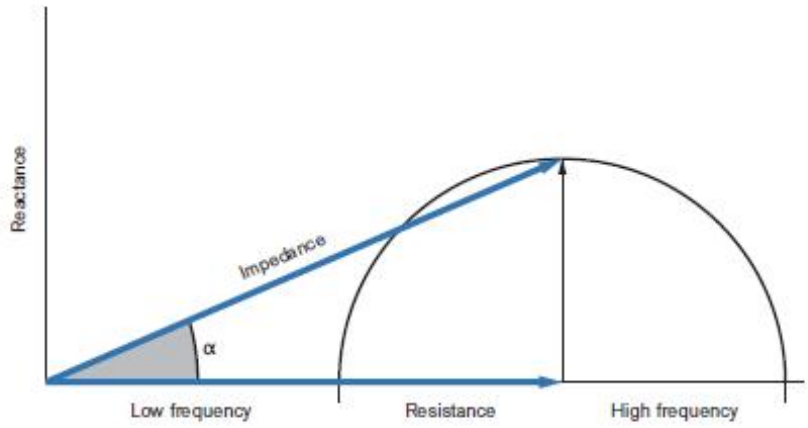

Figure 1.5 Cole & Cole plot: the effect of frequency on the impedance of biological tissues [32]

Another important study, carried out by Schwan, was published in 1958. The dielectric constant (ε) and conductivity (σ) (S/m) were analyzed as a function of frequency [33]. α and β dispersions were discussed in this wide-band, multi-frequency study (1 Hz – 20 GHz). Beta dispersion occurring in 0.1 – 10 MHz band, is due to the poorly conducting cell membranes that needs time to be charged. This band, will later be investigated in many publications, trying to emphasize the electrical properties of tissues

Tarjan and McFee measured the resistivity of human torso and head using magnetic induction. A time-varying magnetic field was generated, by applying a sinusoidal current to a coil. Induced electromagnetic field was measured with another coil [34]. Due to presence of a conducting object, currents are induced proportionally to the conductivity. Both excitation and recordings were implemented via contactless measurements, yielding electrodes unnecessary, resulting elimination of coupling problems.

1.5.6.2 Different Methodologies in EIT

In the applied-current electrical impedance tomography (ACEIT), current is directly injected to the body using electrodes and resulting voltage values are also measured by separate electrodes. For a specific electrode position, only one measurement is possible. For all the corresponding locations, a recording is made, and the voltage readings are inserted into a data matrix, which is known as the ¨forward problem in EIT¨. Then, the conductivity (or resistivity) values are reconstructed with image reconstruction algorithms, which is called ¨inverse problem in EIT¨.

In the induced-current electrical impedance tomography (ICEIT), current is induced to the body by generating time varying magnetic fields inside the body. Similar to ACEIT, electrodes are used to record the measurements. Major advantage of this technique is that, multiple recordings are possible by simply shifting the position of the electric field generator (i.e. coils), instead of changing the electrode positions.

The forward problem in EIT, has attracted many of the researchers. Gençer and Tek used magnetic excitation to introduce currents and reconstructed the conductivity distribution using finite element method [35]. The authors published another study implementing a similar technique. A modality is proposed to using contactless measurements. A time varying magnetic field, generated by the transmitter coil, induced currents in the tissue [36]. The receiver coil measures both the primary field (created by transmitter coil), and the induced field in the tissue. They reconstructed electrical conductivity of the tissues, where mathematical models of the procedure were explained in detailed.

Webster designed an impedance camera to image thorax in 1978. The camera could provide 100 pixels for a single image, where 32 frames taken per seconds [37]. They observed a change in admittance during forced respiration. They discussed the limitations of this very fundamental imaging device that some people consider, as the first medical EIT system.

In 1983, Barber and Brown proposed a method to image electrical resistivity [38]. They used 16-electrode current application configuration to measure voltage differences. Authors concluded that, this method could be used for many application areas (medical, geological etc.).

In the light of previous studies about tissue bio-impedance, Isaacson and his colleagues designed an instrument to acquire data from the internal body structures [39]. The instrument, using 32 electrodes, was able to apply any desired current pattern at 15 kHz, and measure the resulting voltage (maximum of 5 mA rms, for a 1000 Ω load).

Designing and building a highly accurate current source is a difficult task. However, a voltage source is easier to build and operate. Choi and colleagues presented an algorithm to apply multiple currents using voltage sources [40]. They recorded the

voltage sources that can provide the desired current patterns. Using this iterative algorithm, current was applied by simply adjusting the voltage characteristics.

Researchers have been trying to develop new methodologies and design new instrumentations to obtain more accurate EIT recordings (forward problem), while some others focused on the reconstruction techniques and algorithms (inverse problem). As in other imaging techniques, back projection algorithm is used to reconstruct the images in electrical impedance tomography. Murai and Kagawa implemented a simulation study using a finite element method to simulate the impedance field and sensitivity theorem to reconstruct the electrical conductivity [41].

In a similar study to Murai and Kagawa [41]; Gençer, Kuzuoğlu and İder investigated reconstruction algorithm using sensitivity matrix analysis [42]. They proposed a new reconstruction method based on minimization procedure.

Improper measurements may cause the reconstruction algorithms to fail. Mu and Wexler, proposed an excitation/measurement pattern algorithm to prove that the image quality depends on both the numerical features (electrode number) of EIT system and its topological structure [43]. Improvements on 2D EIT were observed, however in 3D imaging, still considerable error was present in deep layers.

1.5.6.3 Dielectric Properties of Tissues

It's been known that dielectric properties of biological tissues determined by charging of the cell membrane, and vary with the frequency. With the help of newly developed impedance imaging devices, wide-band studies using EIT became possible and popular. Surowiec and his associates presented a study on dielectric properties of breast carcinoma and surrounding tissues in 20 kHz – 100 MHz frequency range in 1988. Tumor samples from seven breast cancer patients are used [11]. Results of the experiments suggested that, all various samples (central part of

the tumor, surrounding tissue, normal breast tissue etc.) had an increase in conductivity and decrease in dielectric constant at higher frequencies. There was a slight increase in conductivity of the healthy breast tissue, on the other hand, tumor tissue showed a drastic elevation from 2 mS/cm at 20 kHz to 10 mS/cm at 100 MHz. Authors also reported different types of carcinomas could have varying dielectric properties, but average conductivity values of tumor tissues were 5 to 10 times higher than the healthy breast tissue.

Josinet, in 1996, observed the impedivity (equivalent of resistivity in AC) in normal and pathological breast tissues [44]. Jossinet examined 6 groups of breast tissues and measured the impedivity values for 0.488 Hz – 1 MHz. 120 specimen are collected from 64 patients. Author resulted that above 10 kHz, reduced standard error was found 0.1 or less. It was also expressed that for the breast tissue bio-electrical characterization, studies above 1 MHz were necessary.

Chauveau and his colleagues have also investigated the bio-impedance parameters at varying frequency values. They measured the normal and pathological tissue samples *ex vivo*, from 10 kHz to 10 MHz [45]. Extracellular, intracellular resistances and membrane capacitance were calculated. These data represented that cancerous tissue could be distinguished from normal tissues.

As Josinet concluded above, dielectric properties of the biological tissues up to microwave region should be obtained. There are many high frequency studies, focusing on this area. Joines *et al.* (1980), made *in vivo* measurements of mammary gland and tumor tissue from 22 rats [46]. An open-ended coaxial probe produced a field and the fringing field was detected with a directional coupler and an oscilloscope. Tumor showed 3 – 5 times higher conductivity than breast tissue for the frequency range of 30 MHz – 2 GHz at 37 ^{o}C.

Chaudhary and his associates in 1984, measured dielectric properties of normal and malignant breast tissues at frequencies, 3 MHz to 3 GHz [47]. Time domain

spectroscopy results of samples of 15 patients concluded slight difference to the study above [46], however consensus in malignant tissue having 3-5 times higher conductivity.

99 samples from 37 patients (39 of normal breast fat, 18 of benign tumor, 22 of glandular connective tissue, 22 cancer) was investigated at 3.2 GHz. Campbell and his colleagues used the changes in the resonant frequency to characterize the bioimpedance values [48]. Tumor tissues had higher conductivity values compared to other tissues.

Majority of the studies on electrical impedance experiments were performed *in vitro*. It was proven that impedance of tissues changes after death since permeability of cell membrane (b-dispersion characteristic) also changes. Consequently, the impedance of a living tissue and a dead tissue do not equal to each other [49]. To reveal this difference, *in vivo* experiments play crucial role. Morimoto and his colleagues performed an invasive study about breast tumors [50]. A precise-needle electrode was inserted into the tumor. Extracellular and intracellular resistance values, membrane capacitance are calculated in relevance with their model circuit. In conclusion, significant different in tumor and normal tissue was observed in 0 – 200 kHz frequency range.

In vivo measurements of impedance are obviously difficult. Probes used to achieve this goal are either invasive or noninvasive. Invasive probes are inserted into the tissue and current flow and voltage measurements are done via needles. Noninvasive probes use electrodes that are located surface of body region to be screened. Paulson *et al.* has a study about probe design for impedance measurement where errors due to the organ curvature and electrode contact impedance are reduced [51].

Özkan and Gençer published an experimental study, reconstructing the conductivity images of a leech (live worm) via contactless measurements [52]. At a relatively low

frequency (50 kHz), a 2D area was scanned. Inverse problem solved by using Steepest Descent Algorithm.

1.5.6.4 Clinical Applications

Imaging thoracic region with EIT has also been a densely focused area. Recent studies suggest that EIT can be used to monitor lung recruitment and detect lung collapse. Difference images are used, but only thoracic regional impedance change over time can be represented [53].

16 newborn pigs with acute lung injury, were investigated by a bronchoscope passing through mouth or nose into the lungs. This medical procedure is called ¨lavage¨. Frerichs *et al.* observed that lung injury causes the center of ventilation to move to the ventral end (front of the body, close to belly) [54]. They also showed for a treatment method if a compound, lowering the surface tension, was administrated, ventilation shifts back to the original position.

Lindren and associates used EIT to identify lung collapse [55]. Results from mechanically ventilated patients showed that imaging the reduction of the airway was possible. They also investigated volume-controlled and pressure-controlled ventilations, reaching to similar results. EIT provided sufficient data to determine the amount of collapse.

Pneumothorax is a complication caused by abnormal collection of gas in the pleural space that separates the lung and the chest wall. Costa *et al.* [56] proposed an algorithm to detect the changes in EIT signals associated with pneumothoraces and evaluate this signals in real-time. 39 animals were either injected air gradually increasing in amount or applied positive and expiratory pressure (PEEP) increments. With 100% sensitivity and 95% specificity rate, pneumothoraces as small as 20 mL were detected.

The TransScan TS2000, produced by Siemens Medical Systems, is a real-time non-invasive, 2D multi-frequency imaging device. The device can map the distribution of electrical impedance of tissues in the range of 50 Hz – 20 kHz. It applies a small alternating current, limited to 2.5 V and 5 mA due to safety regulations, via probes and a 16x16 array on a probe placed on the breast detects the impedance values [57]. TS2000 is the only commercial electrical impedance imaging device, approved by FDA (Food and Drug Administration) to be used as an adjunct to mammography for follow-up exams for cancer patients.

1.6 Conclusion

The idea of electro – thermal imaging arises from improving the image quality of infrared imaging with the help of multiple images. These desired images can be obtained by applying a stimulation at various frequencies.

This chapter focused on the high incidence and mortality rate of breast cancer. Even though mammography is widely used to detect breast cancer, it is inadequate to detect small tumors. This status of mammography was the origin of introducing a novel imaging modality [6].

Commonly used imaging techniques to detect breast cancer were briefly discussed in chapter 1. Various studies proved that hybrid imaging modalities provide higher sensitivity and specificity rates. Electro – thermal imaging was introduced to improve the image quality of infrared imaging in combination with conductivity imaging.

Studies showed that thermography can be used as a risk indicator for breast cancer. It also detects abnormalities in the tissue but the performance significantly decreases in deep regions. Biological tissues (healthy – malignant) have different electrical properties at different frequencies. Thus, introducing multi-frequency currents, different images can be obtained that shows different tissue characteristics.

CHAPTER 2

ELECTRO-THERMAL IMAGING

2.1 Introduction

This chapter describes the principles of electro-thermal imaging. In the first section, active thermography studies will be discussed, comparing them with electro-thermal imaging, underlining the advantages of this new modality. Subsequently, schematics of the modality and the fundamentals about the application will be presented. Then, definitions of the ¨passive¨ and ¨active¨ modes are explained in detail. In the following section, mathematical analysis of both modes will be derived to show the theoretical background. In the last section, an example will be solved to demonstrate the additional effect of electro – thermal imaging to the infrared imaging.

2.2 Active Thermography Studies

Living organisms are considered as sources of different signals, which are used for medical diagnosis. Infrared imaging (IR) is a well-known modality used in localizing the hot and cold spots (high / low metabolism). IR has many advantages. It is contactless (no interaction with tissues), fast and easy to use and has an attractive way of presenting the surface temperature distribution. Moreover, in recent years, detector technology in IR is significantly developed. Cameras with 0.01 ^{o}C thermal resolution, high speed (1000 frames/sec), high spatial resolution (more than 1 million pixels) are available. These state-of-the-art infrared cameras are used not only for diagnosis but also in medical procedures such as hyperthermia.

In 1972, Arthur W. Guy studied induced electromagnetic fields by using equivalent phantom models of biological tissues [58]. For the fat and bone tissue phantom models, dielectric constant is controlled with aluminum powder and conductivity by acetylene black percentage. A high water content phantom is used to model muscle tissue. Polyethylene powder percentage set the dielectric constant and conductivity value was adjusted by changing the salinity of the solution. These structures had the same internal field distribution of the biological tissues in the existence of an electromagnetic source. Guy used various source geometries to apply electromagnetic field, such as plane, dipole, and aperture, and compared the theoretical and observed heating patterns of the phantom models at different frequencies (circular cylindrical tissue, plane tissue layers, and irregular cylindrical tissues).

Kaczmarek and Nowakowski had an active thermography study, which they applied external power to phantoms. An electromagnetic field of 40 W, halogen lamps of 20x50 W, semiconductor and laser sources are used as stimulators. These studies proved that electromagnetic and optical excitations could be used for heating purposes (because of high heat penetration) however laser sources did now show any difference [59].

Microwave ablation can heat deeper regions of a tissue compared to RF currents. Bernardi and his colleagues, also used phantom models, investigated the temperature rise and SAR distribution by using a microwave cardiac ablation catheter [60]. Numerical tools based on finite-difference time-domain method were implemented. Experimental setup consisted of a cardiac catheter inserted into a two-layer heart model. Muscle tissue model was similar to Guy's phantom [58], with high water content. Authors tried to detect lesions located at different depths (1-9 mm depth), by applying radiated power for 60-120 seconds. Results showed that, a lesion at 5 mm with low blood perfusion was detected.

Mital and Scott presented a study aiming to determine the location and the generated power of a heat source placed in a cylindrical tissue phantom in 2007 [61]. Both sides of the cylinder were isolated, so that only the top surface was exposed to convection. An infrared camera with a 0.08^{o}C resolution was used during the experiments, in which setup was left out 4 hours to obtain a steady-state temperature field. Results indicated a good correlation with the estimated and actual depth and power parameters. Authors predicted the location of the heat source (maximum actual depth was 0.025 m) with an error margin of 0.004 m. Power estimations were even more accurate. Using 0.12 - 0.78 W sources, the prediction of the power generated by these heat sources was close to the actual values with 0.02 W error. They concluded that it was possible to estimate the depth and the generated power of the heat source with surface measurements. On the other hand if the source is located deep down the surface, temperature variations generated on the surface would be small and it would be more difficult to make a prediction of the exact location.

Active thermography studies are based on applying a hot or cold stress to the target and imaging the heat patterns with thermal camera. There are different methods in the application of the external stress, such as microwave, induction, light, air, etc. In 2003, Kaczmarek and Nowakowski used a set of halogen lamps as external sources (with 1000W electrical power) [59]. The lamps are placed 50 cm away from the target and pulse duration was 30 seconds. They examined 3 women (diagnosed breast cancer), and concluded that it was impossible to detect tumors using conventional passive thermography. It was only possible to locate the abnormalities in the breast with active thermography.

Researches prefer microwave heating because of its greater depth for detecting tumors. Tipa and Baltag applied microwave radiation in 10-12 GHz band, and observed a maximum of 2.5 ^{o}C difference between two breasts of the same patient [9]. Due to the symmetry of the breasts, 0.5 ^{o}C temperature difference is generally

accepted as normal condition. In this case, 5 times higher temperature difference between breasts, indicates an abnormal activity in the patient.

There are many active thermography methods, however application methods in medical area are reduced to basically microwave heating. Even though there are not many experimental studies, simulations using different active thermography sources are present. In 2010, Carlak and Gençer used a different approach in tumor detection [7]. In this simulation study, an additional low frequency current (5 mA, within safety limits) was applied in order to improve the imaging performance. Similarly, Bernardi had used microwave ablation to heat up the phantom models (mentioned previously [60]). This extra heat source caused an increase in the temperature difference between tumor and surrounding tissues, 0.083 ^{o}C for tumors at 5 cm depth and 0.433 ^{o}C for tumors at 0.5 cm depth). Finite element method simulation results show, a significant performance improvement, 70% for tumors close to the surface and 14% for located in deeper regions of the breast tissue.

Active thermography is not only used for diagnostic purposes but it is also important in cancer surgeries. Cancer hyperthermia method destroys cancer cells by heating the tissue. Radiofrequency (RF) and microwave (MW) electromagnetic radiation are popular techniques in order to accomplish this aim. The reason of this techniques being preferred to deliver heat to the cancer site is their relatively high (deep) penetrating. Cook and Pearce underlined that 50 seconds microwave exposure achieved almost 100% cancer cell death without any significant damage to the surrounding tissue [62].

In another study, Guo simulated 2D breast tissue as a semicircle of 10 cm diameter, including skin, breast fatty and glandular tissue and chest wall [63]. Simulations are conducted at 200-800 MHz band in order to locate a single 1 mm tumor and two 1.5 mm tumors below the skin. In conclusion, higher stimulation frequency provided better determination of the tumor location. Using active thermography in breast cancer diagnosis is a recently developed technique. There are not many patented

systems. Mammovision is the most well-known patent system, in medical active thermography area. Mammovision exposes the patient to cool air stress and records the thermal patterns of the skin just after breast temperature rises to the room temperature. The advantage of this technique is that it is possible to cool down the skin much lower temperatures without hurting the patient, compared to heating. In a study in which Mammovision was used on 114 patients from 2006 to 2007, this system detected 2 cancer patients for further examination where x-ray mammography failed to report them [4].

In addition to the medical use, there are several forms of active thermography. Each methodology may have different stimulation techniques. Smith (GEC-Marconi Limited) has a patent, using electromagnetic waves for active thermography [64], to detect hidden objects especially in a baggage at an airport. A resistive surface is placed between the thermal imager and the object. EM waves penetrating this surface, reflect from the object. Instead of the actual object, the thermal image on the surface is recorded.

2.3 Structures of Electro – Thermal Imaging

Electro – thermal imaging differs from ordinary thermal imaging by means of additional heat source (Fig 2.1). An infrared camera is located at a distance to the patient. Thermal images of the patient are obtained in two different modes.

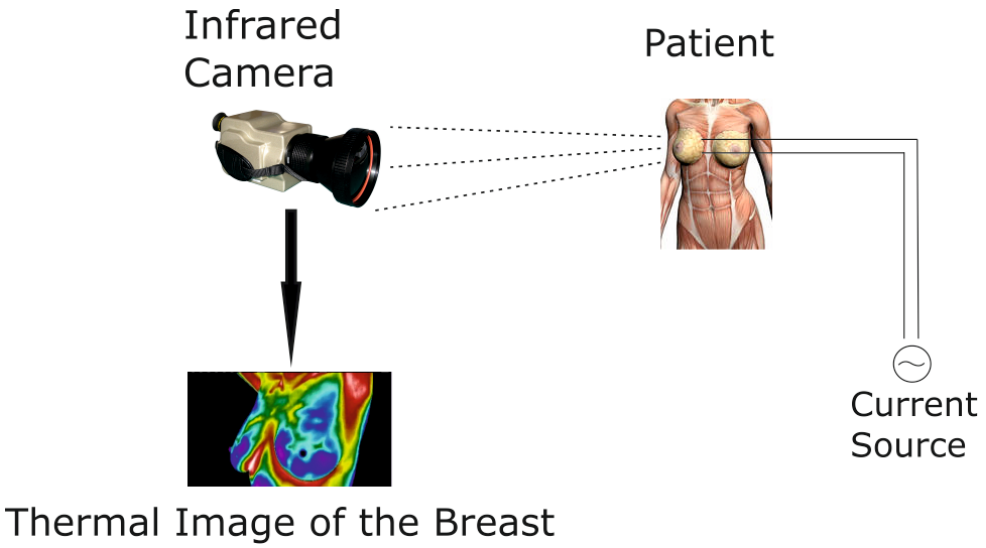

Figure 2.1 Schematics of the Electro – Thermal Imaging. In ¨passive¨ mode, current source is off. In ¨active¨ mode, sinusoidal current is applied to the patient.

In the first mode of operation, i.e., the ¨passive¨ mode, patient is imaged without any additional heat sources (classical thermography). These images are called ¨passive¨ images. Thermal distributions on the skin surface in ¨passive¨ images are caused by blood perfusion, and metabolic heat generation of the internal tissues and organs.

In ¨active¨ mode, a time-varying current (within medical safety limits) is applied to the patient, and the body is imaged. These, ¨active¨ images display the effects of both internal and external sources. Tumor tissue has higher conductivity than surrounding (healthy) breast tissues, generating a low-resistive pathway for the current to flow. Thus, applied electric current tends to flow through the cancerous tissue.

2.4 Analysis of the ¨Passive¨ Mode

In 1948, Harry H. Pennes proposed the first analytical bio-heat transfer model, describing the thermal distribution of the human tissue [65]. He tried to determine

the applicability of the heat flow theory to the biological tissues, aiming to evaluate the rates of tissue heat production and blood volume flow.

$$\rho c \frac{\partial T}{\partial t} = k \nabla^2 T \tag{2.1}$$

Equation 2.1 shows the fundamental time dependent heat transfer relation. Pennes recorded the radial thermal distributions in the forearm by using a thermocouple. Temperatures of the skin, rectal and brachial artery were also measured. He added a term, describing the effect of the blood flow, to the heat equation. Considering the effects of blood perfusion and the metabolic heat generation of the tissues, Pennes bio-heat transfer resulted as in equation 2.2.

$$\rho c \frac{\partial T}{\partial t} = k \nabla^2 T + q_b + q_m \tag{2.2}$$

Where, ρ is the density (g/cm^3), c is the specific heat (cal/g^{o}C), k is the thermal conductivity (cal/s cm ^{o}C), T is the temperature (^{o}C), q_b is the blood perfusion term (cal/s$\cdot$cm^3) and q_m is the metabolic heat generation (cal/s$\cdot$cm^3).

Pennes suggested the thermal equilibrium of tissues, in the above form. This model is widely used to describe thermal behavior in biological tissues since it accurately specifies temperature change (decay) from the body core to the skin surface. Pennes' major contribution was that the heat transfer rate between blood and tissue is proportional with the volumetric perfusion rate and the difference between the arterial blood temperature and the tissue temperature.

$$q_b = w \rho_b c_b (1 - k)(T_a - T) \tag{2.3}$$

Where, q_b is the heat transfer rate per unit volume (cal/s$\cdot$cm^3), w is the blood perfusion rate per volume of tissue (s^{-1}), ρ_b is the density of blood (g/cm^3), c_b is the

specific heat of blood (cal/g^{o}C), k is a coefficient that determines the incompleteness of the thermal equilibrium $0 \leq k \leq 1$, T_a is the arterial blood temperature (^{o}C) and T is the temperature of the tissue (^{o}C).

In the analysis, it is assumed that thermal equilibrium is reached, so that k~0 [66]. The term due to the blood perfusion equation 2.3 can be simplified as follows:

$$q_b = w\rho_b c_b (T_a - T) \tag{2.4}$$

In some studies [67], blood perfusion is written as a modified version of the equation 2.4, with an addition of porosity term (ε) for sponge-like tissues (like *corpus cavernosum*). Due to the insufficient literature data and the need of advanced mathematical modeling of the tissue geometry, this term is generally omitted (equation 2.5).

$$q_b = w\rho_b c_b \varepsilon (T_a - T) \tag{2.5}$$

If equation 2.4 inserted in the q_b term, equation 2.2 can now be expressed as in the following form:

$$\rho c \frac{\partial T}{\partial t} = k\nabla^2 T + w\rho_b c_b (T_a - T) + q_m \tag{2.6}$$

Equation 2.6 shows the relation of heat transfer in biological tissues. At steady-state (thermal equilibrium), T denotes the equilibrium temperature of the tissue in ¨passive¨ mode ($T_{passive}$). However the model of the body's thermal system is not complete unless the heat transfer from the body to the surroundings is not considered. Mechanisms of the heat transfer to surroundings are:

- conduction
- radiation
- convection

- evaporation (sweating)

Conduction to the air can be ignored because gases (air) have very low thermal conductivity. Consequently there will not be any significant heat transfer by conduction

The rate of heat transfer by radiation to surroundings, is defined by Stefan-Boltzmann Law:

$$q_r = \sigma_s \varepsilon (T_s^4 - T_{env}^4) \tag{2.7}$$

where q_r is the heat loss by radiation per unit area, σ_s is the Stefan Boltzmann constant, ε is the emissivity of the skin surface, T_s is the body surface temperature, T_{env} is the temperature of the environment (surrounding). The emissivity of the human skin is close to 1 (~0.98), since in infrared region skin behaves like close to a black body.

Draper and Boag used an approximation, claiming that difference between skin surface and environmental temperature is very small compared to the mean temperature, $T_m = \frac{1}{2}(T_s + T_{env})$ [68].

$$q_r = 4\sigma_s \varepsilon T_m^3 (T_s - T_{env}) \tag{2.8}$$

where

$4\sigma_s \varepsilon T_m^3 = h_r$, h_r is the radiative heat transfer coefficient and h_r =6.1±0.2 $Wm^{-2}K^{-1}$.

Convection is the heat loss at skin surface due to liquid or gas movement. There are two types:

Free convection: air flows caused by air intensity differences, generated by high skin temperature

Forced convection: air flow generated by external sources

Heat loss for both types of convection, is calculated by using the same relation.

$$q_c = h_c(T_s - T_{env}) \tag{2.9}$$

where q_c is the convection heat loss per unit area of the skin surface, h_c is the convective heat transfer coefficient, T_s is the body surface temperature, T_{env} is the environmental temperature. The convective heat transfer coefficient depends on surface geometry of the skin, physical properties of air, and the rate of air flow across skin. Rice observed that, h_c varies from 2.1 to 5.6 $Wm^{-2}K^{-1}$ and h_c =3.6$Wm^{-2}K^{-1}$ for 10^oK difference between surface and surrounding temperature [69].

At room temperature, normal human does not sweat much if he/she is not doing physical exercise. However, in real case, body loses its heat through evaporation (perspiration) insensibly. This is a process that water close to the body surface diffuses, and evaporates to the environment by taking the heat of the skin. The amount of this heat loss is expressed as in the following relation.

$$q_e = h_{fg} m(p_s^* - p_{env}) \tag{2.10}$$

where, q_e is the heat loss per unit area due to evaporation, h_{fg} is the heat of evaporation, m is the skin permeation coefficient, p_s^* is the saturated water vapor pressure at skin temperature (Pa) and p_{env} is the water vapor pressure at surrounding temperature. Draper and Boag revised this relation [68], and accomplished to make it similar to radiation and convection heat flow equations (as energy flow is proportional with temperature difference and a coefficient). According to this assumption, $h_e \approx 0.8$ $Wm^{-2}K^{-1}$.

At the surface – air boundary, the boundary condition can be written as:

$$k\frac{\partial T}{\partial z} = h(T_s - T_{env}) \tag{2.11}$$

where $h = h_r + h_c + h_e$ is the combined heat transfer coefficient for radiation, convection and evaporation, $\frac{\partial T}{\partial z}$ is the change in the local temperature in the z-axis (normal axis to the surface).

Brown concluded that h could be used directly to calculate total heat loss per unit surface area [70], where

$$h = h_r + h_c + h_e \approx 11 \text{ Wm}^2\text{K}^{-1} \tag{2.12}$$

2.5 Analysis of the ¨Active¨ Mode

In the ¨active¨ mode of electro-thermal imaging, a voltage controlled current source is used to apply external heat to the breast tissue. With the addition of the new source, the heat equilibrium equation should be modified as:

$$\rho c\frac{\partial T}{\partial t} = k\nabla^2 T + q_b + q_m + q_{ext} \tag{2.13}$$

Where q_{ext} is the external heat energy (by current source). q_{ext} is calculated by Joule Heat Equation.

$$q_{ext} = \frac{1}{\sigma}|J|^2 \tag{2.14}$$

where σ is the electrical conductivity (S/m) and J is the electrical current density (A/m^2) of the applied source.

In ¨passive¨ mode, the equilibrium temperature ($T_{passive}$) is calculated by using equation 2.6. The resulting T value of the equation 2.13 gives the equilibrium temperature of the ¨active¨ mode (T_{active}). The effect of the external heat source is calculated as

$$\Delta T = T_{dynamic} - T_{static} \tag{2.15}$$

ΔT is the temperature difference caused by additional heat source. Instead of solving 2 equations, equation 2.13 can be solved only in transient mode.

$$\rho c \frac{\partial T}{\partial t} = k\nabla^2 T + w_b \rho_b c_b (T_a - T) + q_m + q_{ext} \tag{2.16}$$

Equation 2.16 is the expanded version of 2.13, generated by inserting variables of q_b (blood perfusion rate) term. If equation 2.16 is further expanded:

$$\rho c \frac{\partial T}{\partial t} = k\nabla^2 T + w_b \rho_b c_b T_a - w_b \rho_b c_b T + q_m + q_{ext} \tag{2.17}$$

It is obvious that, $w_b \rho_b c_b T_a$ and q_m (metabolic heat generation) terms have the same effects on both ¨passive¨ and ¨active¨ mode of operation. Consequently, these terms are vanished in transient analysis, reducing the relation to

$$\rho c \frac{\partial T}{\partial t} = k\nabla^2 T - w_b \rho_b c_b T + q_{ext} \tag{2.18}$$

In uniform regions, $\nabla \cdot \nabla T = 0$, yielding

$$\rho c \frac{\partial T}{\partial t} = -w_b \rho_b c_b T + q_{ext} \tag{2.19}$$

Temperature difference created by external source can now be calculated by simply solving the equation 2.19.

$$T(t) = \Delta T(1 - e^{-\frac{t}{\tau}}) + T_0 \tag{2.20}$$

where $T(t)$ is the temperature at an instant, T_0 is the initial temperature, ΔT is the difference between the steady-state and initial temperature, and τ is the time constant of the tissue. It is obvious that ΔT represents the additional temperature difference caused by external heat source.

Using the assumption (equation 2.20), ΔT

$$\Delta T = \frac{q_{ext}}{\rho_b c_b w_b} \tag{2.21}$$

and the time constant (τ)

$$\tau = \frac{\rho c}{\rho_b c_b w_b} \tag{2.22}$$

are calculated.

Pennes only described the bio-heat transfer in the ¨passive¨ mode. However, in the ¨active¨ mode, electrical distributions generated by the external source should be derived. Coupled partial differential electromagnetic equations are as follows.

$$\nabla^2 \vec{A} - j\omega\mu(\sigma + j\omega\varepsilon)\vec{A} - \mu(\sigma + j\omega\varepsilon)\nabla\phi = 0 \tag{2.23}$$

$$\nabla \cdot [(\sigma + j\omega\varepsilon)\nabla\phi] + \nabla(\sigma + j\omega\varepsilon) \cdot j\omega\vec{A} = 0 \tag{2.24}$$

where $\vec{A}$ is the magnetic vector potential, ω is the angular frequency, μ is the permeability, σ is the conductivity, ε is the permittivity and ϕ is the scalar potential.

When a time-varying sinusoidal electrical current is applied to the region (A is the source, B is the sink) as in figure 2.2, the boundary conditions need to be considered yields as:

$$\sigma \frac{\partial \phi}{\partial n} = \begin{cases} I & \text{on A} \\ -I & \text{on B} \\ 0 & \text{otherwise} \end{cases} \tag{2.25}$$

Where I is the applied current from the nodes and n is the unit vector, normal to surface.

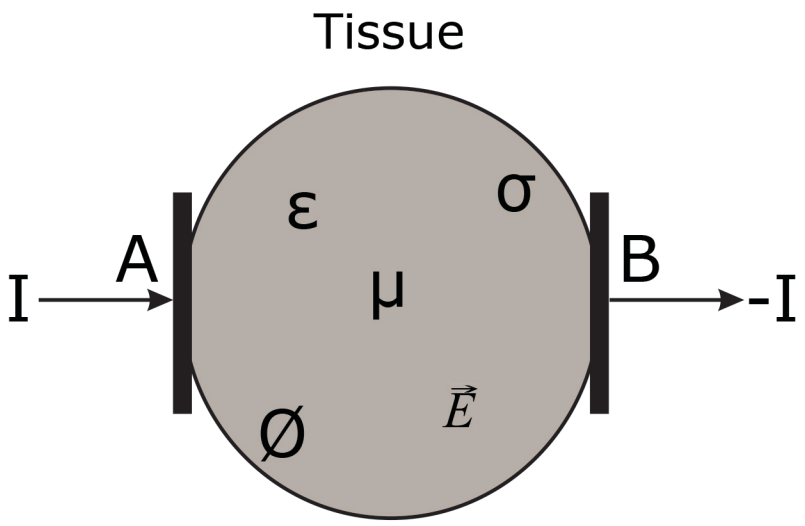

Figure 2.2 Electromagnetic model of electro – thermal imaging. $\vec{E}$ is the electric field, ε is the permittivity, σ is the electrical conductivity, μ is the permeability, ϕ is the scalar potential, A is the current source, B is the sink.

The generated electric field (equation 2.26) due to the current source can be calculated by using the equations 2.23 and 2.24. Considering the boundary conditions (equation 2.25).

$$\vec{E} = -j\omega \vec{A} - \nabla\phi \tag{2.26}$$

The electromagnetic model of the electro – thermal imaging with the boundary conditions is shown in the figure 2.2.

2.6 Numerical Example

The bio-heat relation of the tissues in ¨active¨ mode is described in the previous section. In the light of this knowledge, temperature difference between the ¨passive¨ and ¨active¨ modes, can be calculated by using the equation 2.21. And the electrical and thermal properties of the tissues given in table 2.1.

Table 2.1 Electrical and thermal properties of healthy and cancerous tissues [27,71,72]

	Healthy Tissue	Cancerous Tissue
Tissue density, ρ, (kg/m^3)	~1000	~1000
Specific heat of tissue, c, (J/kg^{o}C)	3000	4200
Density of blood, ρ_b, (kg/m^3)	1060	1060
Specific heat of blood, c_b, (J/kg^{o}C)	3770	3770
Blood perfusion rate, w_b, (m^3/sm^3)	0.00018	0.009
Arterial temperature, T_a, ^{o}C	37	37
Thermal conductivity, k, W/m^{o}C	0.42	0.42
Electrical conductivity, σ, S/m	0.2	1
Metabolic heat generation, q_m, W/m^3	450	~30000

In Carlak's Ph.D thesis [6], a maximum of 5 mA of sinusoidal electrical current was applied. Literature studies, presented in the chapter 1, suggest that the average value of electrical conductivity of the cancerous tissue is ≈ 1 S/m. Hereby, the power per unit volume applied by the external current source is calculated as

$$q_{ext} = 25000 \frac{W}{m^3} \tag{2.27}$$

Equation (2.20) describes the relation between the temperature rise due to the external sources. Using the tumor tissue parameters given in Table 2.1, temperature difference is found.

$\Delta T = 0.695^{o}C$

This is a significant increase in the temperature considering that state-of-the-art infrared cameras have a NETD of ~20-30m^{o}C.

Table 2.2 Radiation, convection and evaporation heat loss model parameters [70]

Parameter	Value
H	11 W/m^{2o}K
A_s	0.0325 m^2
T_s	310 ^{o}K
T_{env}	298 ^{o}K

Total heat loss per unit area due to radiation, convection and evaporation is united in the equation

$$q = h(T_s - T_{env}) \tag{2.28}$$

where $h = h_r + h_c + h_e$. If uniform heat loss from the surface is considered, total heat loss will be

$$q = hA_s(T_s - T_{env}) \tag{2.29}$$

where A_s represents the surface area. Using the equation (2.29) and the parameters of the breast tissue given in Table 2.2, total heat loss can be calculated as 4.3 W. Metabolic heat generation differs, 5-64 kW/m^{3}depending on the stage of the cancer. In simulation studies, q_m is considered as 29000-33800 W/m^3, in [27] and [72], resulting an average of 30000 W/m^3. This heat loss from the skin surface is really small compared to 30000 W/m^3 metabolic heat generation and 25000 W/m^3 external power source. Thus, it is neglected in the calculations and simulations in the literature studies.

2.7 Conclusion

In this chapter, Pennes' Bio Heat Equation is analyzed. Final form of the bio heat relations is presented, starting from the fundamental equation. In the presence of an additional heat source, the effect on the temperature elevation in cancer tissue is both analytically and numerically calculated. It is concluded that this extra temperature difference has a significant value and also can be detected by modern infrared cameras. The heat loss from the skin surface is also obtained both analytically and numerically. However, it is neglected in studies since the value of heat loss is really small compared to other heat generating sources (both internal and external). Tissue parameters in the numerical analysis are widely accepted values in literature, and also used in many simulation studies.

CHAPTER 3

CURRENT SOURCE

3.1 Introduction

Chapter 3 discusses the design and realization of a voltage controlled current source (VCCS) for multi-frequency electro-thermal imaging. This chapter is divided into five sections. In the first section, the requirements of the current source for electro thermal imaging are explained. In the second section, a literature research on the available current sources is presented. Following sections describe the problem, analysis, simulation (LT Spice) and implementation procedures, and present the characteristics and performance of the current design. The last section summarizes the results obtained by the analysis, simulations and implementation, and discusses the discrepancies.

3.2 Requirements for the Current Source

In active thermography, the general idea is to deliver external power to the patient, trying to create an additional contrast between cancer and surrounding (healthy) tissue. There are various ways of delivering this power and electrical current is one of these methods. In general, both voltage and current sources can be used for this purpose. In medical area, usually current sources are preferred. The current level applied to human body is restricted, i.e., it should be lower than the safety limits. According to the standard EN 60601-1 [73], for operation frequencies between 10 kHz and 1 MHz, the current should be between 1 -10 mA peak to peak (p-p).

Specifications for the current source design include many aspects. The aim is to design a current source that delivers the desired power to the tissue in a specific frequency band. Based on different considerations, the following criteria should be satisfied:

- The current intensity should be as large as possible without exceeding the safety limits (determined by EN 60601-1).Thus, our goal is to design a current source that can deliver a maximum current level of 10 mA p-p (via 1 cm^2electrodes)and operating between 100 kHz and 1 MHz frequency band.

- Output current should be controlled by input voltage.

The output impedance Z_{out} must be much higher compared to the tissue impedance Z_{tissue}. Z_{out}>100xZ_{tissue}should be satisfied over the whole operating frequency range. High output impedance is important to ensure that the current is independent of the load (tissue and contact impedances) and constant in magnitude.

Table 3.1 Safety Current Limit (EN60601-1 Standards) (mA peak-to-peak)

Frequency	Current Limit
0.1 Hz – 1 kHz	100 µA
1 kHz – 100 kHz	frequency/10 µA
> 100 kHz	10 mA

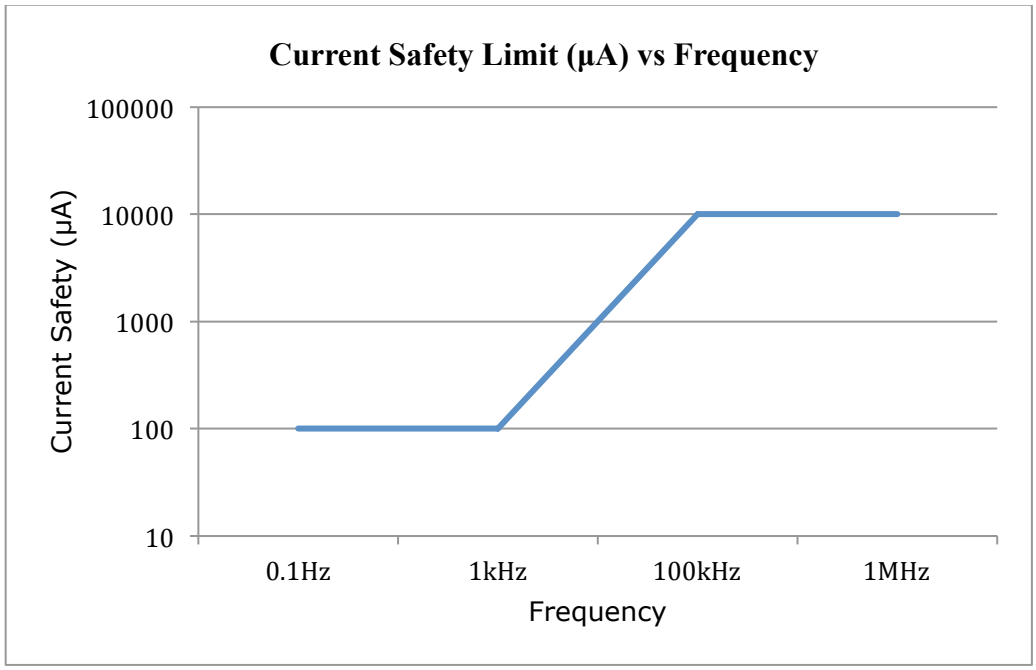

Figure 3.1 Safety current limit (EN60601-1 Standards) (µA peak-to-peak)

3.3 Available Current Source Technologies

Before approaching to design a current source, a general literature research on electrical impedance tomography systems should be made. Since the current is applied through the chest, EIT current sources must satisfy similar requirements. Technical features, possible problems and proposed solutions are concluded from those papers.

3.3.1 General Literature Search in Current Sources

There are many simulation studies carried out in last 30 years, but some of these topologies are preferred to implement. Research documents of MedIT group [74], discusses developed systems:

- Current mirror topologies
- Howland current pump

- Wideband transconductance amplifier
- Tietze topology

The performance of all these types of current sources depends on the design requirements. In our design the following specifications should be satisfied:

- High output impedance considering the load around 1.5 kΩ
- Constant current magnitude just below safety limit (~10 mA peak to peak)
- Operating on a wide frequency band (100 kHz – 1 MHz).

According to various studies, Tietze and Howland topologies have the best performance over the whole frequency range. For this reason, these two topologies are examined in the following section and a comparison made for further selection of the topology.

Previous studies show there are various custom current source designs. In Yang's design using microcontroller, only 140 μA can be injected to the load in the desired frequency range [75]. Solmaz achieved a 800 μA current over 100 kHz – 1 MHz frequency range, however the design is only successful for low loads (up to 1kΩ) [76]. Liao had the same drawbacks of Solmaz's study, it was possible to deliver only 1 mA current to 239Ω load [77].

Besides custom designs, Tietze and Howland topologies are widely used, analyzed and implemented. Zhangyong and his colleagues have a simulation study on various VCCS models and they concluded that Howland topology has the highest output impedance (1 MΩ) over a wide frequency range (up to 1 MHz), thus it is more suitable compared to other current sources [78]. Wang also underlines that Howland circuit is widely applied in EIT system design due to its simple structure, superior driving capability and feasible implementation [79]. It is also noted that the output performance of this model significantly decreases due to parasitic and stray capacitor as the operating frequency increases. However, in kHz – MHz frequency

range, it still has the best stability capability according to the authors. Simulation results show that 1 mA current can be injected to a 10 kΩ load from 1 kHz to 1 MHz.

In Abad's study Tietze and Howland topologies are both discussed and simulated in detail [74]. It conclusion, both current sources have similar characteristics in means of high output impedance, output current intensity and stability. Tietze topology has lower current magnitude error (0.76%) compared to Howland (2.6%), on the other hand Howland shows greater output impedance (13 MΩ for Howland, 7 MΩ for Tietze).

Another simulation study is done by Bouchaala and his colleagues that compares Tietze and Howland sources [80]. The results provide improvement in the current magnitude error. It is calculated as 0.089% and 0.058% for Tietze and Howland, respectively. It is also added that current magnitude of Tietze is not kept constant for a large load comparing to Howland.

Howland current source is a widely accepted and commonly used VCCS in EIT area. However, even in a machine interface for wheelchair control systems may use Howland topology as a current source. Yunfei, designed a system which controls a wheelchair by human body movements [81]. Body segment movement changes the bio impedance, and with the help of 50 kHz, 0.5 mA AC current, this bio impedance change is recorded.

3.3.2 Tietze Topology

The first topology to be analyzed is the Tietze current source [82]. This current source has two cascade operational amplifiers (Fig 3.2).

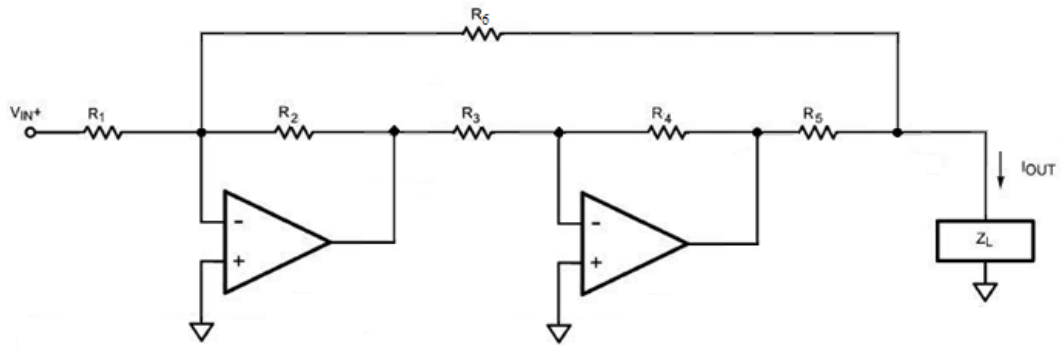

Figure 3.2 Schematics of Tietze Current Source

After a simple derivation, the output (load) current of this current source as in the following relation:

$$i_L = V_{in}\frac{R_2R_4}{R_1R_3R_5} + V_L\frac{1}{R_5R_6}\left(\frac{R_2R_4}{R_3} - (R_5 + R_6)\right) \tag{3.1}$$

It is obvious that, in order to have an ideal current source (independent of the load) the following matching equation must be satisfied:

$$\frac{1}{R_5R_6}\left(\frac{R_2R_4}{R_3} - (R_5 + R_6)\right) = 0 \tag{3.2}$$

which simply equals to:

$$R_2R_4 = R_3(R_5 + R_6) \tag{3.3}$$

The above equation would make the current source ideal and perfect if and only if the operational amplifier is ideal. However, it actually is not. On the other hand the matching criteria is not affected with the non-ideality of the operational amplifier. The relation still needs to be satisfied to have high output impedance. The simulation model of Tietze topology in LT Spice simulator is done considering the

mentioned requirements. The output current as a function of the input voltage is expressed as:

$$i_L = V_{in} \frac{R_2 R_4}{R_1 R_3 R_5} \tag{3.4}$$

3.3.3 Howland Current Pump

The other current source to be analyzed is the Howland current pump. This topology is similar to Tietze, using only one operational amplifier instead of two. The circuit configuration is shown in Fig 3.3 [83].

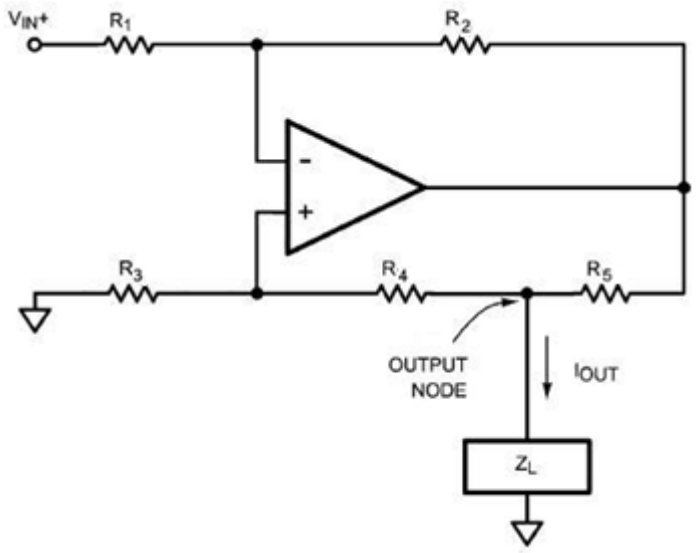

Figure 3.3 Schematics of the Howland Current Source

The load current is calculated as in the following equation:

$$i_L = -V_{in} \frac{R_2}{R_1 R_5} + V_L \left(\frac{R_3}{R_4 (R_3 + R_4)} + \frac{R_3 (R_1 + R_2)}{R_1 R_5 (R_3 + R_4)} - \frac{R_4 + R_5}{R_4 R_5} \right) \tag{3.5}$$

As in the Tietze current source, matching the resistors is important to obtain ideal behavior. In this model, the following equation should be satisfied to adjust current independent of the load:

$$\frac{R_3}{R_4(R_3+R_4)}+\frac{R_3(R_1+R_2)}{R_1R_5(R_3+R_4)}-\frac{R_4+R_5}{R_4R_5}=0 \tag{3.6}$$

which simply equals to:

$$R_2R_3=R_1(R_4+R_5) \tag{3.7}$$

In the light of this resistor matching, output (load) current is only dependent to input voltage as follows:

$$i_L=-V_{in}\frac{R_2}{R_1R_5} \tag{3.8}$$

3.3.4 Literature Review Summary

Design of multi-frequency current source is an active research area for many years. There are various designs available. Some authors made custom designs for the current application. On the other hand, many other researchers modified available current source topologies. The most popular topologies are Tietze and Howland as they provide high output impedance and high current stability in kHz-MHz bandwidth. Both current sources operate in similar ways (having equal positive and negative feedback) and have close output performance. Howland provides higher output impedance. Thus, for high loads (~2 kΩ in our case), Howland is more suitable. The aim is to design a 10 mA peak-to-peak current source up to 1 MHz. Since there is not any study that strongly proves Tietze outlines Howland current source, Howland current source is chosen for the design.

3.4 Parameters to Analyze for Implementation

Majority of the studies that analyze current sources are simulation studies. Even in the designs that implement the circuit practically, frequency response of the system is not analyzed. In the previous section, Tietze and Howland topologies are compared assuming the operational amplifier is ideal, as in literature studies. Authors only comment on the stray and parasitic capacitance effects at high frequencies which may degrade the driving capability. However, these capacitance values are important and determine the characteristics of the current source at high frequencies, dominantly. In this section, these effects are analyzed and the effect on the overall performance is calculated.

3.4.1 Mathematical Model

Figure 3.4 shows the non-ideal model of an operational amplifier, used in the analysis:

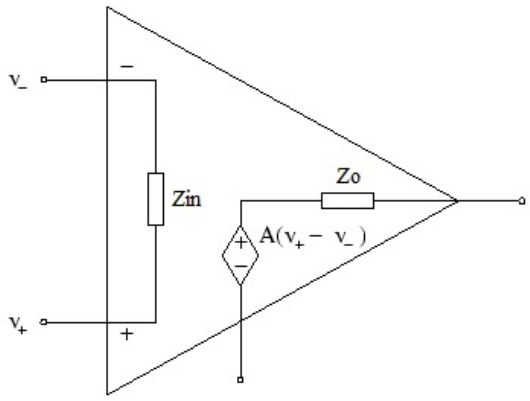

Figure 3.4 Non-ideal operational amplifier model

This non-ideal model is integrated in Howland current source, and characteristics are obtained. Frequency response (transfer function) and output impedance of the system is calculated as:

$$\frac{i_L}{V_{in}} = -\frac{[(2Z_{in}A - r - 2Z_0)R^2 + R(Z_{in}rA - r^2 - 3Z_0r - 2Z_{in}Z_0) - Z_0r(1+Z_{in})]}{4(r+Z_0)R^3 + (Z_{in}(2rA+4Z_0) + 3r^2 + (6Z_0+4Z_{in})r)R^2 + R[Z_{in}r(rA+2Z_0) + 2(Z_0+Z_{in})r^2] + Z_{in}r^2} \tag{3.9}$$

Equation 3.9 is complex and difficult to analyze the effects of the variables. It can be simplified as follows:

$$\frac{i_L}{V_{in}} = -\frac{2Z_{in}AR^2 + Z_{in}rRA}{4(r+Z_o)R^3 + 2Z_{in}rA + Z_{in}r^2RA} \tag{3.10}$$

The output impedance is calculated by short circuiting the input terminal V_{in} and connecting a test voltage source at the output node terminal of the current source. The relation for Z_{out} is shown in eq (3.11):

$$Z_{out} = \frac{4(r+Z_0)R^3 + (Z_{in}(2rA+4Z_0) + 3r^2 + (6Z_0+4Z_{in})r)R^2 + R[2Z_0r^2 + Z_{in}((A+2)r^2 + 2Z_0r)] + Z_{in}r^2}{4R^3 + R^2(6r + 4(Z_0+Z_{in})) + R[2r^2 + 4((Z_0+Z_{in})r + Z_0Z_{in})] + Z_0r(r+2Z_{in})} \tag{3.11}$$

where

Z_{in} is the input impedance of the operational amplifier

Z_o is the output impedance of the operational amplifier

A is the open-loop gain

w_{c0} is the 3-dB frequency of the open-loop gain

R and r are the chosen resistor values.

Similar to the transfer function of the system, output impedance relation also needs to be simplified:

$$Z_{out} = \frac{4(r+Z_o)R^3 + 2rZ_{in}AR^2 + Z_{in}(A+2)r^2R}{4R^2Z_oZ_{in}} \tag{3.12}$$

Z_{in} is modeled as in Fig.3.5. For simplicity it is assumed that input impedance is a parallel combination of a resistor and a capacitor. ($Z_{in} = R_{in} // c_{in}$)

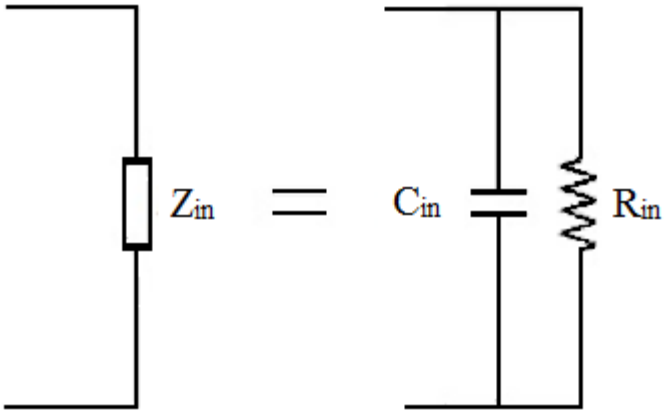

Figure 3.5 Equivalent model for input impedance of the operational amplifier.

It is desired to design a current source operating up to 1 MHz. So, the pole of the system should be larger than maximum operating frequency. The pole of the transfer function is calculated as:

$$w_{p1} = \frac{4R^3(r+R_o)+R^2(2R_{in}rA+4R_{in}R_o+3r^2+6R_or+4R_{in}r)+R(R_{in}r^2A+4rR_oR_{in}+2r^2R_o+2R_{in}r^2)+r^2R_oR_{in}}{(R_{in}C_{in}+\frac{1}{w_{c0}})(4R^3(R_o+r)+3R^2r^2+6R^2rR_o+2RR_or^2)} \tag{3.13}$$

$$w_{p2} = \frac{4R^3(r+R_o)+R^2(2R_{in}rA+4R_{in}R_o+3r^2+6R_or+4R_{in}r)+R(R_{in}r^2A+4rR_oR_{in}+2r^2R_o+2R_{in}r^2)+r^2R_oR_{in}}{\frac{R_{in}C_{in}}{w_{c0}}(4R^3(r+R_o)+3R^2r^2+6R_orR^2+2RR_or^2)} \tag{3.14}$$

It is difficult to understand the effect of each of these variables on the poles. These complex equations need to be simplified for a better understanding of the effect of each term. The literature survey suggests a single cut-off frequency for the current source. Thus, the first pole is assumed to be the dominant pole and further simplification and analysis is only done for the first pole. The following equation is the simplified version of pole 1:

$$w_{p1} \cong \frac{R_{in} rA(2R+r)}{(R_{in}C_{in} + \frac{1}{w_{c0}})(4R^2(R_o + r))} \tag{3.15}$$

For this purpose, the following graphs are plotted. These plots show the individual effect of each parameter on the system. Since w_{p1} is assumed to be the dominant pole, only w_{p1} is considered in the following sections.

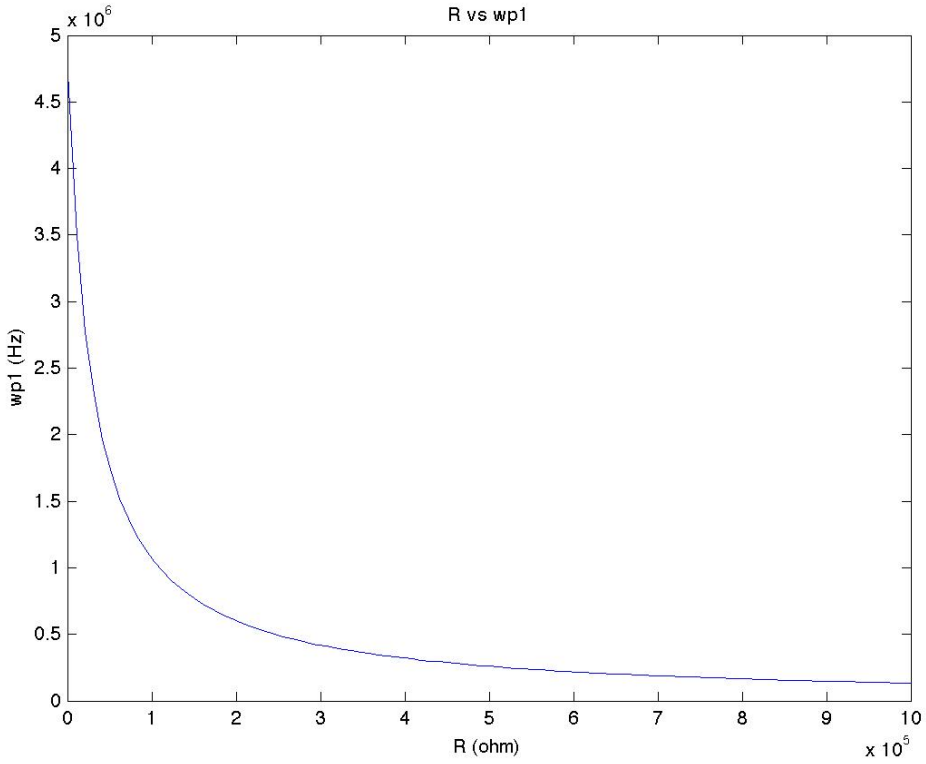

Figure 3.6 Resistor R, effect on pole 1 frequency. As R value gets larger, pole frequency of the system becomes smaller.

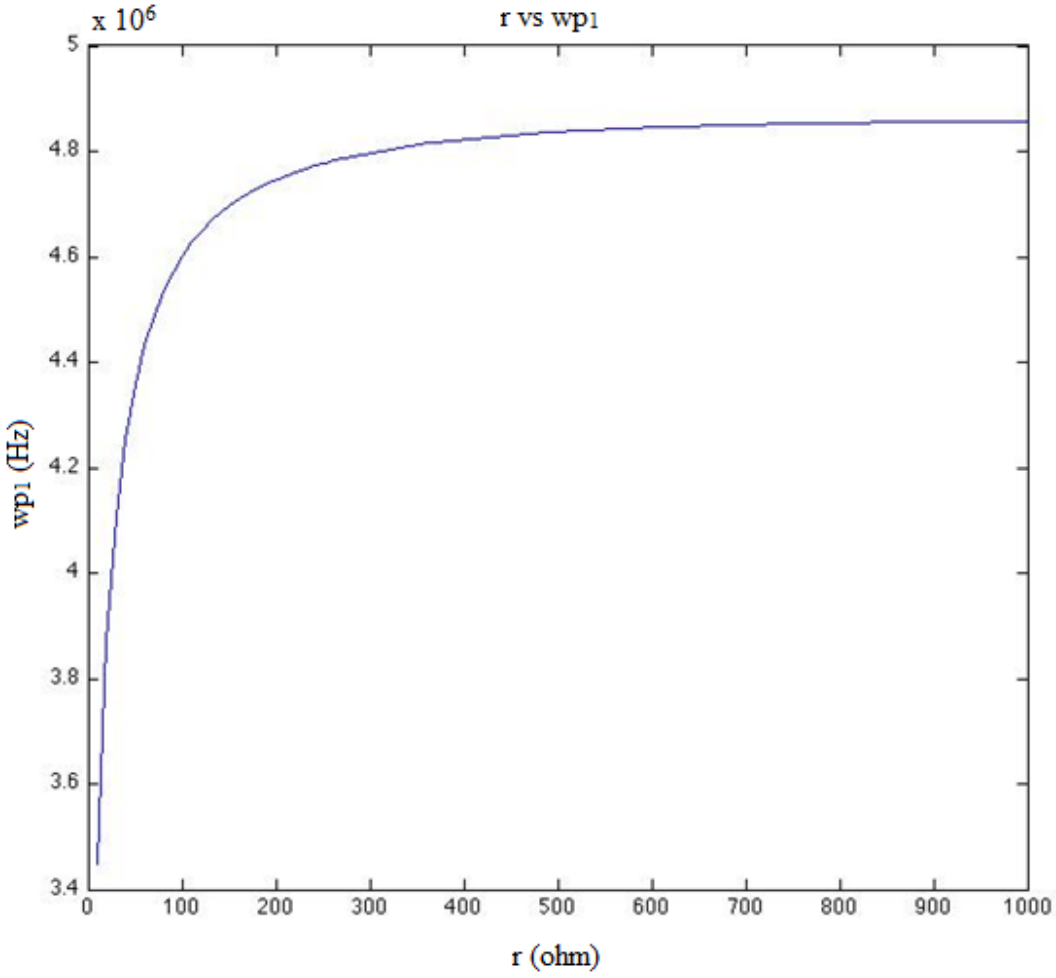

Figure 3.7 Resistor r effect on pole 1 frequency. If r value is higher than 100 Ω, system will have large pole location.

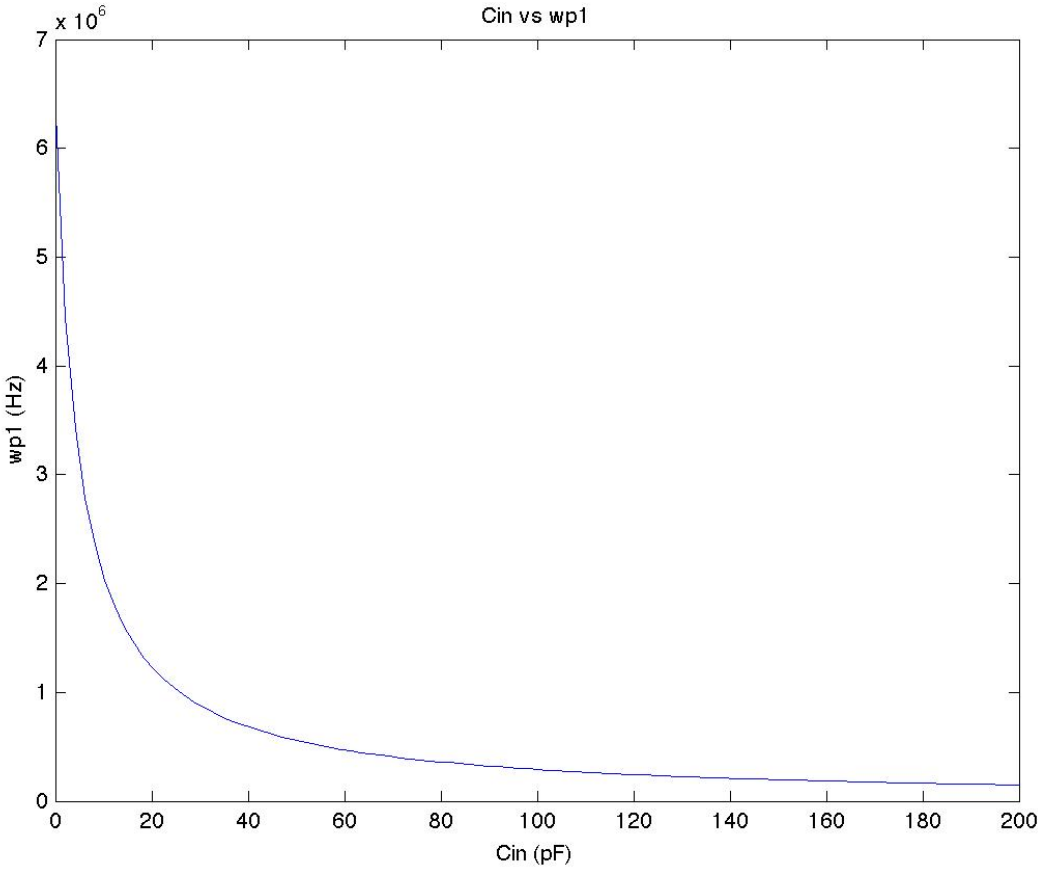

Figure 3.8 Input capacitance of the operational amplifier (C_{in}) effect on pole 1 frequency. As the capacitance increases, the pole of the system gets smaller

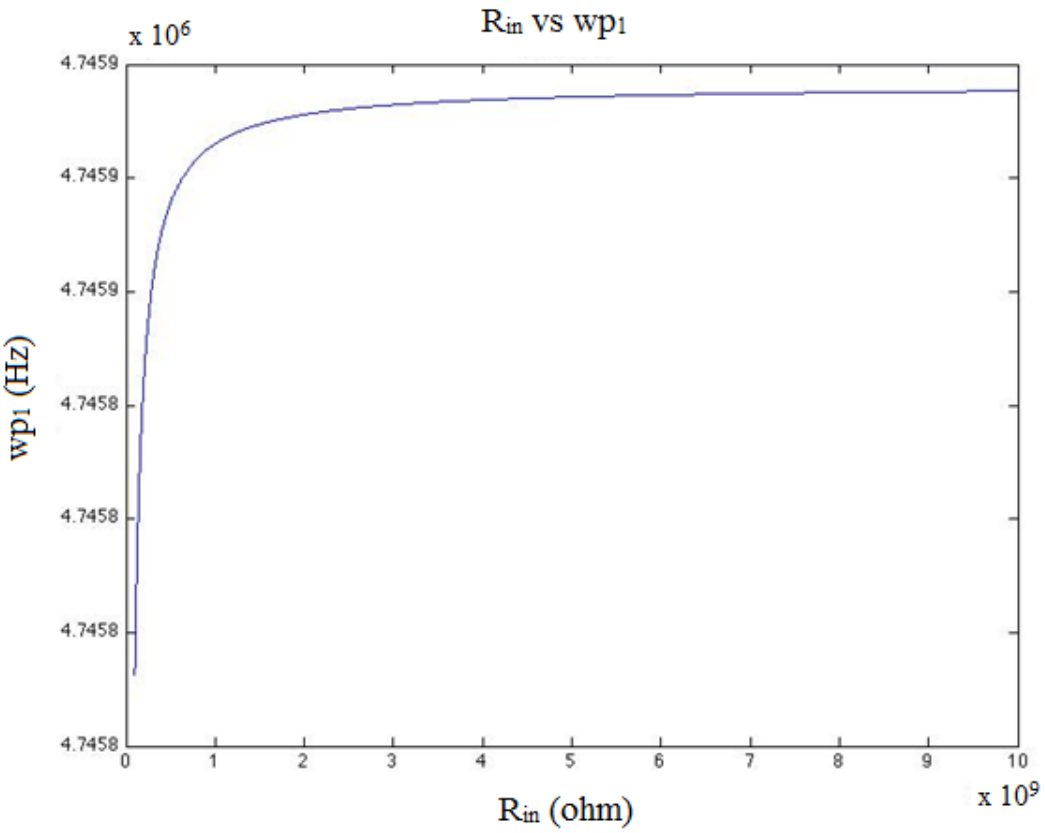

Figure 3.9 Input resistance of the operational amplifier (R_{in}) effect on pole 1 frequency. R_{in} should be larger than 1 GΩ, to have a high pole value

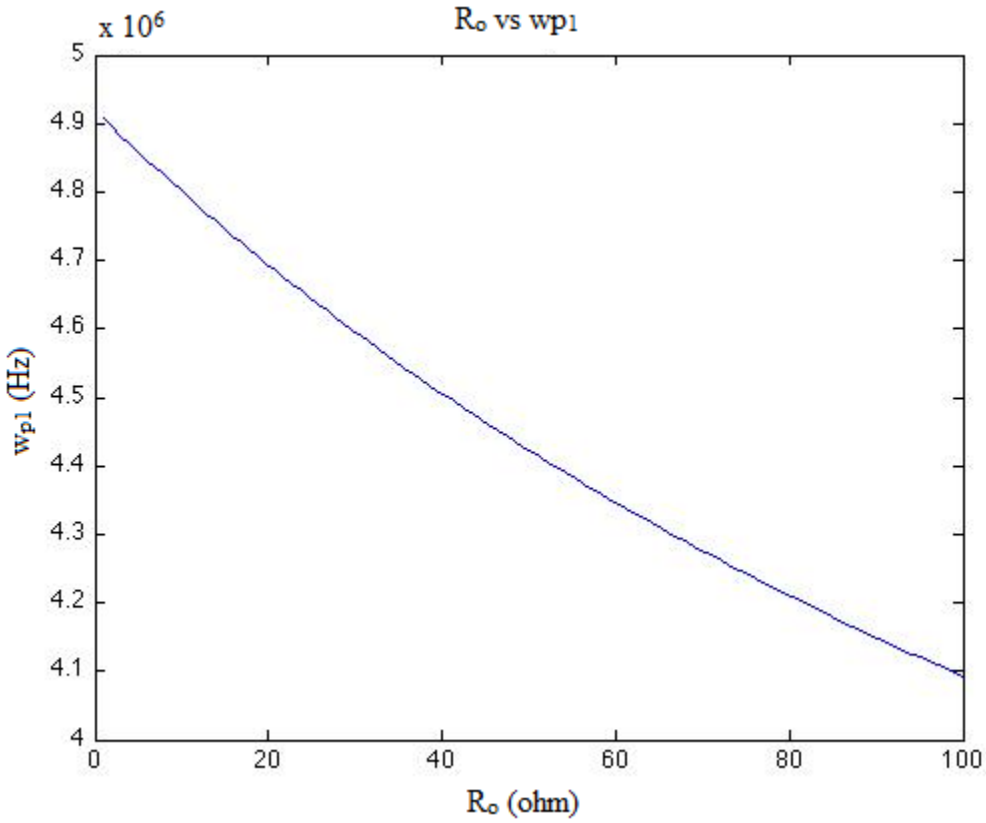

Figure 3.10 Output resistance of the operational amplifier (r_o) effect on pole 1 frequency. ro value should be as low as possible in order to have a high pole location

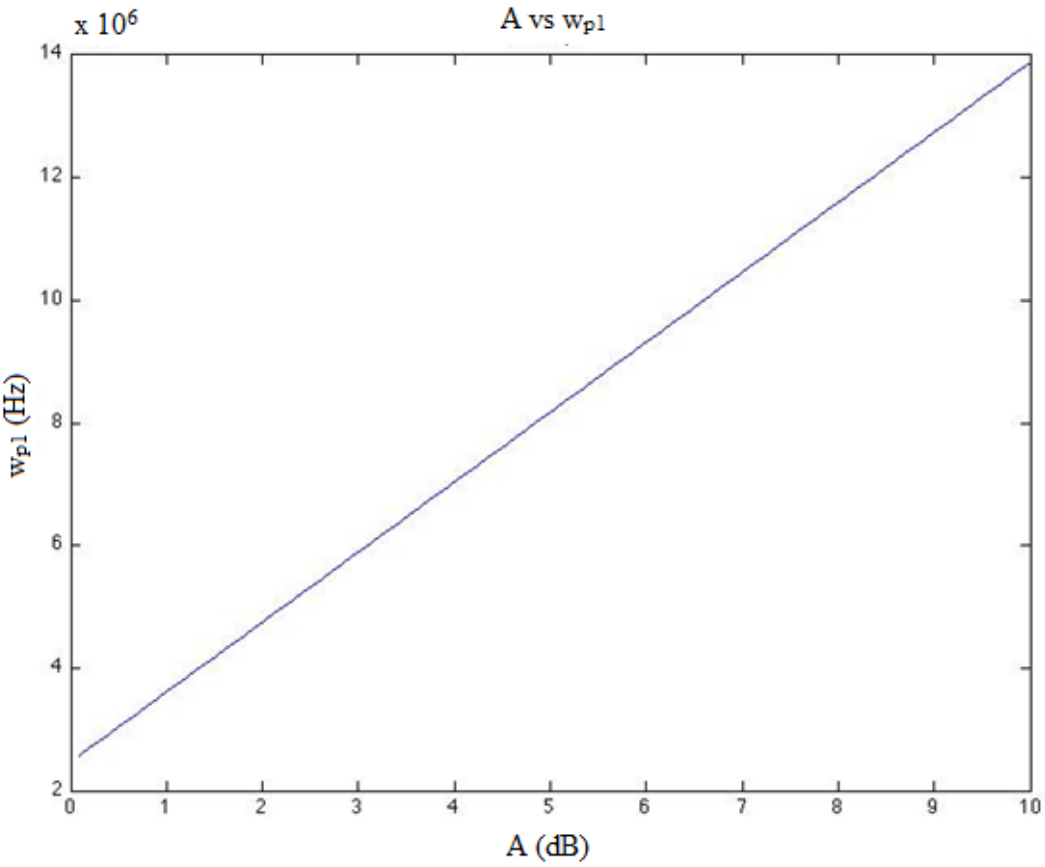

Figure 3.11 A (open-loop gain of the operational amplifier) effect on pole 1 frequency. The greater A value suggests, higher pole frequency

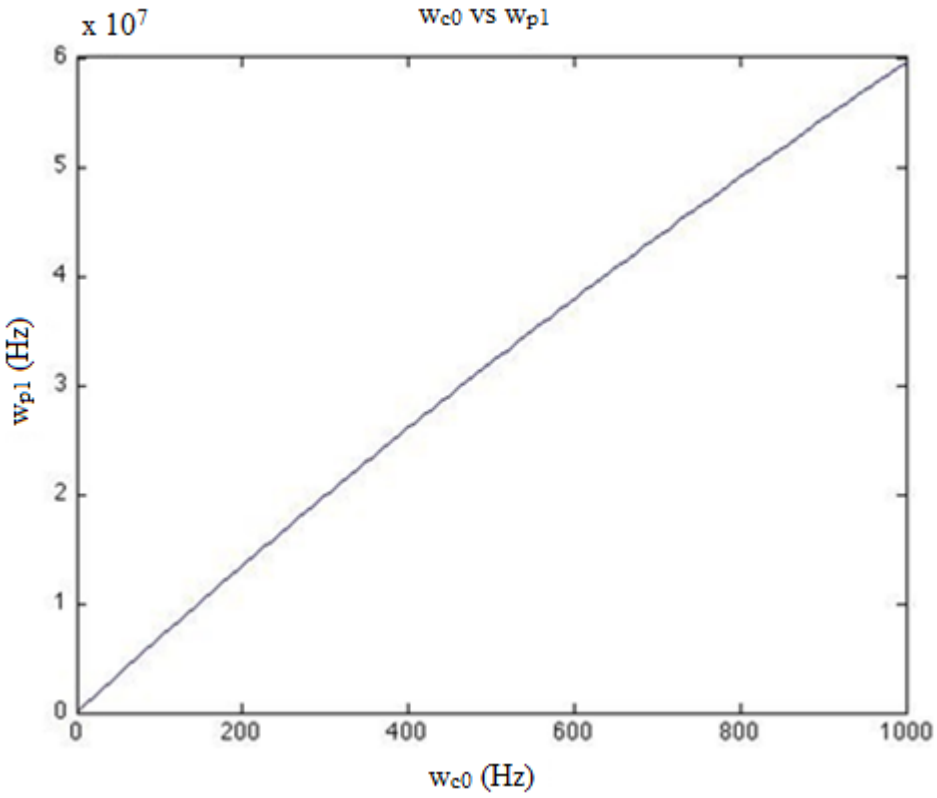

Figure 3.12 3-dB frequency of the operational amplifier (w_{c0}) effect on pole 1 location. For a better frequency response, w_{c0} should be as high as possible.

These plots will be used to determine the general characteristics of the pole of the transfer function as the variables are changed. In a single plot, all other variables are kept constant at a random value to show the effect of that specific parameter on the system. Thus, it can be concluded how the pole behaves at different parameter values, however the pole values on the y-axis do not represent any significant information on the pole frequency. Further analysis is available in the following sections.

3.4.2 Internal Parameters

The phrase ‘internal parameters’corresponds to parameters of the operational amplifier. These parameters are fixed unless a different commercial product

(opamp) is used in the system. Plots in the previous section show that these parameters should satisfy the following conditions:

- the smaller c_{in} gets, the pole becomes larger.
- the greater R_{in}, the pole becomes larger
- A (open-loop gain) should be high, so pole becomes larger
- w_{c0} obviously should be high
- R_o must have as small value as possible

In the use of this knowledge, from the available products operational amplifier AD8034 is selected, and used in the rest of this chapter. The datasheet [84] suggests that:

C_{in}: 1.7 pF
R_{in}: 1000 GΩ
R_o: 30 Ω
A: 92 dB
W_{c0}: 7.2 kHz

These parameters confirm that AD8034 can be used for our design. 21 MHz Gain-Bandwidth product suggests, if poles of the system are adjusted in high precision, it is possible to design a wide-band multi-frequency current source that injects desired current.

3.4.3 External Parameters

External parameters represent the two different resistor values. The plots suggest, both values should be as low as possible. However, determining the pole of the system is not the only requirement.

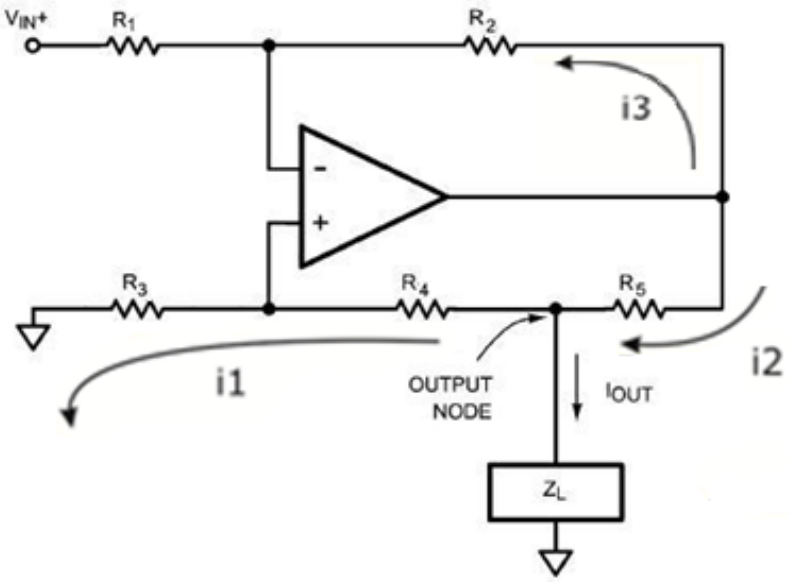

Figure 3.13 Schematics of the Howland Current Pump.

Figure 3.13 is helpful to visualize different current pathways affecting the load current. If the currents are defined as shown, then it is evident that load current equals to

$$i_{out} = i_2 - i_1 \tag{3.16}$$

where i_1 is the current flowing across the feedback resistors R_3 and R_4, i_2 is the current flowing across R_5, i_3 is the current flowing across the feedback resistors R_1 and R_2. When the load (R_L) in increased, V_L is increased in the same ratio, simply by elevating the currents i_1 and i_2. Feedback resistances R_3 and R_4 sense the change in the V_L, and shifts V^+ terminal of the opamp upwards. Operational amplifier tries to equate V^- to V^+ terminal, by increasing current across R_1, which is i_3. If load is decreased, feedback resistors shift V^+ terminal downwards, to decrease the output current of the operational amplifier. By arranging i_1 and i_2, shifting up or down synchronously, i_{out} is kept constant.

Resistor R, changes the power dissipation in the system. When R gets smaller, power converted to heat on these resistors is elevated, because of the increase in the current flowing across. It is also preferred that the desired high current only is delivered to the load, and rest of the components does not drive high values. In Howland current source design, operational amplifier output current is the sum of i_2 and i_3. For the chosen resistor matching, i_1=~i_3. Consequently;

$$i_{opamp} = i_{load} + 2i_1 \tag{3.17}$$

If resistor R is selected in the order of 1 kΩ, i_1~5 mA, this choice degrades the current leveldelivered to the load. In order to maintain 5 mA load current, current flowing in the rest of the circuit should be maximum of 1 mA. For these reasons, R is used as 10 kΩ.

Resistor r, determines the limit of the load current. Operational amplifier output note should not be higher than 11.9 V. This potential is:

$$V_o = V_r + V_L \tag{3.18}$$

If voltage difference across the resistor r is small, it is possible to have high value at load node, corresponding to high load current delivery. However, making r too small causes problems in adjusting the output current. $R_1 = R_2 = R$ is selected so the output current is inversely relation only with r.

$$i_L = \frac{V_{in}}{r} \tag{3.18}$$

If r is too small, in the order of 10 Ω, it is obvious that Vin=50 mV is required to deliver a maximum of 5 mA to the load. Very low reference voltage yields to difficulty in trimming the load current. For a 1 mA output is controlled by only 10

mV source. In many studies, r is selected in the order of kΩ, however according to equation (3.16), this is not feasible in our design.

For 2 kΩ load, highest current level is adjusted as 5 mA, resulting a maximum of 10 V load voltage. Thus, voltage difference across the resistor r, should be lower than 1.9 V, according to the equation 3.16, where ~6 mA current is flowing through. For these reasons r is chosen 200 Ω, resulting ~0.7 V voltage margin for the whole current source.

3.5 Results

In this section, results of the current source design are provided. First, analytical results are presented. In the following sub-section, simulation results are presented for the same design. In the last part, experimental realization of the current source on printed-circuit board is given.

3.5.1 Analytical Results

These results are obtained using the mathematical models discussed previously. The frequency response of the system (Eq.3.9) is obtained by using MATLAB.

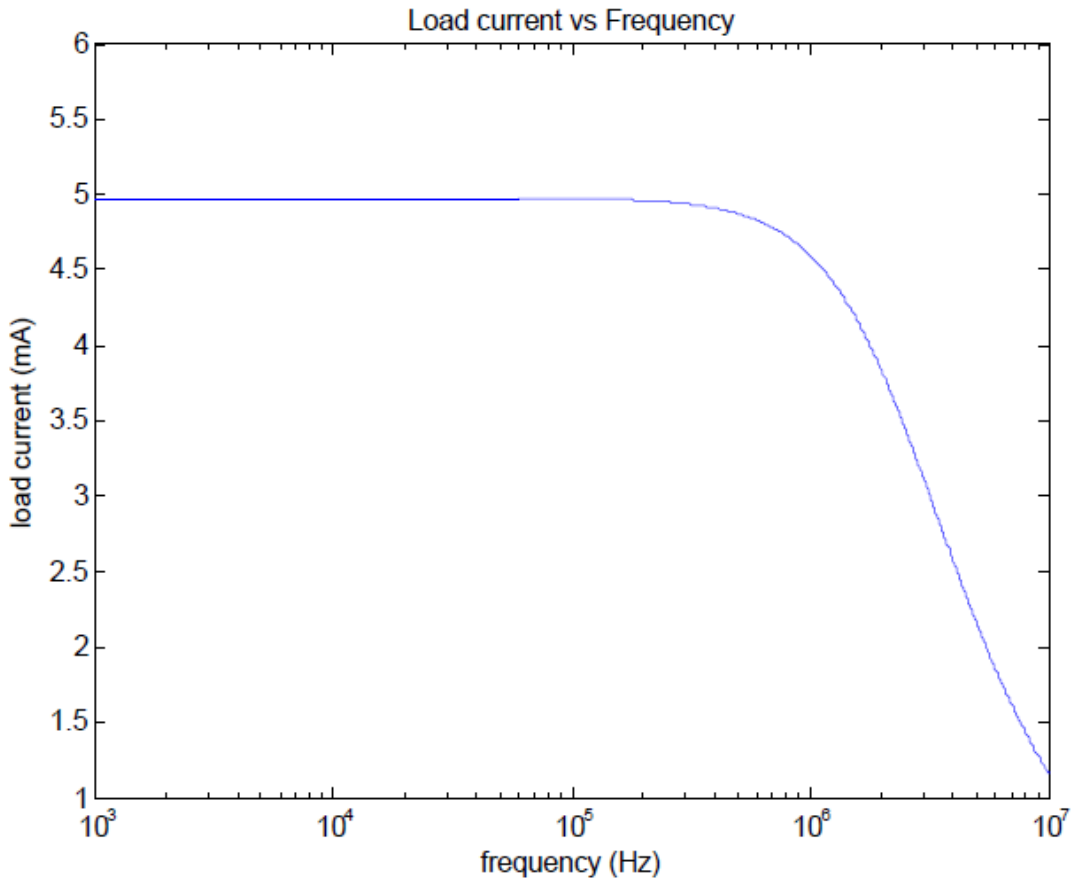

Figure 3.14 Frequency response of the load current

Pole equations of the system are given in equations (3.13) and (3.14). The effects of these parameters were discussed in previous section and the values for the optimized characteristics are calculated. According to those relations, the pole is calculated analytically. The resulting 3-dB frequency and cut-off frequency of the current source:

W_{p1}=6.82 Mrad , f_{c0}=1.08 MHz
W_{p2}=8.9 Grad, f_{c0}=1.41 GHz

The second pole is much greater than the first pole (>10 times), thus first pole is dominant and determines the frequency characteristics of the system. This

calculation proves the assumption made in the previous sections that only the first pole fixing is sufficient for adjusting frequency response.

3.5.2 Simulation Results

This section provides the simulation results of the designed current source. LT-Spice IV program is used to obtain the graphical results (waveforms and frequency characteristics).

3.5.2.1 Total Harmonic Distortion

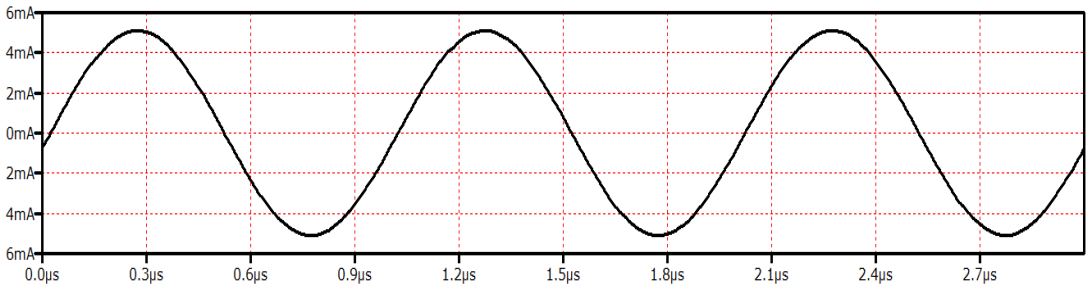

Figure 3.15 Load current waveform at 1 MHz for 2 kΩ load resistance.

The load current is checked if there is any distortion at the load waveform and also to confirm opamp is operating in the linear region. The output waveform does not show any signal distortion. However, calculating the total harmonic distortion gives additional and more detailed information about the output signal.

Total harmonic distortion (THD) is a measurement of the distortion in the signal. It simply is the ratio of the sum of the powers of the higher harmonic frequencies, to the power of the first harmonic.

$$THD = \frac{\sum_{i=2}^{\infty} P_i}{P_1} = \frac{P_2 + P_3 + P_4 + ..+ P_\infty}{P_1} \qquad (3.17)$$

The load will be driven by the current is in the order of 1.5-2kΩ. THD is calculated for the load 2 kΩ, at different frequencies. Table 3.2 shows that the maximum value of THD is -51 dB at 1 MHz.

Table 3.2 Total Harmonic Distortion values of the current source

Frequency	Total Harmonic Distortion
10 kHz	-59 dB
100 kHz	-56 dB
1 MHz	-51 dB

3.5.2.2 Frequency Response of the Simulation Study

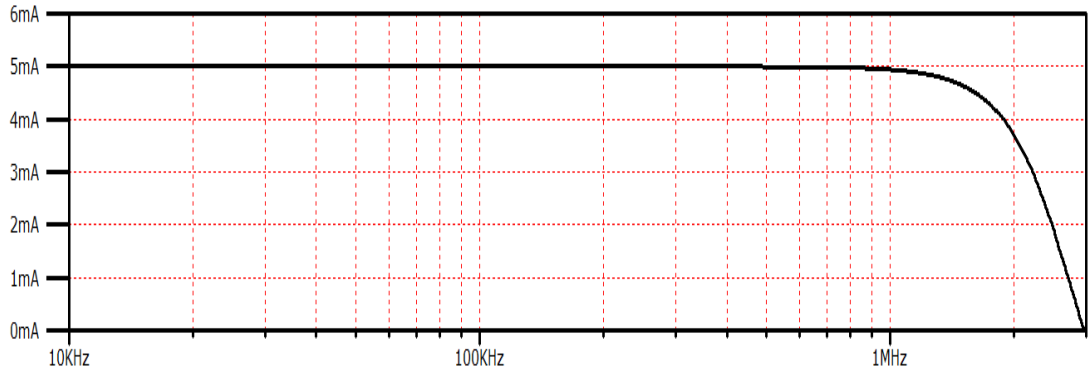

Figure 3.16 Frequency response of the current source for 2 kΩload

3 dB frequency of the system is measured as:

w_{3dB}=7.4 Mrad

$f_{cut\text{-}off}$=1.17 MHz

Calculated cut-off frequency in the simulation study confirms the analytical value of the analytical study (1.08 MHz). It can be concluded that the approach used in the analytical study provides close results to the simulation study. Combining the results of analytical and simulation study, it is possible to obtain a similar frequency characteristics in the real implementation of the current source.

3.5.2.3 Output Impedance of the Simulation Study

Z_{out} is a critical measure of determining the ideality level of an amplifier. The following circuit is used to calculate the output impedance:

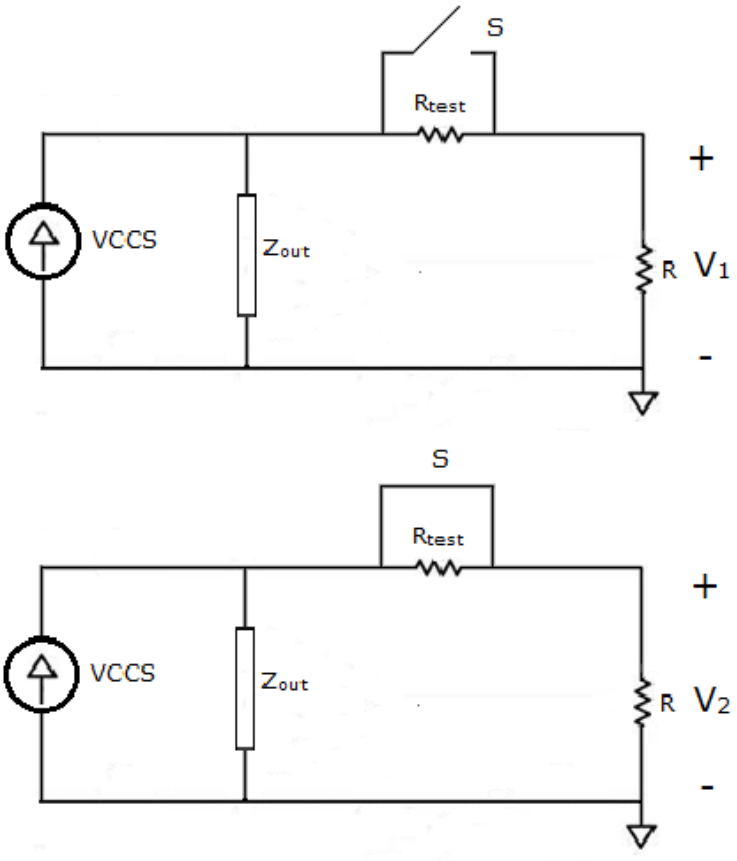

Figure 3.17 Schematics of the circuit used to measure Z_{out} , S is the switch.

The output impedance of the current source, is calculated by the following equation.

$$Z_{out} = \frac{R_{test}}{\frac{V_2}{V_1} - 1} - R \qquad \text{(Eq. 3.18)}$$

where, Z_{out} is the output impedance of the current pump, R_{test} is a test resistance, R is the load resistance, V_1 is the voltage across R when the switch is open and V_2 is the voltage across R when the switch is closed. Table 3.3 and figure 3.18 show the output resistance values with varying frequency.

The schematic of the output impedance measurement circuit (figure 3.17) is used for the determination of the output impedance of the simulation study. The change in the output voltage (or current) for different loads, determine the output impedance of the current source. The results are shown in the following table:

Table 3.3 Output impedance value of the current source at different frequencies for the simulation study

Frequency (Hz)	Output Impedance (Ω)
10k	6.42M
20k	5.89M
30k	5.62M
40k	5.51M
50k	5.30M
60k	4.99M
70k	4.68M
80k	4.30M
90k	3.99M
100k	3.54M
200k	2.49M
300k	1.50M
400k	935k
500k	622k
600k	438k
700k	354k
800k	285k
900k	239k
1M	211k

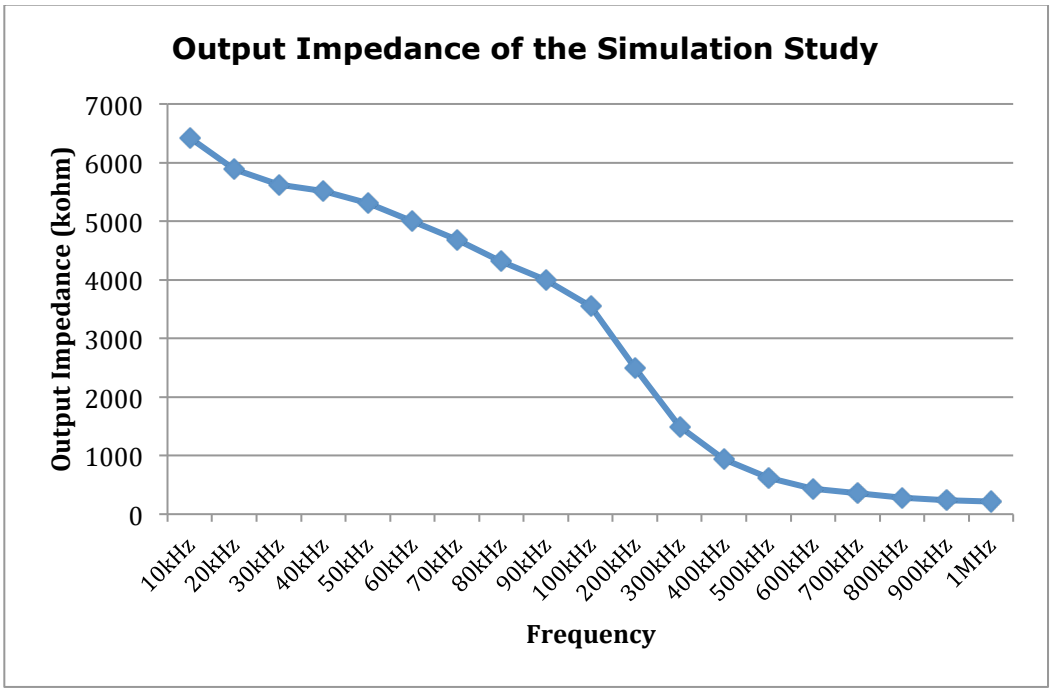

Figure 3.18 Output impedance of the simulation study

The output impedance decreases expectedly as the operating frequency increases. At the highest frequency (1 MHz), the current source has 211 kΩ. This value is greater than the 100 times of our load (1.5k-2kΩ).

3.5.2.4 Phase Delay

Phase delay is another aspect that may cause performance degradation in current designs besides the output impedance. Large phase delay effects the output current stability. There is not any accepted value or limit for the phase delay in literature. However, the studies (mentioned in previous sections) suggest phase delay lower than -25^{o} is beneficial for the implementation of the current source [74]. There are not many studies available discussing the phase delay. Phase delay is generally measured in simulation studies as an indicator for the frequency response. Figure 3.19 shows the phase delay of the current source simulation. -11.7^{o} is measured for the highest frequency (1 MHz for 2kΩ load) in our bandwidth, and for the lower frequencies phase delay is in the order of milidegrees.

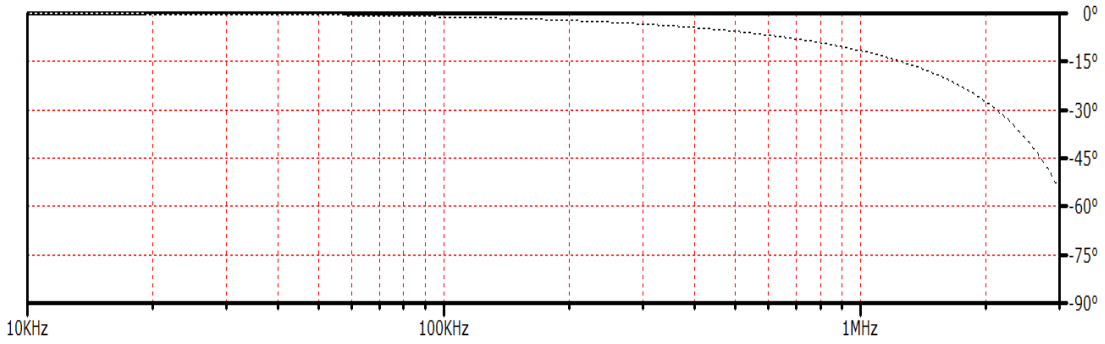

Figure 3.19 Phase delay (maximum -11.7^{o} at 1.007 MHz for 2 kΩ)

3.5.3 Implementation Results

3.5.3.1 Output impedance of the Implementation

Analytical and simulation study results give strong approval information of the operating characteristics of the current source. In previous sections, it can be concluded that the real implementation will have similar performance.

Implementation of the current source is realized on a printed circuit board, using surface-mount technology (smd) components. The chosen operational amplifier is only available in smd dimension (sizes are in the order of millimeters), therefore it is necessary to build a smd circuit. These components have two additional advantages:

- These smd components have low tolerance values (%0.1)
- Smd components have lower parasitic capacitance effects on the circuit, than normal printed circuit board components

The parasitic capacitance effects are not discussed in detail in the literature. There are only comments available, claiming that smd components may improve the frequency characteristic. Since this effect is generally neglected in the design procedures (in the literature studies), it will be useful to comment on the implementation performance (by experimental experience).

Table 3.4 Output impedance value of the current source at different frequencies for the implementation

Frequency (Hz)	Output Impedance (Ω)
10k	2.83M
20k	2.74M
30k	2.66M
40k	2.49M
50k	2.30M
60k	2.18M
70k	2.12M
80k	1.79M
90k	1.69M
100k	1.49M
200k	1.20M
300k	747k
400k	622k
500k	497k
600k	444k
700k	366k
800k	311k
900k	220k
1M	196k

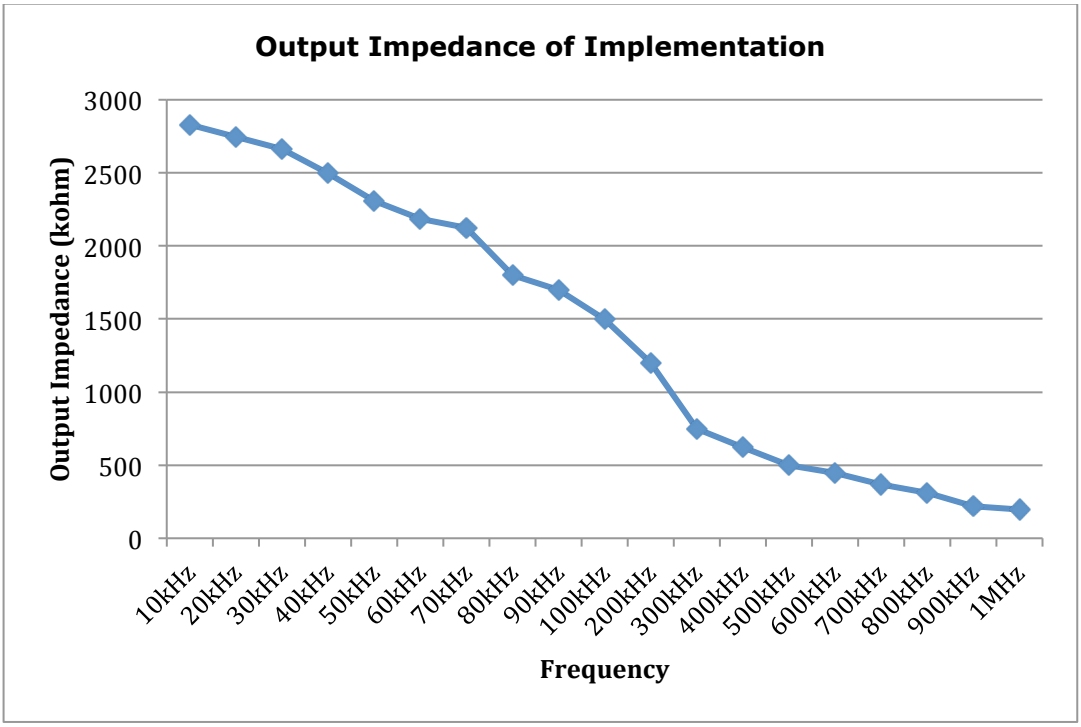

Figure 3.20 Output impedance of the implementation

3.5.3.2 Error of the Load Current

Medical safety suggests that it is possible to inject human body 10 mA_{p-p} frequencies above 100 kHz. It is our desire to apply 5 mA_{peak} and try to investigate the thermal images, thus having a load current error below 3% is beneficial for the current stability.

Table 3.5 Error of the Load Current for implementation. (For the loads of 1.5kΩ & 2kΩ, first error term is the error of I_{min} and I_{max}. The second value represents the error between I_{min} and the supposed current I_{fixed})

Load (Ω)	I_{fixed} (mA)	I_{min}(mA)	I_{max} (mA)	Error
100	5	5	5	~0
500	5	4.98	5	0.4%
1k	5	4.97	5	0.6%
1.5k	5	4.92	4.99	1.4 (1.6)%
2k	5	4.87	4.98	2.2 (2.6)%

The output current is set to 5 mA_{peak} and the injected current is measured. Table 3.5 shows the error in the current magnitude for different loads. A maximum of 2.6% error shows, the current source is stable up to 1 MHz operating region. In the table, there are two error values. The first value represents the error of the minimum and maximum currents for the corresponding load. On the other hand, the second value represents the error of the minimum and the fixed current levels. For the loads of 1.5kΩ and 2kΩ, at 1 MHz the maximum current applied are 4.99 mA and 4.98 mA respectively.

The aim is to design a current source that can drive loads up to 1.5-2kΩ. At the beginning of this chapter, it is mentioned that having an output impedance of 100 times of load is necessary to maintain this requirement. Both simulation and implementation studies show that this current source has at least 200kΩ output impedance at 1 MHz. Implementation of the current source proves the simulation study assumptions and predictions. Now, it is possible to confirm that the current source is able to inject 5 mA current for the loads up to 2kΩ between 10 kHz and 1 MHz. This designed and implemented current source is used in the multi frequency electro-thermal imaging experiments, which will be covered in the next chapter.

3.6 Conclusion

Chapter 3 discussed the facts of ¨Howland Current Pump¨. Fundamental knowledge on working principles and the key features that should be focused on the design process, are underlined. By carefully matching the resistance values, output current is derived independent of the load but only depends on the input voltage and ratios of some resistors.

In addition to providing theoretical information, performance of the design is presented by giving the output resistance characteristics over the frequency range. Although implemented source shows lower output resistance than expected, it still acts as an ideal current source for low resistance values (1.5kΩ).

Howland is a well-known current source topology. There are various designs based on Howland topology, however design procedures are not clearly discussed in detail. Only the operational amplifier model and resistor values are given in most of the studies.

Finally, it will be useful to comment the possible reasons of the decrease in the output impedance. With the increasing frequency, the input capacitance of the operational amplifier becomes dominant. The effect of this capacitance on the pole location is previously discussed. This capacitance causes degradation in the output impedance. Additionally, the real implementation results contain the non-ideal characteristics of the components of the circuit (resistor, etc.). In the simulation study, the resistors are assumed ideal as the temperature changes, and in means of tolerance values. However, in real implementation even 0.1% tolerance value results as reduction in output impedance, consequently in output current.

CHAPTER 4

EXPERIMENTAL STUDY

Electro – thermal imaging experiments are conducted using an infrared camera and a phantom mimicking human body tissues. Chapter 4 describes the experimental setup, the phantom preparation procedure, and results of the first experimental studies conducted for multi-frequency electro-thermal imaging.

4.1 Experimental Setup

In the *in vitro* study, a phantom is used to mimic the electrical properties of the woman breast tissue. In the ¨active¨ mode, external AC source injects current to the tissue model and thermal distribution on the phantom surface is detected bya thermal infrared camera. Fig 4.1 demonstrates the experimental setup.

Maintaining constant ambient (environmental) temperature is crucial for the consistency of the experiment. Pennes' bio heat equation assumes that the surrounding temperature does not change over time. For this reason, the room temperature should be kept constant. Air conditioner is suitable for fixing the ambient temperature.

Figure 4.1 shows the experimental setup:

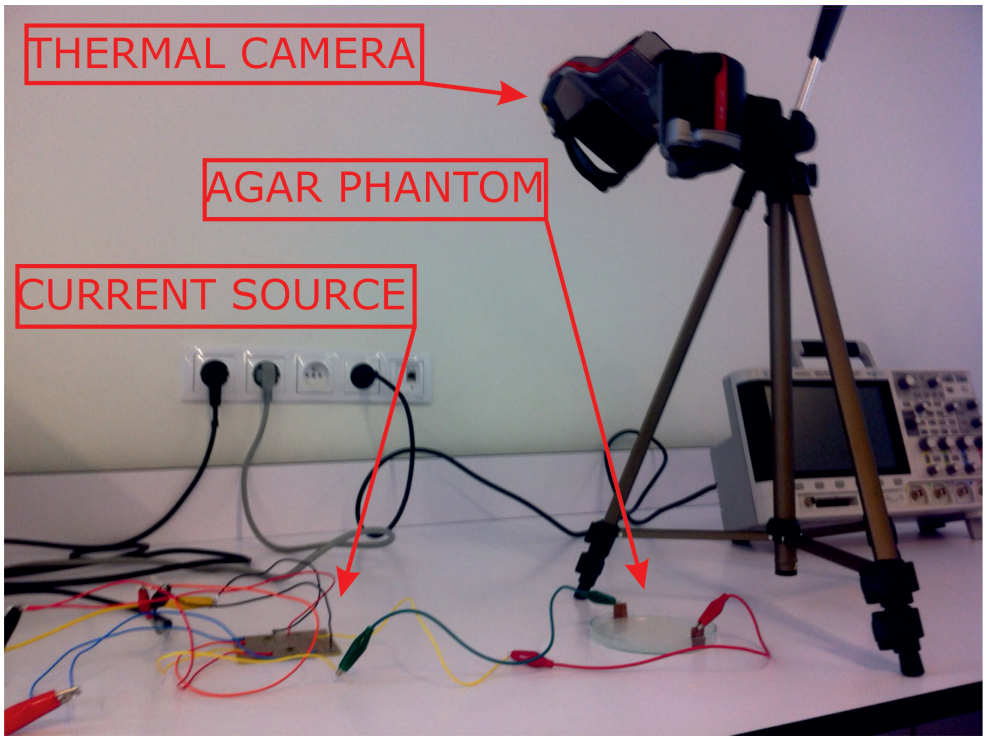

Figure 4.1 Experimental Setup

4.2 Phantom Preparation

There are many phantom models used to simulate biological tissues. High water content saline solution is commonly used in various studies to mimic the breast tissue [58]. The solution contains

- Water (deionized)
- NaCl
- Solidifying agent

Deionized water represents the high water content of the tissue. Sodium chloride (NaCl) amount controls the conductivity value of the phantom. Higher NaCl in the solution will result in a higher conductivity. Thus, the agar solution prepared for the representation of the cancerous tissue has a higher NaCl concentration than the healthy tissue. Agar is a solidifying agent that balances melting and gel stability at

temperatures close to the nominal human body temperature (37^{o}C). It is also preferred to inhibit water decomposition in the solution. TX-150 and TX-151 are advanced solidifying agents used in the literature, in which TX-151 solidifies the solution quicker than TX-150 and also has higher functional life time. But still, the phantoms prepared with TX content, degrades much faster than the phantoms prepared using agar. In this study, the phantom should be in complete thermal equilibrium, which requires sufficient waiting time. For this purpose, TX agents are not used.

The solidifying agent plays a key role in the process of reaching thermal equilibrium. The phantom model is prone to decompose, lose the shape and rigidity. These deformations may cause the phantom losing its contact to the electrodes. In this case it is impossible to deliver the current to the phantom. Another important effect of solidifying agent is maintaining the homogeneity of the phantom. During current injection, external heat source may cause local melting in the phantom. For these purposes, experiments should be conducted on a narrow time interval. Prepared agar phantom should reach to thermal equilibrium (~3 hours), however; after 5-6 hours agar effect degrades and phantom begins to deform.

4.3 Experimental Results

4.3.1 Experiments on Phantom 1 (Representing Breast Tissue)

First part of the experimental studies is about generating an agar phantom mimicking the breast tissue of human body. Phantom has a circular inhomogeneity, representing the cancerous tissue, where background of the phantom represents the healthy breast tissue.

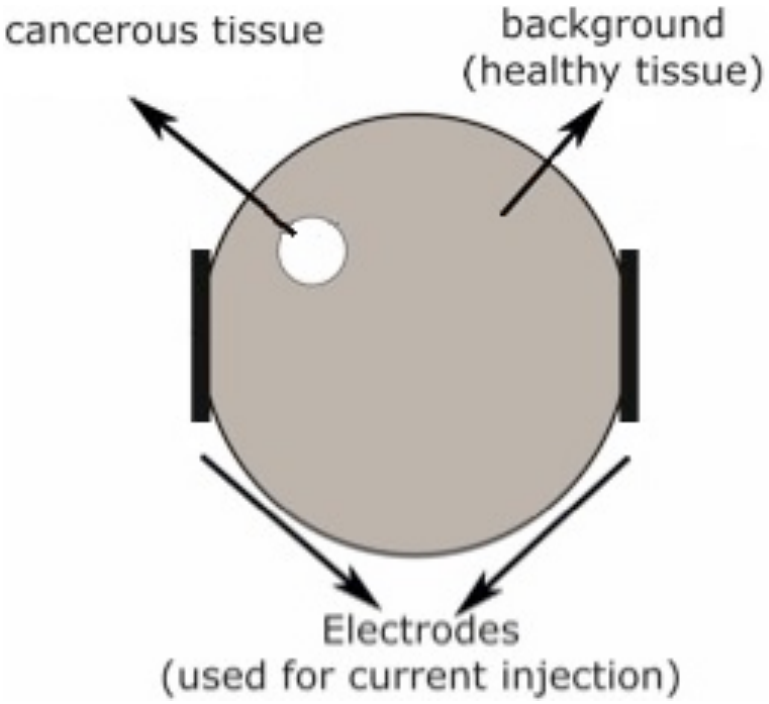

Figure 4.2 Phantom model used to mimic healthy and cancerous tissue

Fig 4.2 shows the complete phantom model. The background gray region represents the healthy (normal) breast tissue, and circular white region is the cancerous (tumor) tissue. In the preparation process, the ingredients (available in Table 4.1) are mixed at high temperatures to obtain highly homogeneous solution. Prepared agar solutions (for each region) then poured into a cylindrical container and left out to reach thermal equilibrium at room temperature. Infrared camera output is mainly changed by the emissivity and absolute temperature value of an object. Thus, it is crucially important that the whole phantom model should be at full thermal equilibrium initially.

Table 4.1 Contents of the phantom and conductivity values

Content	Healthy Tissue	Cancerous Tissue 1	Cancerous Tissue 2	Cancerous Tissue 3
Deionized water (ml)	100	100	100	100
NaCl (gr)	0.1	0.2	0.29	0.35
Agar (gr)	1.5	1.5	1.5	1.5
Sucrose (gr)	-	1.5	1.5	1.5
Conductivity (S/m)	0.2	1	1.6	2.1

Table 4.1 shows the contents of the agar phantoms prepared for the experimental procedure of electro-thermal imaging. The purpose of this thesis is to investigate the multi-frequency performance of this imaging modality. For this purpose, studies discussing the conductivity values of the breast tissues are investigated. However, most of these studies compare the electrical properties of breast tissues between kHz to GHz region. There is only one available study, suggesting the electrical conductivity values for our desired operating frequency [11]. This study concludes that between 100 kHz to 1 MHz, the healthy breast tissue electrical conductivity remains constant. On the other hand, cancerous tissue conductivity may double. In the light of this knowledge, healthy tissue conductivity is used as 0.2 S/m, and cancerous tissue conductivity is used as 1 S/m for 100 kHz. For the experiments at higher frequencies, higher NaCl content agar phantom is prepared having higher electrical conductivities (1.6 and 2.1 S/m). The phantoms of cancerous tissue 1, 2 and 3 are used for 100 kHz, 500 kHz and 1 MHz consecutively.

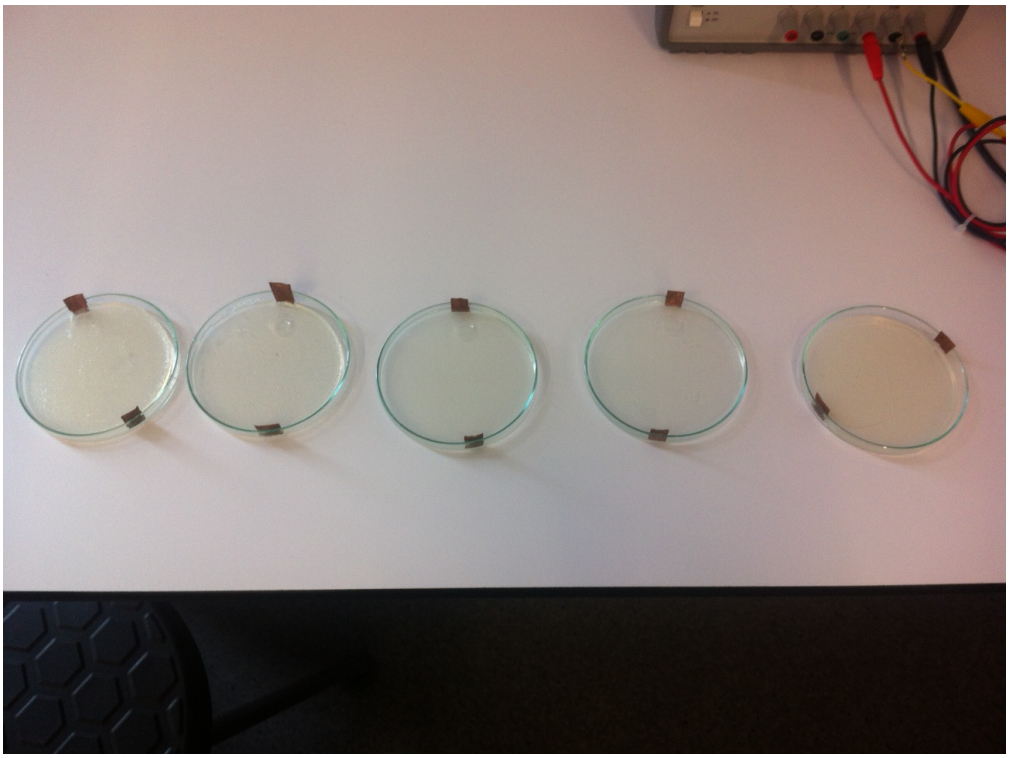

Figure 4.3 Agar phantom models used in the experiments

The experimental setup is shown in Figure 4.1. The technical specifications of the thermal camera used in the experiments are given in Table 4.2. The thermal camera is focused on the agar phantom in order to get clear images. Room temperature is kept constant by an air-conditioning system.

Table 4.2 Thermal camera specifications used in the experiments

	Camera
Detector	**Uncooled micro bolometer**
Resolution	**320x240**
Dynamic range (bit)	**14**
Spectral range (μm)	**7.5-13**
NETD (at 30°C)	**50 mK**
Frame rate (Hz)	**9**
Minimum focus distance (cm)	**40**

Experimental procedure starts with the agar phantom preparation. After adding inhomogeneity (cancerous tissue) inside the phantom, approximately 3 hours is required to reach the thermal equilibrium. When the thermal equilibrium is maintained, thermal image of the phantom is taken (t=0).

At t=0, current source operating at a specific frequency is turned on and 5 mA_{peak} current is injected to the phantom by using 1 cm^2 electrodes for 10 minutes.

At t=5 min, another image is recorded. This is an intermediate image providing additional information and comparison between t=0 and t=10 min images.

At t=10 min, final thermal image is taken. Ratio images are constructed using this image (taken at t=10 min) and the initial image (at t=0), to detect the thermal differences on the phantom. This experiment is repeated for three different frequencies, namely, 100kHz, 500 kHz and 1MHz.

Figures 4.4 (a), 4.5 (a)and 4.6 (a) show the passive mode images before each active mode experiment. Figures 4.4 (b), 4.5 (b) and 4.6 (b) are the active mode images after 5 minutes of current injection when the injection frequency is 100 kHz, 500 kHz, and 1 MHz, respectively. Figures 4.4 (c), 4.5 (c) and 4.6 (c) are the active mode images after 10 minutes of current injection, for these three current injection configurations. It is concluded that, it is not possible to distinguish any difference when the absolute thermal images are observed. However, as it was proposed in Carlak'sPh.D thesis [6], the inhomogeneity, which is not observable in the passive mode images, can be distinguished by normalizing the active mode images with the passive mode ones. For each current drive frequency, the active mode images recorded at t=10 min are normalized with the corresponding passive mode images. These normalized images are shown in Figure 4.7.

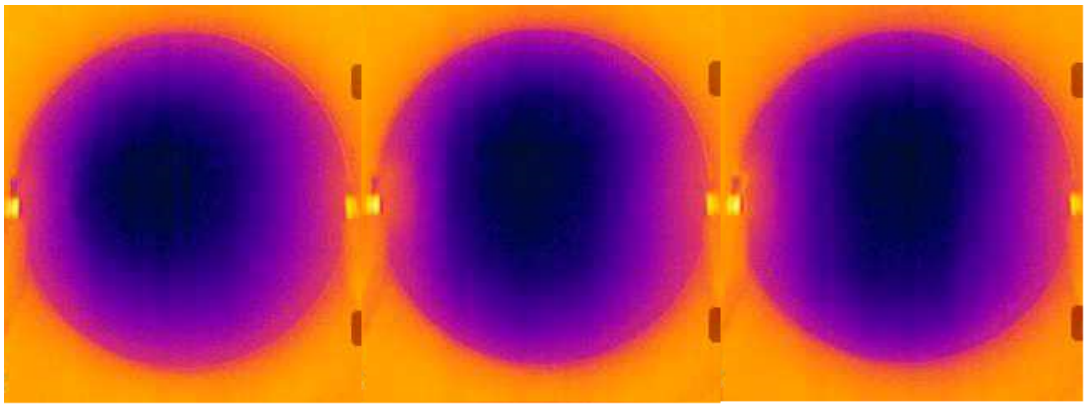

(a) (b) (c)

Figure 4.4 Thermal images of the phantom. (a) Passive mode image (no current injection) (b) after 5 minutes of current injection at 100 kHz (c) after10 minutes of current injection at 100 kHz

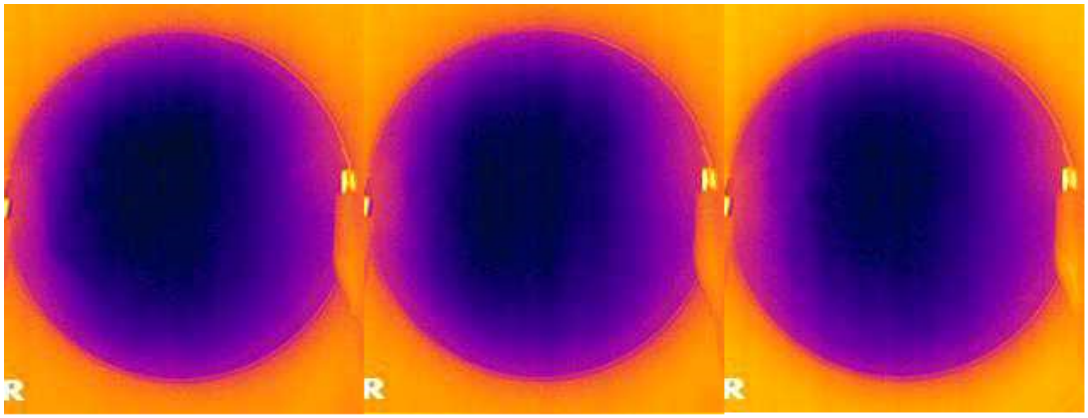

(a) (b) (c)

Figure 4.5 Thermal images of the phantom. (a) Passive mode image(no current injection) (b) after 5 minutes of current injection at 500 kHz, (c) after 10 minutes of current injection at 500 kHz.

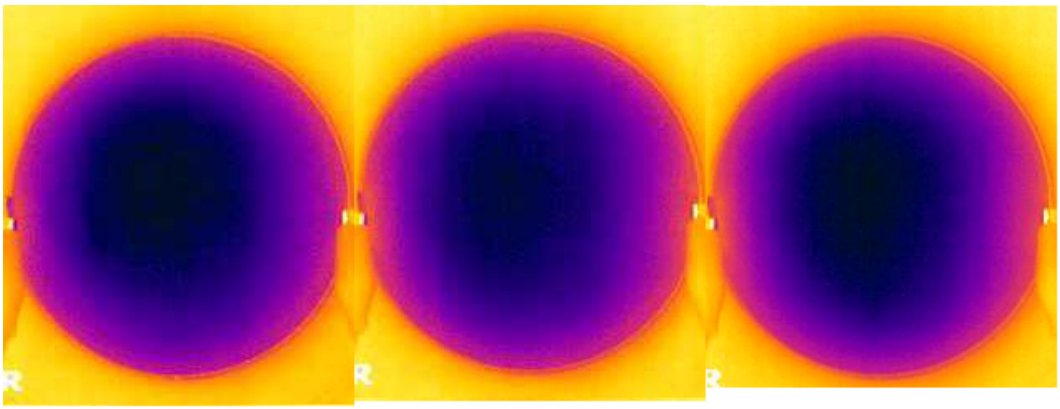

(a) (b) (c)

Figure 4.6 Thermal images of the phantom. (a) Passive mode image(no current injection) (b) after 5 minutes of current injection at 1 MHz, (c) after 10 minutes of current injection at 1 MHz.

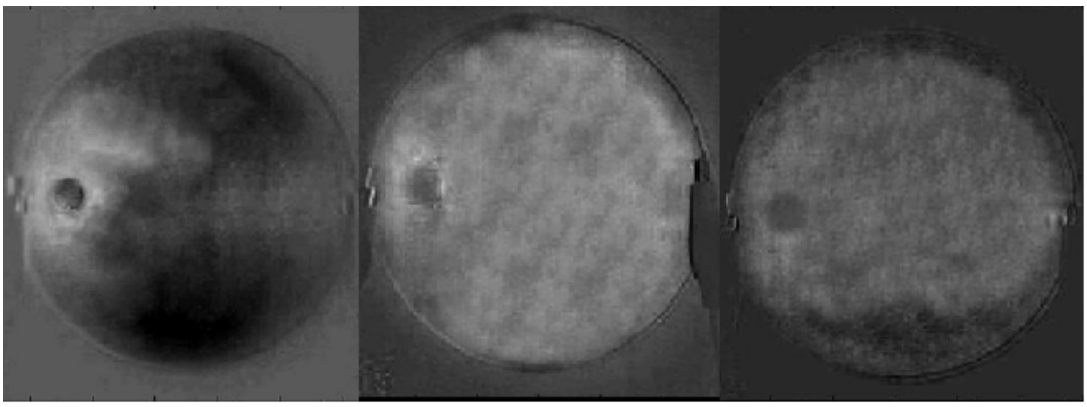

(a) (b) (c)

Figure 4.7 Normalized images of the phantom: division of the passive mode image to the active mode image obtained after 10 minutes of current drive. Current drive frequency (a) 100 kHz (b) 500 kHz (c) 1 MHz.

Figure 4.7 shows that the abnormality in the phantom (cancerous tissue) can be distinguished in the normalized images. Experimental results suggest that it is possible to obtain information about the size and location of the abnormality, the temperature difference between the healthy and cancerous tissue by displaying the normalized images. However, when the abnormalities cannot be detected visually, more detailed analyses is required to obtain a quantitative information.

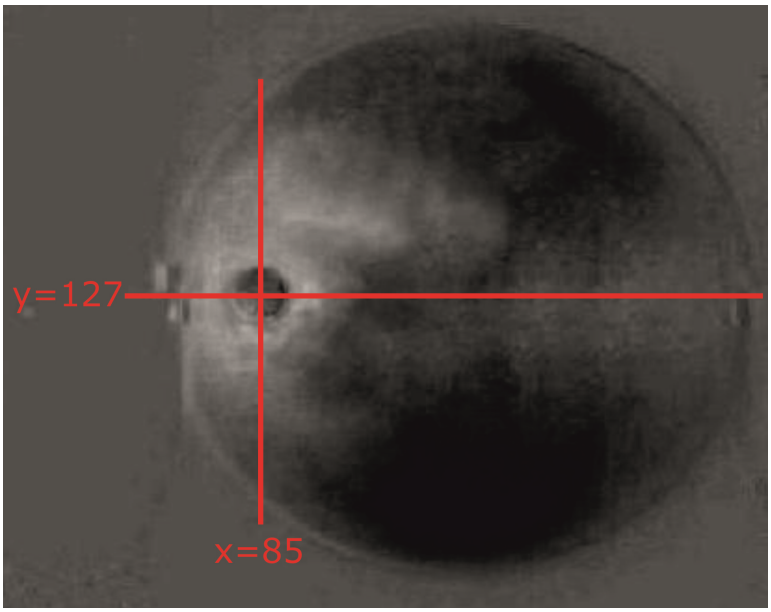

Figure 4.8 Vertical (x=85) and horizontal (y=127) axis of the center of the abnormalityfor 100 kHz

Figures 4.8, 4.10 & 4.12 show the vertical and horizontal axis which thermal distributions over these axisare plotted in figures 4.9, 4.11 & 4.12.

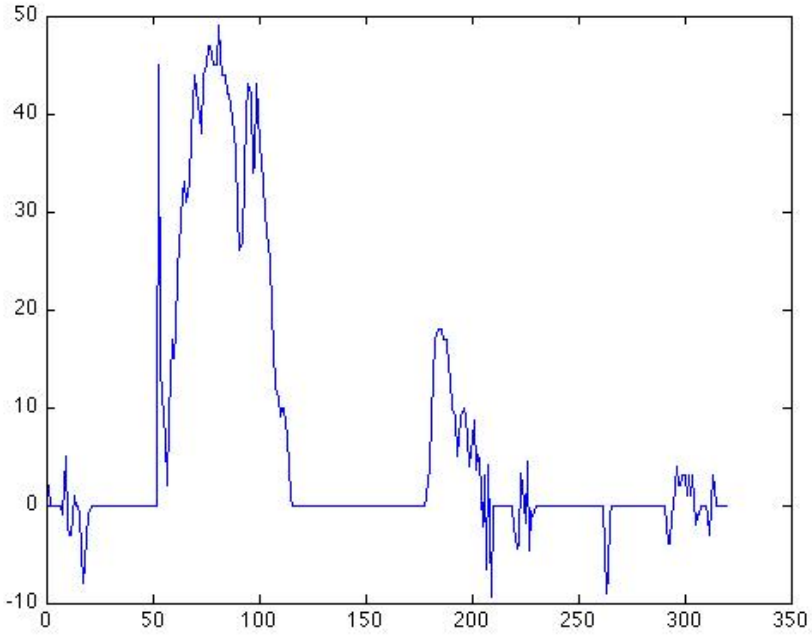

(a)

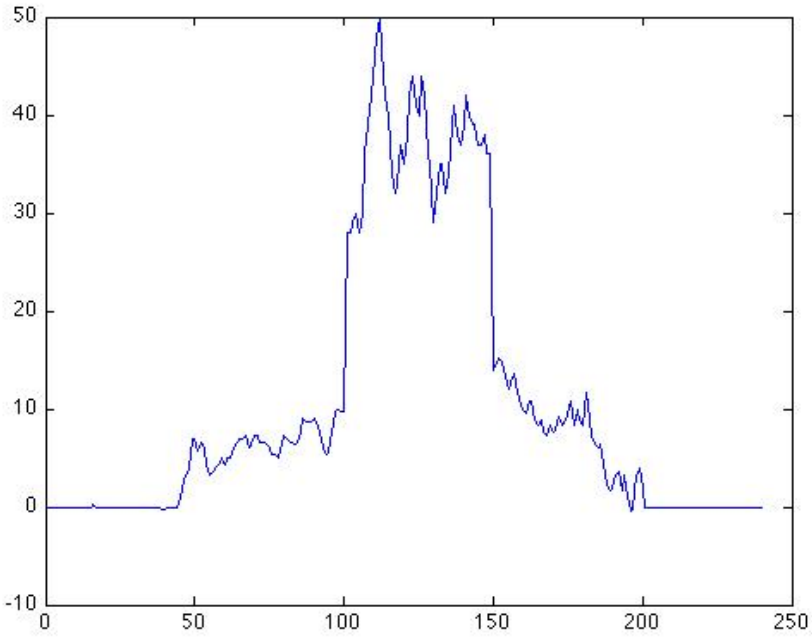

(b)

Figure 4.9 Thermal distributions over a specified x and y-axis of the phantom for 100 kHz. (vertical axis is arbitrary unit, horizontal axis shows the pixel location) (a) thermal distribution at y=127 (b) thermal distribution at x=85

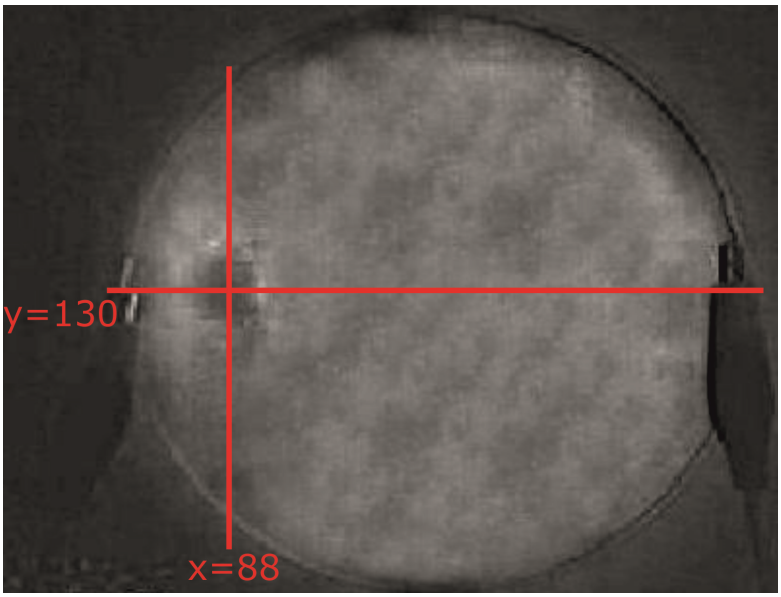

Figure 4.10 Vertical (x=88) and horizontal (y=130) axis of the center of the abnormality for 500 kHz

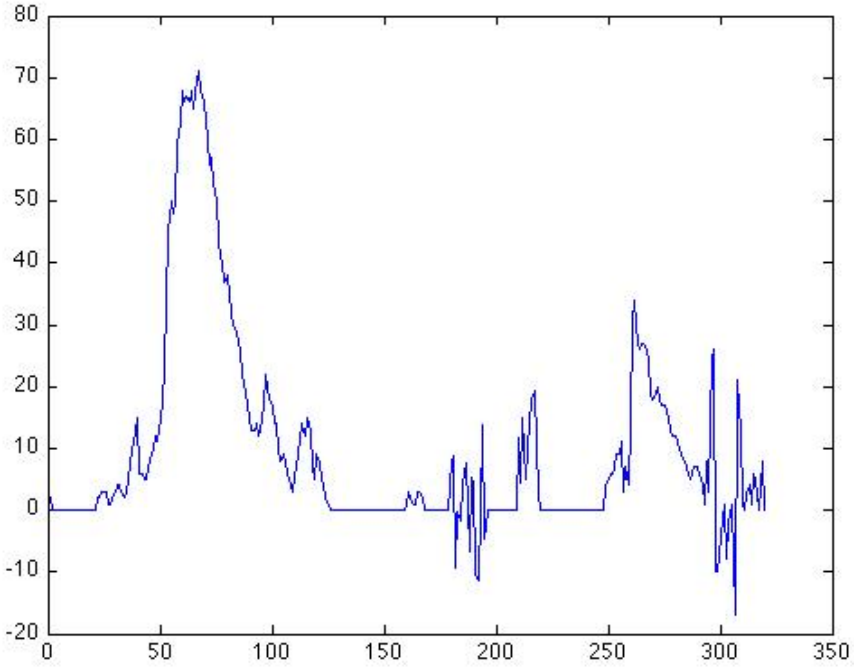

(a)

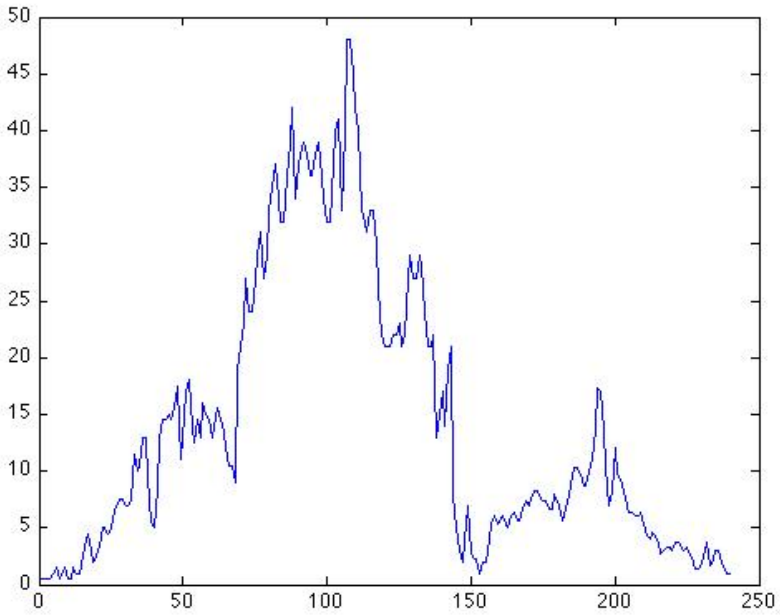

(b)

Figure 4.11 Thermal distributions over a specified x and y-axis of the phantom for 500 kHz. (vertical axis is arbitrary unit, horizontal axis shows the pixel location) (a) thermal distribution at y=130 (b) thermal distribution at x=88

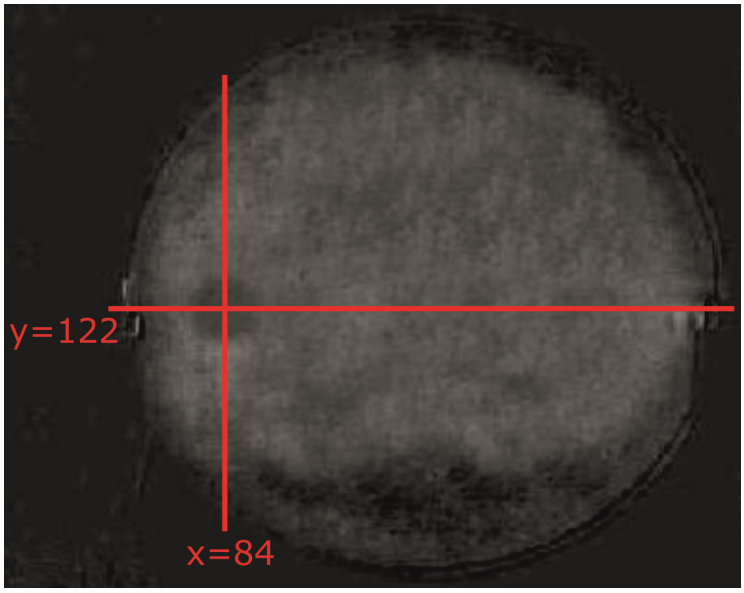

Figure 4.12 Vertical (x=84) and horizontal (y=122) axis of the center of the abnormality for 1 MHz

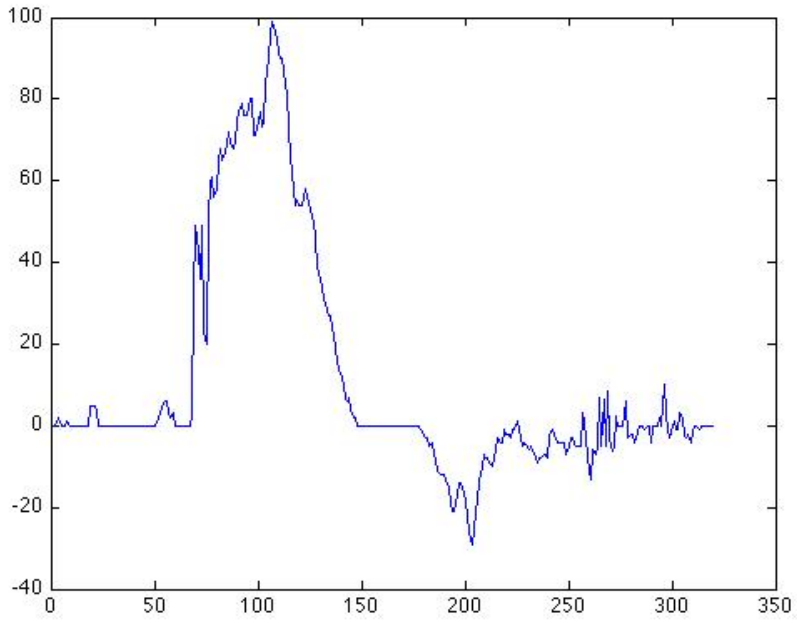

(a)

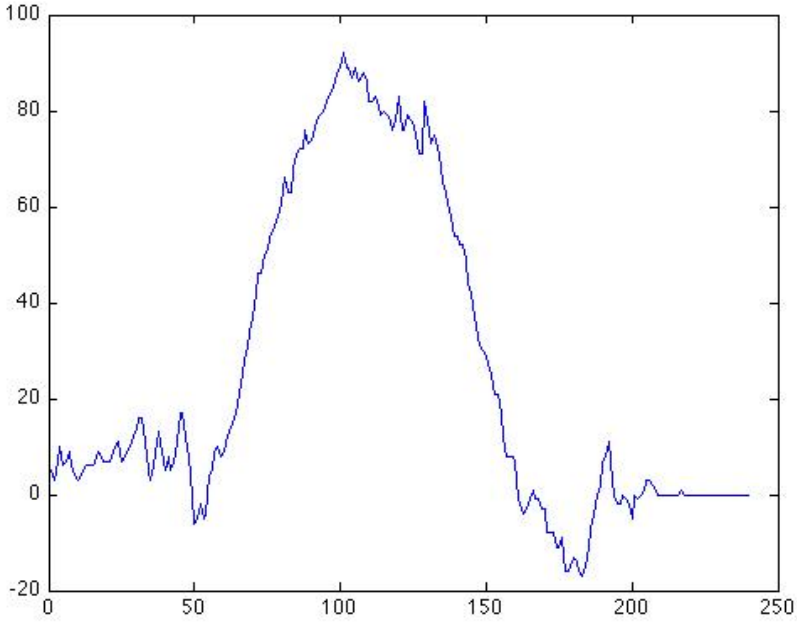

(b)

Figure 4.13 Thermal distributions over a specified x and y-axis of the phantom for 1 MHz. (vertical axis is arbitrary unit, horizontal axis shows the pixel location) (a) thermal distribution at y=122 (b) thermal distribution at x=84

Figures 4.9, 4.11 and 4.13 show one-dimensional temperature distributions after 10 minutes of current injection for sinusoidal current drive at frequencies of 100 kHz, 500 kHz and 1 MHz. The imaged axes are chosen as the probable tumor location visible in the normalized images. Considering the tumor location, the average temperature levels of the abnormality and the background (phantom) can be calculated.

In Carlak'sPh.D thesis [6], this additional temperature change was detected when current drive was applied at lower frequencies (at 10 kHz). Tumor location and generated temperature difference were determined. However, in those experiments, it was not possible to comment on the multi-frequency performance of electro-thermal imaging. Thermal distributions recorded for current drives at different frequencies, did not provide sufficient information about the multi-frequency characteristic of electro-thermal imaging. Next experiment reveals this behavior employing a phantom considering the frequency dependent characteristics of the conductivity distribution.

4.3.2 Experiments on Phantom 2

In the first experiment, the electrical conductivity of the body phantom representing the breast tissue is independent of frequency. In order to realize a multi-frequency experimental study, a different phantoms is designed using biological bodies in saline solution. The frequency dependent conductivity characteristics of these biological bodies are well-known in the literature. The results obtained, give us supportive information about the multi-frequency use of this imaging modality for future applications.

For the second experiment, phantoms are generated by placing three biological bodies (banana, potato and carrot) inside a uniform agar solution. Studies show the electrical conductivity values of these biological materials up to 500 kHz [85]. In

this study, multi-frequency experiments will be conducted between 10 kHz – 1 MHz. Figure 4.14 shows the phantom model used in the experiments. Potato, carrot and banana are used in regions 1, 2 and 3, respectively.

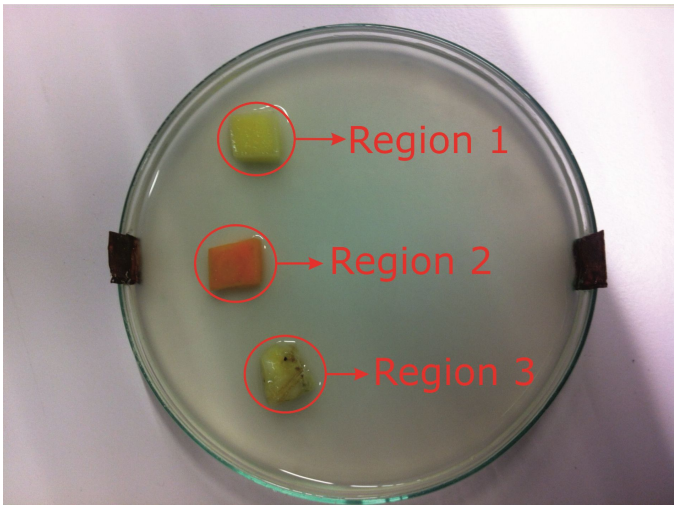

Figure 4.14 Phantom model. Region 1, 2 and 3 shows pieces of potato, carrot and banana, respectively.

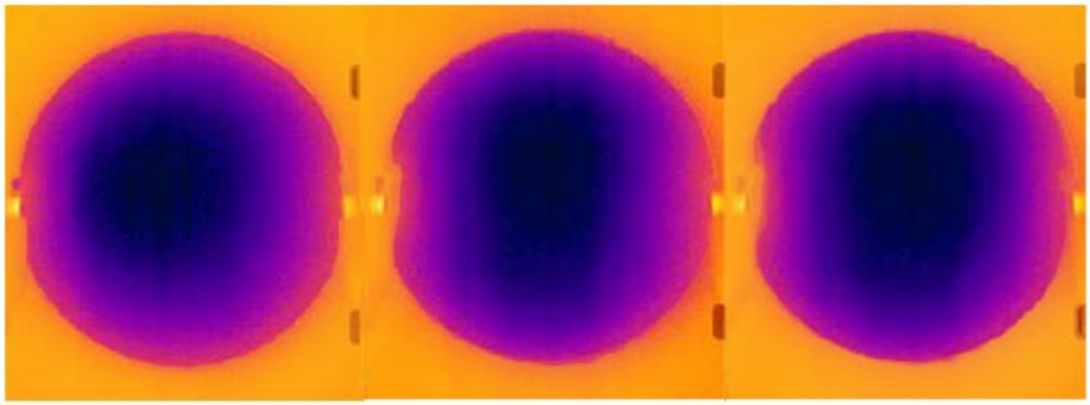

(a) (b) (c)

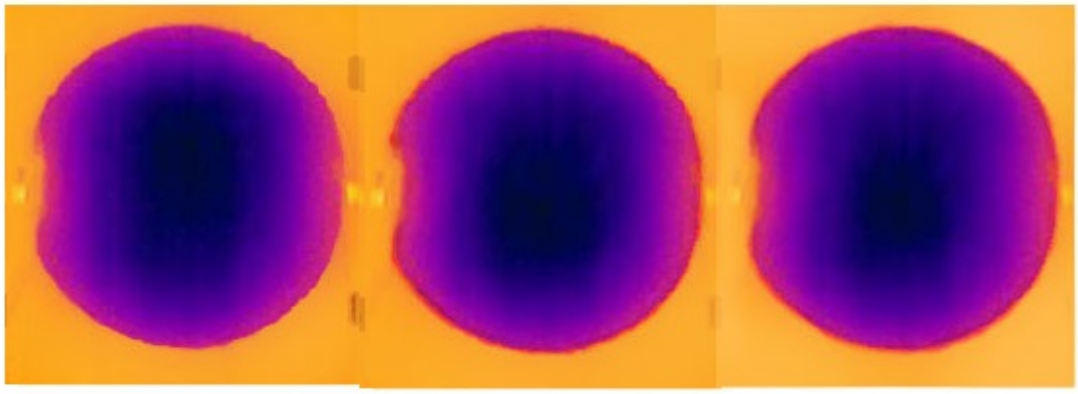

(d) (e) (f)

Figure 4.15 Thermal images of the phantom. (a) Passive mode image(no current injection).After 10 minutes of current injection at (b) 10 kHz, (c) 100 kHz, (d) 250 kHz, (e) 500 kHz, and (f) 1 MHz.

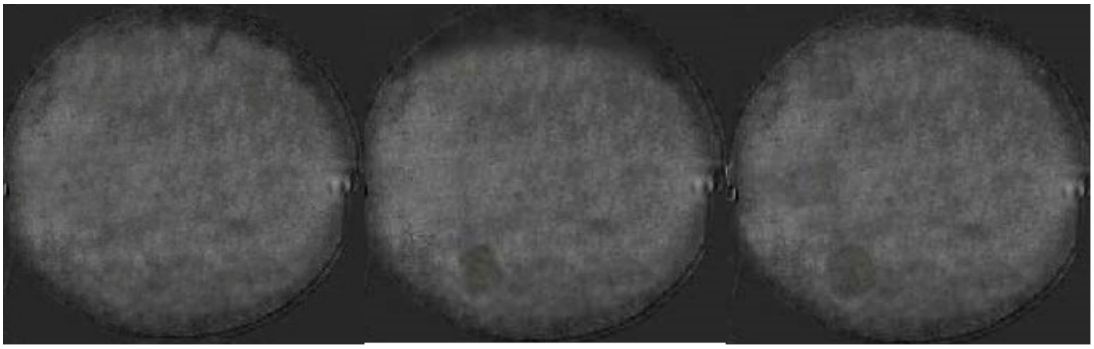

(a) (b) (c)

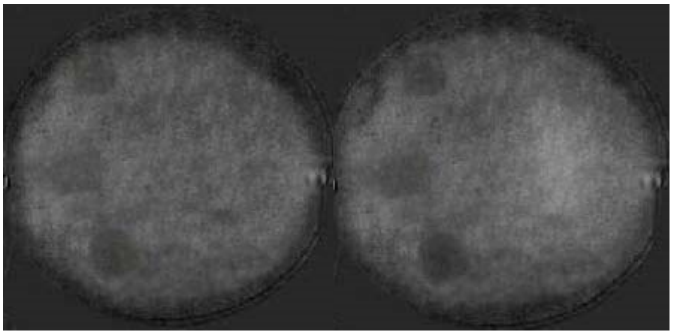

(d) (e)

Figure 4.16 Normalized images of the phantom after 10 minutes of current injection at (a) 10 kHz, (b) 100 kHz, (c) 250 kHz, (d) 500 kHz, (e) 1 MHz.

Figure 4.16 shows the change in distinguishability for different regions when different frequencies are used for current injection. At 10 kHz, the normalized image is uniform, the three inhomogeneities cannot be distinguished (Fig. 4.16 (a)). As the frequency increases, the electrical conductivities of banana, carrot and potato also increase. Thus, temperature difference between the abnormal regions and background is elevated.

At 100 kHz, it is possible to distinguish region 3, representing banana (Fig. 4.16 (b)).This is expected as seen in Fig. 4.17 from the frequency dependent characteristic of banana. Comparing to other regions, region 3 has the greatest contrast at that frequency, while other regions are not visible.

Starting from 250 kHz, region 1 (potato) is detectable (Fig. 4.16 (c)). As the frequency increases, the contrast for this region improves.

For region 2 (carrot), the distinguishability of the region does not change much, with the increasing frequency. Frequencies up to 500 kHz, this region is barely visible(Fig. 4.16 (d)). Carrot can be seen, when the current injection frequency is 1 MHz (Fig. 4.16 (e)).For such a high frequency current drive, all regions are detectable. The results coincide with literature in most parts.

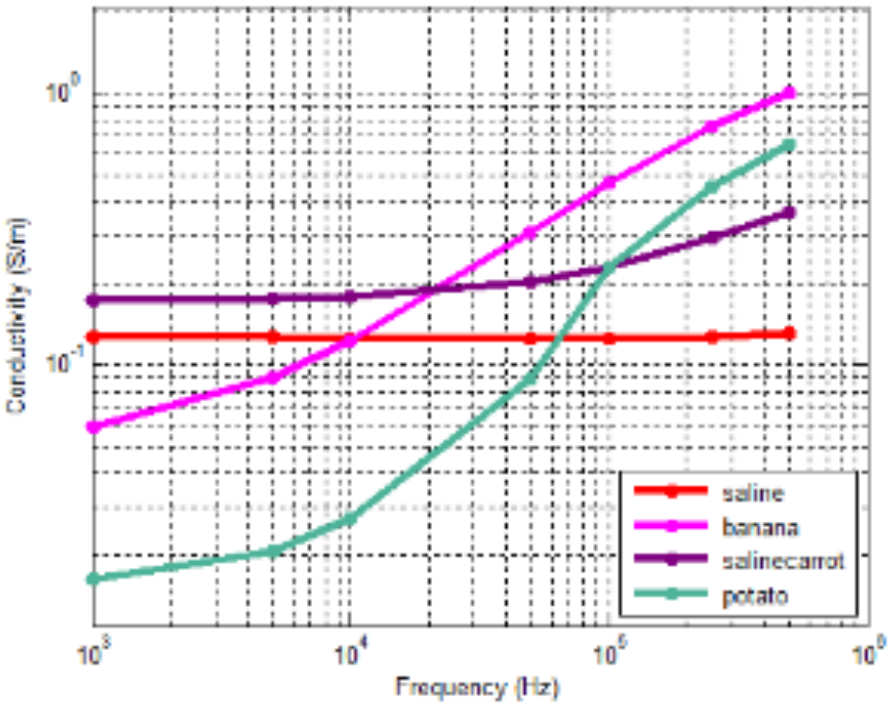

Figure 4.17 Electrical conductivity of the contents of phantom 2 [85]

4.4 Conclusion

In this chapter, the instruments used in the experimental procedure are expressed. The critical aspects and process of phantom preparation are discussed in detail. The contents of different saline solutions and the corresponding electrical conductivity values are presented.

In the first part of the experimental study, the conductivity values are chosen as the previous studies on dielectric properties of tissues suggest. Active and passive images and normalized images taken for 100 kHz, 500 kHz and 1 MHz current drive are presented, concluding that the external heat source creates a temperature difference between healthy and cancerous tissue. In addition to the images, graphics displaying thermal distribution over specific axis are shown.

In the second experimental study, another phantom is generated. The electrical properties of the contents of this phantom (banana, potato and carrot) change with the frequency of the current stimulus. A single phantom can be used for multi-frequency experiments. Resulting images show that at lower frequencies (10 kHz) none of the abnormal regions can be distinguished. As the application frequency increases up to 1 MHz, all of these regions become detectable.

In this thesis multi-frequency effect of the external AC current source is investigated. In experimental results, the use of active mode operation is clearly shown.

CHAPTER 5

CONCLUSION AND DISCUSSION

In this thesis, mathematical basis of electro – thermal imaging modality was presented. A voltage controlled current source was designed to prove the multi-frequency performance of electro-thermal imaging, experimentally. The current source operates stably up to 1 MHz for loads between 100 – 2kΩ. Howland current source is used in the design. This topology is well known and commonly used in current source designs. However, previous studies in the literature do not explicitly give the design rules. Operational amplifier is assumed ideal, and the optimum resistor values are adjusted by trial and error. In this study the design rules are derived and clearly presented. The limitations caused by each term are revealed:

- Input capacitance of the opamp should be as low as possible
- Input resistance of the opamp should be as large as possible
- Open loop gain and frequency characteristic obviously should be high and wide-band
- Output resistance of the opamp should be as low as possible
- Resistors R and r should be fixed to an optimum value

In this study, a current source operating up to 1 MHz, is designed and realized. However, this work can be improved. Using an operational amplifier with better specifications mentioned above (input capacitance, resistance etc.), will improve the frequency characteristics.

Resistor choice (for R and r) also decreases the frequency response. In chapter 3, the reasons of R and r choices are clearly presented. Operational amplifier output current limit and load current strength prevent R being smaller and r larger. Using an

opamp with higher current delivery, makes R smaller, improving the frequency performance.

This design is the first current source that is able to deliver a maximum of 5 mA current to the loads up to 2 kΩ, from 10 kHz to 1 MHz bandwidth. The primary aim of this design is to heat up the tissue sample. In previous studies, current source designs are made for mostly bio impedance measurements, and 1 mA current level for small loads (~300-400Ω) was considered to be sufficient, in the same frequency region.

The purpose of conducting a multi – frequency study is to determine the healthy – malignant tissue characteristics at different frequency values. Since it has been known that tissues have different electrical properties at different frequencies, different thermal images can be obtained for the same tissue and same current drive electrodes. Each image represents different thermal distribution because of the change in tissue electrical properties. An abnormality may be distinguishable for a specific current application, however; at another injection frequency, the abnormality may totally disappear. In these experiments, none of the biological tissue models (banana, carrot, potato) can be distinguished for a current injection at 10 kHz. On the other hand, at an operation frequency of 500 kHz all of these regions are distinguished. When the current injection frequency is increased to 1 MHz the image contrast is improved by 80 %. These images can be either analyzed individually, or combination of various ¨active¨ mode images may provide useful information about the health of the tissue. Experimental work conducted in this study, makes it possible to show the potential of multi-frequency electro-thermal imaging in detecting cancerous tissues.

This study can be expanded to cover a wider frequency range. For example, obtaining active thermal images in MHz-GHz band may provide additional information about the frequency dependent characteristics of various cancerous tissues.

REFERENCES

[1] American Cancer Society, Cancer Statistics 2012 www.cancer.org (Last accessed date: 20.01.2013)

[2] R. Lawson, ¨Implications of Surface Temperatures in the Diagnosis of Breast Cancer¨, Canad. M. A. J., pp.309-310, 1956

[3] H. Spitalier, D. Giraud, R. Amalric, ¨Does Infrared Thermography Truly Have a Role in Present-Day Cancer Management?¨, Biomedical Thermology. Alan R. Liss, Inc., NY, pp. 269-278, 1982

[4] R. Berz, C. Schulte-Uebbing, ¨Mammovision – 114 Cases Evaluated¨, 2008

[5] M. R. Sharlon, "Active Thermography: An Overview of Methods and Their Applications in Use Today"

[6] H.F. Carlak, ¨Electro-Thermal Imaging¨, Ph.D Thesis, Middle East Technical University, 2012

[7] H. F. Carlak, N. G. Gençer, C. Beşikçi, ¨Thermal Images of Electrically Stimulated Breast: a simulation study¨, Medicon 2010 12thMediterrenean Conference, 2010

[8] H. F. Carlak, N. G. Gençer, C. Beşikçi, "Medical Thermal Imaging of Electrically Stimulated Women Breast: A Simulation Study", IEEE Engineering in Medicine and Biology Society Conference 2011 (EMBS 11)

[9] R. Tipa, O. Baltag, ¨Microwave Thermography for Cancer Detection¨, Rom. Journ. Phys., vol.51, no.3-4, pp.371-377, 2006

[10] J. R. Keyserlingk, P. D. Ahlgren, E. Yu, N. Belliveau, M. Yassa, ¨Functional infrared imaging of the breast¨, IEEE Engineering in Medicine and Biology, pp.30-41, 2000

[11] A. J. Surowiec, S. S. Stuchly, J. B. Barr, A. Swarup, ¨Dielectric Properties of Breast Carcinoma and Surrounding Tissues¨, IEEE Transactions Biomedical Engineering, 35, p.257-263, 1988

[12] A. M. Hassan, M. El-Shenawee, ¨Review of Electromagnetic Techniques for Breast Cancer Detection¨, IEEE Reviews in Biomedical Engineering, vol.4, pp.103-118, 2011

[13] J. Brown, S. Bryan, R. Warren, ¨Mammography screening: an incremental cost effectiveness analysis of double versus single reading of mammograms¨, Br Med Journal, vol.312, pp.809-812, 1996

[14] P. Metherall, D. C. Barber, R. H. Smallwood, B. H. Brown, ¨Three – dimensional electrical impedance tomography¨, Nature, vol. 380, pp.509 – 512, 1996

[15] N. Avril, C. A. Rose, M. Schelling et al., ¨Breast imaging with positron emission tomography and fluorine-18 flourodeoxyglucose: use and limitations¨, Journal of Clinical Oncology, vol. 18, pp.3495-3502, 2000

[16] Furstenberger et al., ¨Insulin like growth factors mediate breast cancer growth and proliferation¨, Onkologie, vol. 26, no. 3, pp.290-294, 2003

[17] The Electromagnetic Spectrum Figure (Last accessed date: 04.11.2012) http://premediablog.widen.com/blog/the-color-space/call-me-mr-biv-v1

[18] M. Anbar, ¨Clinical Thermal Imaging Today¨, School of Medicine and Biomedical Sciences, IEEE Engineering in Medicine and Biology, pp. 25-33, 1998

[19] J. Gershen-Cohen, J. Haberman, E. E. Brueschke, ¨Medical thermography: A summary of current status¨, Radio Clin North Am vol.3, pp.403-431, 1965

[20] C. Gros, M. Gautherie, ¨Improved System for the Objective Evaluation of Breast Thermograms¨, Biomedical Thermology, pp.897-905, 1982

[21] H. J. Isard, W. Becker, R. Shilo, ¨Breast Thermography after Four Years and 10000 Studies¨, Am. J. Roentgenol., pp.811, 1972

[22] I. Nyirjesy, Y. Ayme, ¨Clinical Evaluation, Mammography and Thermography in the Diagnosis of Breast Carcinoma¨, Thermology, 1, pp.170, 1986

[23] J. Haberman, J. Francis, T. Love, ¨Screening a rural population for breast cancer using thermography and physical examination techniques¨, Ann. N. Y. Acad. Sci., pp.335-492, 1980

[24] Y. R. Parisky, A. Sardy, ¨Efficacy of Computerized Infrared Imaging Analysis to Evaluate Mammographically Suspicious Lesions¨, Am. J. Roentgenol, 180, pp.263, 2003

[25] L. Thomassin, D. Giraud, ¨Detection of Subclinical Breast Cancers by Infrared Thermography¨, Recent Advances in Medical Thermology, Plenum Press, New York, NY. Pp.575-579, 1984

[26] C. Gros, M. Gautherie, ¨Thermography and Cancer Risk Prediction¨, Cancer 45, pp.45-51, 1980

[27] F. J. Gonzalez, ¨Thermal Simulation of Breast Tumors¨, Instituto de Investigacion en CommunicacionOptica, Universidad Autonoma de San Luis Potosi, 53, pp.323-326, 2007

[28] R. Joro, A. L. Laaperi, P. Dastidar, R. Jarvenpaa, T. Kuukasjarvi, ¨A Dynamic Infrared Imaging Based Diagnostic Process for Breast Cancer¨, ActaRadiologica, 50, p.860-869, 2009

[29] H. Fricke, S. Morse, ¨The Electric Capacity of Tumors of the Breast, Journal of Cancer Res, vol.10, pp.340-376, 1927

[30] A. G. Conrad, H. W. Haggard, B. R. Teare, ¨Electrical Studies of Living Tissues¨, IEEE, 55, p.768-772, 1936

[31] K. S. Cole, R. H. Cole, ¨Dispersion and Absorption in Dielectrics – I Alternating Current Characteristics¨, Journal of Chemical Physics, vol.9, pp.341-352, 1941

[32] E. Teschner, M. Imhoff, ¨Electrical Impedance Tomography: The Realization of regional ventilation monitoring,¨Drager

[33] H. P. Schwan, ¨Electrical Properties of Tissues and Cell Suspensions¨, Advances in Biological and Medical Physics, vol.5, pp.147-209, 1957

[34] P. Tarjan, R. McFee, ¨Electrodeless Measurements of the Active Resistivity of the Human Torso and Head by Magnetic Induction¨, IEEE Transactions on Biomedical Engineering, 15, p.266-278, 1968

[35] N. G. Gençer, M. N. Tek, ¨Forward problem solution for electrical conductivity imaging via contactless measurements¨, Phys. Med. Biol., 44, p. 927-940, 1999

[36] N. G. Gençer, M. N. Tek, ¨Electrical Conductivity Imaging via Contactless Measurements¨, IEEE Transactions on Medical Imaging, 18, p.617-627, 1999

[37] R. P. Henderson, J. G. Webster, ¨An Impedance Camera for Spatially Specific Measurements of the Thorax¨, IEEE Transactions on Biomedical Engineering, vol. bme-25, no.3, p.250-254, 1978

[38] D. C. Barber, B. H. Brown, ¨ Imaging spatial distribution of resistivity using applied tomography¨, Electron. Lett., 19, p.933-935, 1983

[39] J. C. Newell, D. G. Gisser, D. Isaacson, ¨An Electric Current Tomograph¨, IEEE Transactions on Biomedical Engineering, vol. 35, no. 10, p.828-833, 1988

[40] M. H. Choi, T. J. Kao, D. Isaacson, G. J. Saulnier, J. C. Newell, ¨An Algorithm for Applying Multiple Currents Using Voltage Sources in Electrical Impedance Tomography¨, International Journal of Control, Automation and Systems, vol.6 no.4, p.613-619, 2008

[41] T. Murai, Y. Kawaga, ¨Electrical Impedance Computed Tomography Based on a Finite Element Method¨, IEEE Transactions on Biomedical Engineering, 32, Ankara, p.177-184, 1987

[42] N. G. Gençer, Y. Z. İder, M. Kuzuoğlu, ¨Sensitivity Analysis of the Backprojection Algorithm in Electrical Impedance Tomography¨, Proceedings of IEEE EMBS 14th Annual International Conference, 1992

[43] Z. Mu, A. Wexler, ¨Electrical Impedance Computed Tomography – Algorithms and Applications¨, IEEE Conference Record 1993, p.1302-1306, 1994

[44] J. Josinet, ¨Variability of Impedivity in Normal and Pathological Breast Tissue¨, Med BiolEngComput, 34, pp.346-350, 1996

[45] N. Chauveau, L. Hamzaoui, P. Rochaix, B. Rigaud, J. J. Voigt, J. P. Morucci, ¨Ex vivo discrimination between normal and pathological tissues in human breast surgical biopsies using bioimpedance spectroscopy¨, Ann NY AcadSci, v.873, p.42-50, 1999

[46] W. T. Jones, R. L. Jirtle, M. D. Rafal, D. J. Schaefer, ¨Microwave Power Absorption Differences Between Normal and Malignant Tissue¨, Int. J. Radiation Oncology Biol. Phys., vol.6, p.681-687, 1980

[47] S. S. Chaudhary, R. K. Mishra, A. Swarup, J. M. Thomas, ¨Dielectric Properties of Normal & Malignant Human Breast Tissues at Radiowave& Microwave Frequencies¨, Indian Journal of Biochemistry & Biophysics, vol.21, p.76-79, 1984

[48] A. M. Campell, D. V. Land, ¨Dielectric properties of female human breast tissue measured in vitro at 3.2 GHz¨, Phys. Med. Biol., vol.37, no.1, p.193-210, 1992

[49] T. A. Hope, S. E. Iles, ¨Technology review: The use of electrical impedance scanning in the detection of breast cancer¨, Breast Cancer Res 2004, vol.6, p.69-74, 2003

[50] T. Morimoto, Y. Kinouchi, T. Iritani, S. Kimura, Y. Konishi, N. Mitsuyama, ¨Measurements of the Electrical Bio-impedance of Breast Tumors¨, EurSurg Res, 22, p.86-92, 1990

[51] K. S. Paulson, S. Jouravleva, C. N. Mcleod, ¨Dielectric Relaxation Time Spectroscopy¨, IEEE – BME, 47, p.1510-1517, 2000

[52] K. Ö. Özkan, N. G. Gençer, ¨Low-Frequency Magnetic Subsurface Imaging: Reconstructing Conductivity Images of Biological Tissues via Magnetic Measurements¨, IEEE Transactions on Medical Imaging, 28, p.564-570, 2009

[53] E. L. V. Costa, R. G. Lima, M. B. P. Amato, ¨Electrical impedance tomography¨, CurrOpinCrit Care, vol.15, pp.18-24, 2009

[54] I. Frerichs, P. A. Dargaville, H. van Genderingen, ¨Lung volume recruitment after surfactant administration modifies spatial distribution of ventilation¨, Am J RespirCrit Care Med, vol.174, pp.772-779, 2006

[55] S. Lindgren, H. Odenstedt, K. Erlandsson, ¨Bronchoscopic suctioning may cause lung collapse: a lung model and clinical evaluation¨, ActaAnaesthesiolScand, vol.52, pp.209-218, 2008

[56] E. L. V. Costa, C. N. Chaves, S. Gomes, ¨Real-time detection of pneumothorax using electrical impedance tomography¨, Crit Care Med, vol.36, pp.1230-1238, 2008

[57] TransScan 2000 – datasheet (Last accessed date: 18.12.2012) http://www.accessdata.fda.gov/cdrh_docs/pdf/P970033c.pdf

[58] A. W. Guy, ¨Analyses of Electromagnetic Fields Induced in Biological Tissues by Thermographic Studies on Equivalent Phantom Models¨, IEEE Transactions on Microwave Theory and Techniques, 19-2, pp. 205-214, 1971

[59] M. Kaczmarek, A. Nowakowski, ¨Analysis of Transient Thermal Processes for Improved Visualization of Breast Cancer Using IR Imaging¨, IEEE EMBS Mexico, 2003

[60] P. Bernardi, M. Cavagnaro, J. C. Lin, S. Pisa, ¨Distribution of SAR and Temperature Elevation Induced in a Phantom by a Microwave Cardiac Ablation Catheter¨, IEEE Transactions on Microwave Theory and Techniques, 52-8, pp.1978-1986, 2004

[61] M. Mital, E. P. Scott, ¨Thermal Detection of Embedded Tumors Using Infrared Imaging¨, Journal of Biomechanical Engineering, 129, p.33-39, 2007

[62] J. R. Cook, J. A. Pearce, ¨Targeted Microwave Hyperthermia Monitored with Ultrasound Thermography¨, IEEE International Ultrasonics Symposium Proceedings, pp.2262-2265, 2010

[63] B. Guo, J. Li, H. Zmuda, M. Sheplak, ¨Multifrequency Microwave-Induced Thermal Acoustic Imaging for Breast Cancer Detection¨, IEEE Transactions on Biomedical Engineering, vol.54, no.11, 2007

[64] C. Smith, ¨Thermal Imaging Using Electro-Magnetic Inductiıon¨, UK Patent Application GB 2 294 604 A, 01.05.1996.

[65] H. H. Pennes, ¨Analysis of Tissue and Arterial Blood Temperatures in the Resting Human Forearm¨, Journal of Applied Physiology, vol.1, no.2, pp.93-122, 1948

[66] E. H. Wissler, ¨Pennes' 1948 paper revisited¨, Journal of Applied Physiology, vol.85, pp.35-41, 1998

[67] W. K. Ng, E. Y. K. Ng, S. J. Chia, ¨The engineering analysis of bioheat equation and penile hemodynamic relationships in the diagnosis of erectile dysfunction: part I – theoretical study and mathematical modeling¨, International Journal of Impotence Research, vol.20, pp.295-306, 2008

[68] J. W. Draper, J. W. Boag, ¨The Calculation of Skin Temperature Distributions in Thermography¨, Physics and Medicine in Biology, vol.16, pp.201-211, 1971

[69] C. W. Rice, ¨Free and Forced Convection of Heat from Bodies of Simple Shape in Gases and Liquids¨, International Critical Tables, vol.5, pp.234-236, 1926

[70] V. J. Brown, ¨Development of Computer Modelling Techniques for Microwave Thermography¨, Ph.D. Thesis, University of Glasgow, 1989

[71] T. R. Gowrishankar, D. A. Stewart, G. T. Martin, J. C. Weaver, ¨Transport lattice models of heat transport in skin with spatially heterogeneous, temperature-dependent perfusion¨, Biomedical Engineering Online, 3:42, p.1-17, 2004

[72] Z. S. Deng, J. Liu, ¨Analysis Study on Bioheat Transfer Problems with Spatial or Transient Heating on Skin Surface or Inside Biological Bodies¨, Transactions of the ASME, 124, p.638-649, 2002

[73] American National Standards, "Safe Current Limits for Electromedical Apparatus", 1993

[74] D. G. Abad, ¨Development of a capacitive bioimpedance measurement system¨, Ph. D Thesis, Helmotz-Institute for Biomedical Engineering, RWTH Aachen, 2009.

[75] Y. Yang, J.Wang, G.N. Yu, ¨Design and preliminary evaluation of a portable device for the measurement of bioimpedance spectroscopy¨, Physiol. Meas, Vol.27, pp. 1293-1310, 2006

[76] H. Solmaz, Y. Ulgen, M. Tumer, ¨Design of a microcontroller based Cole-Cole impedance meter for testing biological tissues¨, IFMBE Proceeding, vol 25, pp.488-491, 2009

[77] J. Liao, Z. Zhou, G. Wang, C. Hu, Y. Yin, ¨The Hardware System of Body Impedance Measurement¨, Proceeding of the IEEE International Conference on Information and Automation Shenzhen, China, 2011

[78] L. Zhangyon, X. Zhui, R. Chaoshi, W. Wei, Z. Dechun, Z. Huiquan, ¨Study of Voltage Control Current Source in Electrical Impedance Tomography System¨, IEEE, 2010

[79] Y. Wang, N. Li, H. Yu, Z. Sun, H. Nie, H. Xu, ¨Study on Wide-band Voltage Controlled Current Source for Electrical Impedance Tomography¨, International Conference on Intelligent Systems Design and Engineering Application, pp.1499-1502, 2012

[80] D. Bouchaala, Q. Shi, X. Chen, O. Kanoun, ¨Comparative Study of Voltage Controlled Current Sources for Bioimpedance Measurements¨, 9th International Multi-conference on Systems, Signals and Devices, 2012

[81] H. Yunfei, ¨Development of bioimpedance based human machine interface¨, M.Sc. Thesis, Prince of Songkla University, 2009.

[82] U. Tietze, C. Schenk, "Advanced Electronic Circuits", Springer Berlin Heidelberg, 2012

[83] D. H. Sheingold, "Impedance&AdmittanceTransformationsusingOperationalAmplifiers", TheLightningEmpiricist, vol. 12 no.1, 1964

[84] Analog Devices, AD8034 Datasheet (Last accessed date: 10.06.2013) http://www.analog.com/static/importedfiles/data_sheets/AD8033_8034.p

[85] S. Ahn, T. I. Oh, S. C. Jun, J. Lee, J. K. Seo, E. J. Woo, "Weighted Frequency-Difference EIT Measurement of Hemisphere Phantom", International Conference on Electrical Bioimpedance, Journal of Physics: Conference series 224, 2010 (Last accessed date: 25.07.2013) http://www.irinfo.org/articles/1_1_2008_sharlon.html